

**APPLICATION OF A QUANTITATIVE PRECIPITATION ESTIMATION  
ALGORITHM FOR THE S-BAND RADAR AT IRENE, SOUTH AFRICA**

by

Erik Hermanus Becker

Submitted in fulfilment of the academic requirements for the degree of  
Masters of Science in Engineering  
in the  
Civil Engineering Programme  
University of KwaZulu-Natal, Howard College

November 2014

Supervisor: Prof. GGS Pegram

## COLLEGE OF AGRICULTURE, ENGINEERING AND SCIENCE

As the candidate's Supervisor **I agree** to the submission of this dissertation.

Signed:



***Geoffrey Guy Sinclair Pegram***

### DECLARATION 1 - PLAGIARISM

**I Erik Hermanus Becker** declare that

1. The research reported in this thesis, except where otherwise indicated, and is my original research.
2. This thesis has not been submitted for any degree or examination at any other university.
3. This thesis does not contain other persons' data, pictures, graphs or other information, unless specifically acknowledged as being sourced from other persons.
4. This thesis does not contain other persons' writing, unless specifically acknowledged as being sourced from other researchers. Where other written sources have been quoted, then:
  - a. Their words have been re-written but the general information attributed to them has been referenced
  - b. Where their exact words have been used, then their writing has been placed in italics and inside quotation marks, and referenced.
5. This thesis does not contain text, graphics or tables copied and pasted from the Internet, unless specifically acknowledged, and the source being detailed in the thesis and in the References sections.

Signed:



**Erik Hermanus Becker**

# COLLEGE OF AGRICULTURE, ENGINEERING AND SCIENCE

## DECLARATION 2 - PUBLICATIONS

DETAILS OF CONTRIBUTION TO PUBLICATIONS that form part and/or include research presented in this thesis (include publications in preparation, submitted, *in press* and published and give details of the contributions of each author to the experimental work and writing of each publication)

### Publication 1

Becker EH., 2011: Progress on the new QPE Algorithm for the S-Band Doppler Radar, (oral) South African Society for Atmospheric Sciences, 27<sup>th</sup> Annual Conference, 22-23 September 2011, Amanzingwe Resort, Broedestroom, North West, South Africa.

### Publication 2

Becker E., Pegram G., Sinclair S., 2013: An improved QPE algorithm for the South African Weather Service's S-Band Doppler Radar at Irene, 36th Conference on Radar Meteorology, 16-20 September 2013, Breckenridge, Colorado, USA



Signed:

**Erik Hermanus Becker**

## ACKNOWLEDGEMENTS

I am grateful for the influence of many people during the course of my study. Some specific acknowledgements have to be mentioned:

**Prof. Geoff Pegram:**

My supervisor, whose knowledge and great enthusiasm for Hydrology and Radar Meteorology has kept me on track during a difficult learning curve and for keeping me motivated to complete the study when quitting seemed to be the only option.

**Dr. Scott Sinclair**

For his patience and support in difficult technical programming and all the enthusiastic discussion that were always full of knowledge and advice.

**Dr. Estelle de Coning (SAWS)**

For her invaluable advice and criticism on the operational implementation of the algorithm

**Dr. Alan Seed (BoM Australia)**

For giving me the knowledge and a thorough understanding of quantitative precipitation estimates. Thus, he laid the foundation for the study.

**Dr. Deon Terblanche**

For his advice and encouraging me to enrol for further studies

**The South African Weather Service**

For providing me with the infrastructure and data needed to complete the study.

## ABSTRACT

Flash floods are the number one cause of death and damage with regard to natural disasters in South Africa (Poolman, 2009). Thus, the South African Weather Service (SAWS) and the National Disaster Management Centre (NDMC) embarked on a collaborative project for the implementation of the South African Flash Flood Guidance system (SAFFG) in flash flood prone regions (de Coning & Poolman, 2011). The SAFFG is dependent on accurate precipitation estimates from radars and therefore much emphasis has been placed on the performance of the Quantitative Precipitation Estimation (QPE) fields. Weather radars offer the public efficient means of measuring precipitation remotely. Although the measurements are indirect radar remains the best alternative in capturing the spatial variability associated with precipitation at high temporal and spatial resolutions.

A methodology proposed by Chumchean *et al.*, (2006) was selected to be implemented and compared against the existing radar precipitation field of the Gematronik 600S S-band Doppler radar at Irene, South Africa. The methodology proposes a process that includes a rainfall classification algorithm. This algorithm separates convective from stratiform precipitation with the intent to assign different Z-R relations to the two different types of rainfall (Chumchean, *et al.*, 2008). A technique for smoothing accumulations was also included into the algorithm, which is based on optical flow techniques (Bowler, *et al.*, 2004). Reflectivity data from the Irene radar together with *in situ* rain gauge data within a 300 km radius of the radar location were obtained for the South African summer rainfall season from October 2010 to March 2011 for evaluation of the QPE field. One and twenty-four hour accumulations were compared to the corresponding rain gauge totals and the resulting evaluation scores are compared to the existing precipitation field to determine any improvements.

The study showed that by applying specific Z-R relationships to both convective and stratiform precipitation yields better results than using a single relationship only. Smoothing the precipitation with optical flow vectors further decreases the QPE error at both one and twenty-four hour accumulations. Overall the dual Z-R relationship with the optical flow smoothing yields the smallest error and is an improvement from the previous algorithm.

## TABLE OF CONTENTS

---

<b>Title Page</b>	<b>I</b>
<b>Preface</b>	<b>II</b>
<b>Acknowledgements</b>	<b>IV</b>
<b>Abstract</b>	<b>V</b>
<b>Table of Contents</b>	<b>VI</b>
<b>List of Tables</b>	<b>X</b>
<b>List of Figures</b>	<b>XII</b>
<b>List of Abbreviations</b>	<b>XIX</b>

### **Chapter 1 BACKGROUND AND INTRODUCTION**

1.1 Introduction.....	1
1.2 The South African Flash Flood Guidance System.....	1
1.3 QPE at the South African Weather Service .....	2
1.4 Aims and Approach of this Research .....	3
1.5 Summary.....	4

### **Chapter 2 RADAR RAINFALL MEASUREMENTS**

2.1 Introduction.....	6
2.2 Weather Radar Development in South Africa .....	6
2.3 The Current Radar Network in South Africa.....	10
2.4. Quantitative Precipitation Estimation .....	12
2.4.1. Reflectivity Measurements.....	13
2.4.1.1 Beam Blocking .....	14
2.4.1.2. The Bright-Band .....	19
2.4.1.3. Ground Clutter.....	21

## TABLE OF CONTENTS

---

2.4.1.4. Anomalous Propagation .....	23
2.4.1.5. Scaling .....	24
2.4.1.6. CAPPI Conversion .....	25
2.4.2. Converting Reflectivity to Rainfall Rate.....	26
2.4.2.1. Radar-Rainfall Algorithms .....	26
2.4.2.2. Classification .....	30
2.4.2.3. Optical Flow Constraint .....	31
2.4.3. BIAS Corrections .....	33
2.5. Summary .....	34

### **Chapter 3 AN ENHANCED QPE ALGORITHM FOR THE IRENE RADAR**

3.1 Introduction.....	35
3.2 The Enhanced QPE Algorithm .....	35
3.3 The Classification Scheme.....	37
3.4 Velocity Vector Calculations Using Optical Flow Constraints .....	43
3.4.1 Determine the OFC Partial Derivatives .....	44
3.4.2. Calculating the Velocity of a Block .....	46
3.4.3 Optimising the Velocity .....	49
3.5 Precipitation Estimates with Dual Z-R Relationships .....	50
3.6 Algorithm to Smooth the Spatial Rainfall Field for Accumulations .....	52
3.7 Summary .....	56

### **Chapter 4 DATA AND EVALUATION METHODS**

4.1. Introduction.....	57
4.2. Rain Gauge Data.....	57
4.2.1. Rain Gauge Network over South Africa .....	57
4.2.2. Advantages and Limitations.....	58
4.2.3. Study Period .....	59
4.2.4. Quality Control of Gauge Data .....	61

## TABLE OF CONTENTS

---

4.3 Weather Radar Data.....	62
4.3.1. The Irene Radar.....	63
4.3.2 Advantages and Limitations.....	65
4.3.3 Scan Strategy.....	70
4.3.4 Data Pre-Processing.....	73
4.4 Quantitative Precipitation Estimation (QPE) Algorithms.....	74
4.4.1 CAPPI Levels.....	74
4.4.2 Precipitation Algorithms.....	75
4.4.3 TITAN Precipitation.....	76
4.5 Verification of QPE Performance.....	76
4.5.1 Evaluation Method.....	77
4.5.2 Evaluation Scores.....	79
4.6 Summary.....	83

### **Chapter 5    RESULTS**

5.1 Introduction.....	84
5.2 Results from Classification Scheme.....	84
5.3 Algorithm Comparison.....	90
5.3.1 TITAN as a Benchmark.....	90
5.3.2 Visual Comparison of Algorithms.....	97
5.3.3 Results of Verification Scores.....	100
5.4. Precipitation Performance with Range.....	111
5.5. Summary.....	113

### **Chapter 6    SUMMARY AND CONCLUSION**

6.1 Introduction.....	114
6.2 Classifying Precipitation.....	114
6.3 Algorithm Comparison.....	115
6.4 Summary.....	116



## TABLE OF CONTENTS

---

**References**

**115**

## LIST OF TABLES

---

Table 2-1: This table illustrates the radar network of the SAWS. Listed are the date the radar was commissioned, the frequency it operates at and its capabilities. ....	11
Table 3-1: The Table lists radius of influence around the convective centre for the appropriate background average (Chumchean et al., 2008). ....	41
Table 4-1: Rain gauge stations listing the total precipitation per month compared to the Climatological value. Not Available (NA) is inserted where there was no data available and the direction to gauge and range to gauge is respective to the Irene S-band radar. ....	60
Table 4-2: One-Way Rain Attenuation $K' \text{ dB/kmm/hr} = (\text{Wexler and Atlas, 1963})$ .....	67
Table 4-3: The volume scan strategy used during the study period. ....	73
Table 5- 1: Contingency tables for hourly measurements are illustrated using 1 mm (a), 5 mm (b) and 10 mm (c) as thresholds. Scores calculated from the resulting tables are illustrated in (d). ....	94
Table 5-2: Contingency tables for daily measurements are illustrated using 1 mm (a), 5 mm (b) and 10 mm (c) as thresholds. Scores calculated from the resulting tables are illustrated in (d). ....	95
Table 5-3: Correlation coefficient scores for hourly measurements of the CRR and OFRR algorithms at the respective CAPPI levels. The TITAN algorithm is included for reference and the CAPPI level SURFACE represents the vertical column of reflectivities being projected to the surface for calculations.....	101
Table 5-4: Correlation coefficient scores for daily measurements of the CRR and OFRR algorithms at the respective CAPPI levels. The TITAN algorithm is included for reference and the CAPPI level SURFACE represents the vertical column of reflectivities being projected to the surface for calculations.....	101

## LIST OF TABLES

---

Table 5-5: Bias scores for hourly measurements of the CRR and OFRR algorithms at the respective CAPPI levels. The TITAN algorithm is include for reference and the CAPPI level SURFACE represents the vertical column of reflectivities being projected to the surface for calculations..... 103

Table 5-6: Bias scores for daily measurements of the CRR and OFRR algorithms at the respective CAPPI levels. The TITAN algorithm is include for reference and the CAPPI level SURFACE represents the vertical column of reflectivities being projected to the surface for calculations..... 103

Table 5-7: RMSE scores for hourly measurements of the CRR and OFRR algorithms at the respective CAPPI levels. The TITAN algorithm is include for reference and the CAPPI level SURFACE represents the vertical column of reflectivities being projected to the surface for calculations..... 105

Table 5-8: RMSE scores for daily measurements of the CRR and OFRR algorithms at the respective CAPPI levels. The TITAN algorithm is include for reference and the CAPPI level SURFACE represents the vertical column of reflectivities being projected to the surface for calculations..... 105

Table 5-9: Contingency table scores using thresholds of 1, 5 and 10 mm are listed in the table below. The scores are listed with the corresponding algorithm, threshold and CAPPI level. The scores are based on hourly accumulated values. The best scores in each category are highlighted in red. .... 107

Table 5-10: Contingency table scores using thresholds of 1, 5 and 10 mm are listed in the table below. The scores are listed with the corresponding algorithm, threshold and CAPPI level. The scores are based on daily accumulated values. The best scores in each category are highlighted in red. .... 108

## LIST OF FIGURES

---

Figure 1-1: Normal winter (left) and summer (right) rainfall for South Africa (Kruger, 2007). .. 2	2
Figure 2-1: The current SAWS operational radar network. The white range rings represents S-band frequency radars while the green rings the C-band frequency radars. The smaller rings are at 200km range while the larger rings are at 300km. The red dot radars do not have Doppler capabilities while the blue dot radar does have Doppler. The turquoise colour radar at Bethlehem includes both Doppler as well as Dual-Polarization capabilities. (X-band radar not include due to it not being operational. The radar will however be located at both CT int. Airport and OR Tambo Int. Airport.)..... 12	12
Figure 2-2: The Australian Bureau of Meteorology process for estimating 1 hour rainfall accumulations (Chumchean et al., 2006). ..... 13	13
Figure 2-3: A graphic illustration of 1) partial and 2) total beam blocking. It is assumed that atmospheric refraction and the curvature of the earth has no effect on the radar beam. .... 14	14
Figure 2-4: Instantaneous reflectivities at the East-London radar showing an example of beam blocking to the east of the radar. .... 15	15
Figure 2-5: A 24 hour accumulation of the C-band radar after the installation of the new S-band radar at Irene. The S-band radar causes total beam blocking to the south of the radar resulting in severe under-estimation of precipitation, the large spike of apparently increased precipitation is caused by RLAN interference. .... 16	16
Figure 2-6: Images of the large warehouse structure as seen from the top of the S-band radar tower. The buildings are the cause of partial beam blocking as well as reflection of the electromagnetic wave. .... 16	16
Figure 2-7: A 24 hour accumulation of precipitation for the Irene S-band Radar. The partial beam blocking to the west of the radar causes under-estimation to be observed (red ellipse).... 17	17

## LIST OF FIGURES

---

Figure 2-8: The radar at Irene detecting storms to the east and north. Reflectivity to the west is a result from radiation being reflected off the buildings (Figure 2-6) towards the storms to the east while the radar is facing west.....	18
Figure 2-9: The effects the reflection (shown in Figure 2-8) can cause on the precipitation field. .....	18
Figure 2-10: The 3.4° PPI illustrating a ring of higher reflectivity as the beam propagates through the melting layer. Clearly illustrating the bright-band.....	20
Figure 2-11: A 24 hour precipitation accumulation illustrating rings of over-estimated precipitation caused by bright-band interference. ....	21
Figure 2-12: The 0.5° PPI display of uncorrected reflectivity data (a) illustrating ground clutter from the Irene S-band radar. After the Doppler filter has been applied (b) most of the clutter has been remove. When extracting the 3km AMSL CAPPI (c) results in virtually no clutter to be present when converting the estimates to precipitation. ....	22
Figure 2-13: Example of Anomalous Propagation showing radar reflectivities in dBZ before (a) and after (b) Doppler filtering. The Velocity field (c) in $\text{ms}^{-1}$ indicates $0\text{ms}^{-1}$ over most of the area inside the red oval. The $0\text{ms}^{-1}$ velocities is a clear indication that the beam is hitting the ground. Thus, the Doppler filter attempts to remove the reflectivities associated with it.....	23
Figure 2- 14: A graphic illustration of how a 2km CAPPI will be interpolated from volumetric data sampling (van Heerden and Steyn, 1999).....	26
Figure 3-1: The Flowchart indicating the processes involved in calculating the enhanced QPE. .....	36
Figure 3-2: A flowchart illustrating the process of classifying a given reflectivity pixel as convective or stratiform precipitation. ....	39

## LIST OF FIGURES

---

- Figure 3-3: The reflectivity difference  $\Delta Z$  compared to Mean Background Average  $Z_{bg}$ , with  $Z_c$  selected at 35 dBZ. If the difference  $Z - Z_{bg}$  is above the green line the pixel will be classified as a convective centre, below the line it will be a stratiform classified value..... 40
- Figure 3-4: A graphical representation of the classified pixel (green), the mean background average (grey) and convective radius (red). Pixels are included for calculations when the pixel centre is within the determined radii..... 40
- Figure 3-5: The classified field on 28 October 2010 at 02:29:16 UTC the corresponding instantaneous reflectivity field. .... 42
- Figure 3-6: Flowchart illustrating the process to calculate motion vectors from two consecutive radar scans using an optical flow method ..... 43
- Figure 3-7: Plotting constraint lines with noiseless (a) and noisy (b) data. .... 47
- Figure 3-8: Velocity vectors on 28 October 2010 at 02:29:16 UTC, calculated from the OFC equation indicating the direction and speed of the reflectivity field. .... 51
- Figure 3-9: A one hour accumulation using dual Z-R relationships on 28 October 2010 at 03:00:00 UTC. Stratiform classified precipitation makes use of Marshall-Palmer ( $Z=200R^{1.6}$ ), while convective classified precipitation is converted with the convective Z-R relationship ( $Z=300R^{1.4}$ )...... 52
- Figure 3-10: A schematic representation of the accumulation scheme. If the advection were not taken into account, the pixel at  $SP$  would not receive any precipitation during this scan interval. The figure illustrates the location of a precipitation cell in two consecutive radar scans ( $Rt1$  and  $Rt2$ ). The motion vector  $V_p$  illustrates the direction and speed of the precipitation cell. The total rainfall on the pixel located at  $SP$  is the weighted sum of the integrals along the paths  $SP|t - St1$  and  $St2 - SP|t$  ..... 54

## LIST OF FIGURES

---

- Figure 3-11: The figure illustrates an example of the percentage overlap for any given iteration of the integral. The pixel value is calculated by weighting the corresponding ground values.... 55
- Figure 3-12: The same one hour accumulation illustrated in Figure 3-9 on 28 October 2010 at 03:00:00 UTC. The figure illustrates the difference after the accumulation technique was applied..... 55
- Figure 4-1: A map illustrating the locations of the 1254 SAWS ground precipitation observation network..... 58
- Figure 4-2: The average precipitation for the rainfall season of October 2010 – March 2011 for the 8 station with WB42 data. The average total precipitation for each month (orange) is compared to the average total climatological precipitation (blue). ..... 61
- Figure 4- 3: Locations of rain gauge that made it through Quality Control (QC) within a 300km radius of the Irene radar. Red gauges are only capable of daily totals while blue gauge are capable of an hourly temporal resolution..... 62
- Figure 4-4: The Irene METEOR 600S S-band radar during construction in 2009, (a) and (b), as it stands today (c) at the Irene WO just outside Pretoria, Gauteng. .... 64
- Figure 4-5: The Enterprise C-band Radar at Bloemfontein illustrating signs of attenuation. A sector of lower reflectivity is observed directly to the West of the storm (relative to the radar) compared to the surrounding region. This sector is mark by the red lines..... 68
- Figure 4-6: Reflectivities from a storm detected by the Enterprise C-band Radar at Bloemfontein show signs of attenuation. The location of the storm relative to the radar is illustrated in (a). Hail inside the storm (b) is causing significant attenuation, so part of the storm away from the radar is significantly underestimated. This region is pointed out by the arrow marked A. Note the high reflectivities in the core in the range 65 – 70 dBZ. .... 68

## LIST OF FIGURES

---

Figure 4-7: Radar displays showing RLAN interference at Irene, Durban and Port-Elizabeth radars.....	70
Figure 4-8: Example of the Port Elizabeth running with the filter (Left), and without (Right). The two image are five minutes apart.....	71
Figure 4-9: An illustration of the height AMSL with range of each elevation in the radar scan strategy (blue line). .....	72
Figure 4- 10: An illustration of the height above AMSL with range of each elevation in the radar scan strategy (blue line). The extracted CAPPI levels are represented by the red lines. The grey rectangle illustrates the region of 17 – 73 km range from radar where all the CAPPI levels are comparable to rain gauges, which lie below the cylinder. ....	75
Figure 4- 11: Range gauges locations within 17 – 73 km range from radar where all CAPPI levels are comparable to the rain gauges.....	77
Figure 4- 12: A sequence of plots separated by a range interval of 30km. The plots illustrate the gauge distribution between each range interval. The number in parenthesis shows the number of each gauge type available.....	78
Figure 4-13: The format of a contingency table constructed by the use of thresholds. ....	80
Figure 5-1: The 5 minute rain rate data recorded at the automatic rainfall stations of Wonderboom Airport (a) and Springs (b). The graphs show the recorded rain rate from the gauge for the period 2010-12-15 00h00 to 2010-12-16 23h55 (UTC). The traces are blue when the classification of the radar is null, red when classified as stratiform and green when the classification algorithm chose convective rainfall. ....	85
Figure 5-2: The average VPR for Wonderboom Airport. An hourly average of the VPR was calculated and plotted for each hour in which every radar scan above the pixel located at the station was classified as convective. The freezing level identified by the radiosonde launched	



## LIST OF FIGURES

---

from the Irene WO is also plotted (red line). The graphs are all classified as convective because of the vertical structure of the reflectivity below the freezing level where the reflectivity is near 40 dBZ. In the graphs (a), (b) and (c) the dates correspond to the title..... 87

Figure 5-3: The average VPR for Springs ARS. An hourly average of the VPR was calculated and plotted for each hour where every radar scan within the hour, the corresponding pixel located at the station, was classified as stratiform. The freezing level from the radiosonde balloon ascent data launched from Irene WO is also plotted (red line). The graphs are all classified as stratiform. In the graphs (a), (b) and (c) the dates correspond to the title..... 88

Figure 5-4: The average VPR for Springs ARS. An hourly average of the VPR was calculated and plotted for each hour where every radar scan within the hour, the corresponding pixel located at the station, was classified as convective. The freezing level from the balloon ascent data done at Irene WO is also plotted (red line). The graphs are both classified as convective. In the graphs (a) and (b) the dates correspond to the title. .... 89

Figure 5-5: Scatterplot for the hourly (a) and daily (b) radar and contemporaneous gauge measurements for the whole study period October 2010 to March 2011. The blue dashed line represents the linear fit, while the black line represents a perfect fit of  $y=x$ . The associated correlation, bias and RMSE for the entire study period are also shown. .... 91

Figure 5-6: Continuous variable scores on a monthly basis for the October 2010 – March 2011 study period are illustrated. The correlation coefficient (a) for hourly and daily measurements is shown. The BIAS and Root Mean Square Error (RMSE) for one hour accumulations (b) as well as daily accumulations (c) are shown. The blue to green bars represents the changes through each month. .... 92

Figure 5-7: Gauge (blue) and radar (red) hourly accumulation (a) and daily accumulation (b) for the study period of October 2010 – March 2011. The associated Cumulative Distribution Function (CDF) considering only measurement that are not zero, are also illustrated in the lower panels, in which the cumulative fraction ranges from 0 to 1 and the horizontal axes are logarithmic scales..... 96

## LIST OF FIGURES

---

<p>Figure 5-8: Examples of the 3 algorithms (TITAN, CRR and OFRR) hourly accumulations. The rows represent each algorithm with the TITAN algorithm at the top, CRR in the centre and OFRR at the bottom. Each column is an event and time stamps are valid for the end of the accumulated period. The 3.0km CAPPI was selected to represent the CRR and OFRR algorithms.....</p>	98
<p>Figure 5- 9: Examples of the 3 algorithms (TITAN, CRR and OFRR) daily accumulations. The rows represent each algorithm with the TITAN algorithm at the top, CRR in the centre and OFRR at the bottom. Each column is an event and time stamps are valid for the end of the accumulated period. The 3.0km CAPPI was selected to represent the CRR and OFRR algorithms.....</p>	99
<p>Figure 5-10: Gauge, TITAN algorithm and CRR algorithm at all CAPPI levels for hourly accumulation (a) and daily accumulation (b) for the study period of October 2010 – March 2011. The associated Cumulative Distribution Function (CDF) considering only measurement that are not zero, are also illustrated in the lower panels, in which the cumulative fraction ranges from 0 to 1 and the horizontal axes are logarithmic scales. ....</p>	110
<p>Figure 5-11: The correlation coefficient at range intervals for the TITAN algorithm and CRR algorithm at all CAPPI levels for hourly accumulation (a) and daily accumulation (b) for the study period of October 2010 – March 2011. The grey bars indicate the number of gauges within each range ring.....</p>	111
<p>Figure 5-12: The bias at range intervals for the TITAN algorithm and CRR algorithm at all CAPPI levels for hourly accumulation (a) and daily accumulation (b) for the study period of October 2010 – March 2011. ....</p>	112
<p>Figure 5-13: The RMSE at range intervals for the TITAN algorithm and CRR algorithm at all CAPPI levels for hourly accumulation (a) and daily accumulation (b) for the study period of October 2010 – March 2011. ....</p>	112

## LIST OF ABBREVIATIONS

---

AMSL	-	Above Mean Sea Level
AP	-	Anomalous Propagation
ATI	-	Area-Time Integral
ARS	-	Automatic Rainfall Stations
AWS	-	Automatic Weather Stations
BPRP	-	Bethlehem Precipitation Research Project
BEWMEX	-	Bethlehem Weather Modification Experiment
BoM	-	Bureau of Meteorology
CBD	-	Central Business District
CRR	-	Classified Rain Rate
CAPPI	-	Constant Altitude Plan Position Indicator
CRA	-	Contiguous Rain Area
COTREC	-	Continuity of TREC
CSI	-	Critical Success Index
DARAM	-	DAily RAInfall Mapping over South Africa
DISPLACE	-	Digital Signal Processing for Logarithmic, Linear and Quadratic Responses
DSD	-	Drop Size Distribution
DFS	-	Dynamic Frequency Selection
ETS	-	Equitable Threat Score
FAR	-	False Alarm Ratio
FMQ	-	File Message Queue
FFGS	-	Flash Flood Guidance System
HSS	-	Heidke Skill Score
HE	-	Hydro-Estimator
HPC	-	High Performance Computer
HRC	-	Hydrologic Research Centre
ICASA	-	Independent Communication Authority of South Africa
MDV	-	Meteorological Data Volume
METSYS	-	Meteorological systems and technology section of the SAWB
NCAR	-	National Centre for Atmospheric Research
NDMC	-	National Disaster Management Centre
NPRL	-	National Physical Research Laboratory
NPRP	-	National Precipitation Research Programme

## LIST OF ABBREVIATIONS

---

NA	-	Not Available
NWP	-	Numerical Weather Prediction
OFC	-	Optical Flow Constraint
OFRR	-	Optical Flow Rain Rate
PDF	-	Probability Density Functions
PMM	-	Probability Matching Method
POD	-	Probability of Detection
PAWS	-	Programme to Augment Water
PRF	-	Pulse Repetition Frequency
QC	-	Quality Control
QPE	-	Quantitative Precipitation Estimation
RDF	-	Radio Direction Finding
RLAN	-	Radio Local Area Network
RMSE	-	Root Mean Square Error
SNR	-	Signal-to-Noise Ratio
SAAF	-	South African Air Force
SAFFG	-	South African Flash Flood Guidance system
SAST	-	South African Standard Time
SAWB	-	South African Weather Bureau
SAWS	-	South African Weather Service
SIMAR	-	Spatial Interpolation and MApping of Rainfall
SSS	-	Special Signals Services
SSS	-	Storm Severity Structure
TITAN	-	Thunderstorm Identification, Tracking and Nowcasting
TREC	-	Tracking Radar Echoes by Correlation
UM	-	Unified Model
VIPOS	-	Vaal dam catchment Integrated Precipitation Observing System
VOL	-	Gematronik volume format
VPR	-	Vertical Profile of Reflectivity
WRC	-	Water Research Commission
WPMM	-	Window Probability Matching Method

---

## CHAPTER 1

# BACKGROUND AND INTRODUCTION

---

### 1.1 Introduction

Weather Radar offers weather forecasters, scientists and the public an efficient means of measuring precipitation. Although its measurements are indirect it remains the best alternative in capturing the spatial variability associated with precipitation at a high temporal and spatial resolution. Flash floods are the number one cause of death and damage with regard to natural disasters in South Africa (Poolman, 2009). Thus, the South African Weather Service (SAWS) and the National Disaster Management Centre (NDMC) embarked on a collaborative project for the implementation of a flash flood warning system in flash flood prone regions, called the South African Flash Flood Guidance system (SAFFG) and was implemented in 2009 (de Coning & Poolman, 2011). The Flash Flood Guidance System (FFGS) is the intellectual property of the Hydrologic Research Centre (HRC), a non-profit public-benefit corporation based in San Diego, USA. SAFFG was developed and implemented by the HRC. The SAFFG is heavily dependent on accurate precipitation estimates from radar and, with the installation of the new Gematronik 600S S-band Doppler radar systems, much emphasis has been placed on the performance of the radar's Quantitative Precipitation Estimation (QPE) field. A methodology proposed by Chumchean et al. (2006) was selected to upgrade and improve the existing radar precipitation field. A rainfall classification algorithm has been introduced in this dissertation. This algorithm separates convective from stratiform precipitation with the intention of assigning different Z-R relationships to the two different classifications of rainfall (Chumchean, et al., 2008). A technique for smoothing accumulation of precipitation, which is based upon optical flow techniques (Bowler, et al., 2004), has also been introduced into the QPE algorithm.

### 1.2 The South African Flash Flood Guidance System

The SAFFG was operationally implemented in October 2010. The SAFFG monitors the soil moisture in 1633 small river basins that are about 50 km<sup>2</sup> on average. These basins are predominantly located in flash flood prone areas in South Africa. These areas surround the metropolitan area of Gauteng the Kwa-Zulu Natal province and the South Coast and being predominantly in highly populated areas near cities, are served by radars. The SAFFG makes use of real-time QPE data such as weather radar, satellite and rain gauges as input for the

hydrological modelling of the basin soil moisture. The most recent 24 hours of rainfall is used to calculate information such as soil moisture and run-off on an hourly basis. The SAFFG then determines the amount of rainfall needed per hour for each basin to cause flooding (de Coning & Poolman, 2011) and when it would be expected. Thus, the SAFFG depends heavily on the QPE products to be accurate as possible. The radar QPE is used as the primary precipitation input, thus the need to improve and include the best possible radar precipitation field was made clear by de Coning & Poolman (2011).

### 1.3 QPE at the South African Weather Service

South Africa is a water stressed country, thus accurately measuring the amount of precipitation is becoming increasingly more important for water management. During the winter months (June, July, August) precipitation is normally observed along the Southwest coastline of South Africa. During the summer months (December, January, February) the central and eastern parts of the country receive most of the country's annual rainfall. This is clearly illustrates in Figure 1-1 after Kruger (2007). The SAWS has a number of tools and infrastructure available that can help monitor and predict the amount of precipitation.

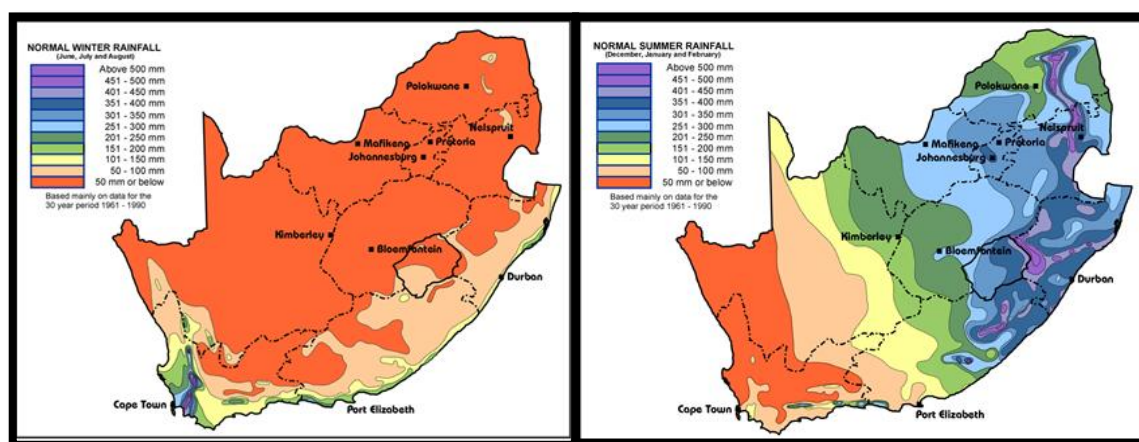


Figure 1-1: Normal winter (left) and summer (right) rainfall for South Africa (Kruger, 2007).

The SAWS currently coordinates the records of almost 1500 rain gauges. This includes data from Automatic Weather Stations (AWS), Automatic Rainfall Stations (ARS), Weather Offices and various observation stations. These instruments are mostly capable of daily measurements. However, 5 minute measurement intervals are available from the AWS and ARS stations. The rain gauge network will be discussed in more detail in chapter 4.

A local version of the UK-Met Office's Unified Model (UM) is also available at the SAWS. The regional model runs twice a day to give a precipitation forecast every hour for a 48 hour forecast. The model domain is between 0.48°N and 44°S, and 10°W and 56°E and runs on a horizontal resolution of 12 km over 38 vertical levels. By the end of 2014, a new High Performance Computer (HPC) will be installed at SAWS and the model will then be capable of running on a horizontal resolution of 4 km over 70 vertical levels (Landman et al, 2012).

The SAWS also has access to Meteosat Second Generation (MSG) data. Using the data from the 10.7  $\mu\text{m}$  brightness temperature channel together with variables such as temperature, precipitable water, etc. available from UM calculations quantitative estimates can be obtained. The software known as the Hydro-Estimator (HE) was developed by Kuligowski & Scofield (2003). The temporal resolution is 15 minutes and its domain and resolution is dependent on that of the UM. The biggest advantage of a satellite based precipitation estimates is that precipitation can be measured in data sparse regions.

The SAWS runs its own weather radar network which is one of the weather service's most expensive and valuable assets. In 2009 the SAWS upgraded the network to expand from ten C-band and two S-band radar, to eleven S-band, three C-band and two X-band radars. The SAWS is currently in the process of removing all C-band radars and migrating to S-band radars. The S-band has numerous advantages, which will be discussed throughout the dissertation. The current network was predominantly used for storm identification, weather prediction and aviation applications (de Coning et al., 2010). However, in recent years the demand for the QPE capabilities of weather radar has been dramatically increasing. The basic reflectivity conversion to rain rate using the Marshall and Palmer Z-R relationship was not sufficiently accurate anymore. More accurate and modern QPE techniques were being sought after.

## **1.4 Aims and Approach of this Research**

The main aim of this dissertation is to improve on the current QPE algorithm available at the SAWS. This can be done by incorporating some of the latest techniques in radar QPE. To achieve this aim the following objectives were defined:

- To introduce instantaneous precipitation classification. To apply different Z-R relationships for convective and stratiform classified rainfall.
- To account for storm movement between successive scans by integrating precipitation over a computed vector path that is based upon optical flow techniques.
- To determine how these techniques mentioned above perform on different altitudes of reflectivity.

These objectives are addressed by:

- Incorporating a 2 dimensional classification scheme (Chumchean et al., 2008).
- Using optical flow to calculate motion vectors between successive scans (Bowler et al., 2004; Sinclair, 2007)
- Using a dual Z-R relationship to convert reflectivity to rain rate (Chumchean et al., 2008).
- Accumulation through morphing with motion vectors (Hannesen, 2002; Sinclair, 2007).

Important research questions can be inferred from the research objectives above. These are:

- Can the classification scheme accurately distinguish between convective and stratiform precipitation?
- Is the dual Z-R relationship an improvement compared to the existing precipitation algorithm?
- Does the smoothing of precipitation accumulations using optical flow techniques further improve the precipitation algorithm?

Two algorithms will be set up to compare to the current precipitation algorithm. One uses the classification technique and a dual Z-R relationship denoted as the Classified Rain Rate (CRR) and the other is a similar algorithm adding the optical flow vectors to the accumulated totals. This combination algorithm will be called the Optical Flow Rain Rate (OFRR) algorithm. Each algorithm will be compared with one another in order to determine which technique improves traditional radar rainfall estimates.

## **1.5 Summary**

The importance of accurate precipitation measurements and early warning systems such as the SAFFG is becoming more and more significant to warn the public of extreme types of weather events. There is evidence to suggest that these extreme events will increase in frequency (IPCC, 2007). Thus, improving the accuracy in which radar precipitation is measured can have a tremendous impact on the value of these early warning forecasts. The remainder of this document will focus on radar precipitation. The next chapter, chapter 2, will discuss the history of radar in South Africa, the SAWS radar network and the different techniques involved in estimating radar precipitation. Chapter 3 will discuss the algorithm developed to implement the techniques introduced in section 1.4. Chapter 4 looks into the advantages and limitations of the radar data as well as the rain gauge data used for the evolution of the precipitation algorithm.



The evaluation method is also discussed in detail. Chapter 5 will list the findings of the research done and the conclusion reached will be discussed in Chapter 6.

---

## CHAPTER 2

# RADAR RAINFALL MEASUREMENTS

---

### 2.1 Introduction

In this chapter the history of the development of weather radar in South Africa is summarised from its early uses in cloud seeding experiments to its role in Quantitative Precipitation Estimation (QPE) in recent years. The new radar network (of which the first radar was installed at the end of 2009) is described, singling out the S-band radar at Irene as the main focus of the study. Basic radar theory is outlined to support the weather radar's ability to measure precipitation.

The Australian Bureau of Meteorology (BoM) precipitation estimation methodology is then presented. It was selected by the South African Weather Service (SAWS) in 2010 to enhance the precipitation estimates from radar-derived reflectivities. The remainder of the chapter discusses the three steps in the methodology that include (i) reflectivity measurements, (ii) Z-R conversion and (iii) rain gauge adjustment. Basic radar theory is introduced to help explain the complex and inherently difficult task of radar precipitation estimation.

### 2.2 Weather Radar Development in South Africa

The roots of weather radar lie in radio. The first proposal to use radio waves for target detection was made as far back as 1922. However, it was not until the start of the 2<sup>nd</sup> World War in 1939 that the development of radar really took off. Used primarily as an early warning system to detect aircraft, operators often observed noise that came from weather phenomena like rain, hail, snow, etc. By the end of the War, radar had been thoroughly developed and scientists interested in studying the weather were some of the first to acquire the surplus military radars (Reinhart, 2004).

South Africa had its first radar build in 1939 under the leadership of Dr Basil Schonland of the Bernard Price Institute of Geophysical Research at the University of the Witwatersrand. Hewitt (1975) and Austin (1992) give an interesting and detailed account of this event. At the start of the war the British Government informed its commonwealth countries of the existence of a radio direction finding (RDF) apparatus, as it was known at the time, and requested that senior scientists from each country travel to Britain and familiarise themselves with the system. South African scientists were unable to attend but it had been arranged that Dr Ernest Marsden,

from the New Zealand Department of Scientific and Industrial Research, return to New Zealand via Cape Town. Here he met up with Dr Schonland and briefed him on the RDF system. Armed with Dr Marsden's knowledge and a vague photocopied manual Dr Schonland set out, using only local components, to build the radar. As a result the first radar echo was received on the 16<sup>th</sup> of December 1939, which was by chance, from the Johannesburg landmark known as the Northcliff Water Tower. The radar operated with a peak power output of 5 kW, with a pulse length of 20  $\mu$ s, a pulse repetition frequency (PRF) of 50 Hz and a wavelength of 3.5 m. The radar was known as JB0 and was operational within 3 month of Dr Schonland's meeting with Dr Marsden.

The South African radar team became known as the Special Signals Services (SSS). Upgrades of the JB0 were then deployed to East Africa as well as the Middle East to aid in the defensive efforts during the war. A further twelve radars were deployed along the coast of South Africa to aid with defence. In April 1942 British radar equipment finally arrived and replaced the JB series radars. By 1943 two Royal Navy type-273 radars were installed on Signal Hill and at Cape Point to monitor shipping. These radars greatly enhanced the capability of the coverage previously provided by the JB radars.

After the war, junior members of Dr. Schonland's team formed the Telecommunications Research Laboratory (a division of the CSIR) and conducted the first cloud seeding experiments over South Africa. During the summer of 1947-1948 they dropped dry ice into the tops of 36 cumulus clouds using aircraft supplied by the South African Air Force (SAAF). A 3cm wavelength X-band radar built at the Telecommunications Research Laboratory station in Johannesburg was then used to monitor the seeding effects. This was the first time radar was used in meteorological studies in South Africa (CSIR, 1948)

In 1971 the CSIR Atmospheric Physics Division brought into operation a Mitsubishi S-band radar for the National Physical Research Laboratory (NPRL) hail studies project. The radar was located at Houtkoppin in Randburg and for the first time the three-dimensional structure of storms could be observed. This led to numerous documented case studies of hail producing storms (Held and Carte 1973; Carte and Held, 1978; and Held 1978 and 1982). The studies highlighted that airflow measurements around these storms are essential for the understanding of these storms. Held (1982) showed how one storm can produce > 5cm hail while a remarkably similar storm can produce heavy precipitation but no hail. Thus, the S-band radar was upgraded to a Doppler system that could detect radial velocities of the hydrometeors. The first Doppler velocity observations were made at the end of the 1986/1987 season (Dicks et al, 1987). A C-band radar installed at Pretoria, which was also a Doppler system, made observations of storm velocity simultaneously with the S-band in Houtkoppin in March 1991

(Held and Gomes, 1992). Shortly afterwards funding was terminated for the project and the CSIR involvement with radar research ended with Hodson's (1993) thesis on radar-rainfall studies.

Since the 1950's the South African Weather Bureau (SAWB) used radar primarily to track upper-air balloons. Only in the 1970s did the SAWB focus shift towards cloud seeding experiments. A Mitsubishi RC 4B C-band radar was installed at Bethlehem in 1971 as part of the Bethlehem Weather Modification Experiment (BEWMEX) (Harrison, 1974). A report on radar observation during the 1978-1979 summer season was compiled by Fletcher (1980).

The name of the project was changed to the Bethlehem Precipitation Research Project (BPRP) in the 1980's and the Enterprise WSR-81 C-band radar was installed at Bethlehem in 1982. The BPRP main focus was to continue to monitor the effect of cloud seeding over the Bethlehem area (Krauss et al, 1987; Gagin et al, 1986). The data captured was also used for storm climatology studies such as storm movement, storm lifetime, etc. (Steyn and Brintjies, 1990; Mather and Terblanche, 1993). Data was also used for studies on evaporation of rainfall between the convective cloud and the ground (Rosenfeld and Mintz, 1988) as well as factors that contribute to the total rainfall yield from convective clouds (Rosenfeld and Gagin, 1989).

At the same time, the Water Research Commission (WRC) carried out a similar seeding project that ran for 3 years starting in 1984. The project was known as the Programme to Augment Water Supplies (PAWS) and a Pacer III C-band radar was used over the Nelspruit area. Mather et al. (1996) give a thorough description of the programme as well as the results from the experiments. The programme was also the birth place of the automatic storm tracking algorithm, which would later be known as the Thunderstorm Identification, Tracking and Nowcasting (TITAN) tracking algorithm (Dixon, 1977; Wiener and Dixon, 1993).

In 1990 the National Precipitation Research Programme (NPRP) was formed. This allowed for a co-operation between the PAWS and BPRP research groups. With their combined efforts quick progress and major advances with cloud seeding experiments was made. One of which was the development of hygroscopic flares. During the 1990-1992 study period the Enterprise C-band radar at Bethlehem was used (Mather and Terblanche, 1993). The radar had limitations that were identified by the project team that included attenuation. The MRL-5 dual-wavelength radar operated in the S- as well as the X-band frequencies due to a unique antenna system was procured to eliminate this limitation. This radar was installed in Bethlehem and would play a pivotal role in radar research for South Africa over the next few years. The 1993/1996 study period would be the final experiment done on cloud seeding by the NPRP, and over South Africa as well (Mather and Terblanche, 1996). The Digital Signal Processing for Logarithmic, Linear and Quadratic Responses (DISPLACE) method was also developed by

Terblanche (1996) during the NPRP. It was originally developed to facilitate the averaging of digitized logarithmic receiver output, but later the method was found to be ideally suited for many other processes, one of which was a more efficient way to calculate Constant Altitude Plan Position Indicator (CAPPI) data (Mittermaier and Terblanche, 1997).

The MRL-5 radar remained in operation after the conclusion of the NPRP but the research focus shifted more toward hydrological applications due to water management concerns. Van Heerden and Steyn (1999) used the radar to develop a greater understanding of the space-time characteristics of convective precipitation and also develop a means of communicating the radar based rainfall to potential users with the view to satisfying hydrological requirements. From this Visser (1999) developed the Storm Severity Structure (SSS) method to help determine the structure and intensity of convective storms. Mittermaier (1999) also developed algorithms that attempt to improve rainfall estimates where bright band interference was possible.

In 2001 the Vaal dam catchment Integrated Precipitation Observing System (VIPOS) project came to an end (Terblanche et al., 2001). This project saw many changes within the SAWS (in 2001 the South African Weather Bureau (SAWB) name changed to South African Weather Service (SAWS)) and also contributed to major advances in Radar precipitation. The merging of the scientific groups in Pretoria and Bethlehem was the start of Meteorological systems and technology section of the SAWB or METSYS for short. This had the advantage of being the sole entity responsible for the National Radar Network, both scientific and technical. With the MRL-5 radar at Bethlehem, the two Enterprise C-band radars at Irene and Ermelo and the Liebenbergsvlei catchment rain gauge network, VIPOS made it clear that the advantages of a radar network's high spatial and temporal resolution had no comparison. This led to the TITAN system being deployed at all the radars in the network. VIPOS also showed that radar rainfall estimations can be improved by adjustment with rain gauge measurements. It also laid the ground work for merging of radar and gauge data which was utilized by the Spatial Interpolation and Mapping of Rainfall (SIMAR) project.

The purpose of the SIMAR project, funded by the Water Research Commission (WRC), was to produce a daily rainfall map of South Africa by merging gauge, satellite and radar precipitation. The project was divided in three parts. The maintenance and upgrading of radar and rain gauge infrastructure (Kroese, 2004) was the first part. The second part focussed on optimising the radar and satellite derived rainfall and then ultimately combining the three precipitation fields (Deyzel et al., 2004). The third part addressed the complex mathematical problem of combining the three fields (Pegram, 2004). An original method of Kriging, exploiting the Fast Fourier Transform, was developed by Pegram (2004) to optimally

integrate/merge the data fields to produce a daily rainfall map. The DAily RAInfall Mapping over South Africa (DARAM) project, also funded by the WRC, followed to improve on the advances made with SIMAR. Further methods of improving the infrastructure and radar coverage were investigated (Kroese et al., 2006). Additional techniques for improving rainfall estimation, as well as investigating method for near future forecasting (up to 2 hours ahead) were included (Pegram et al, 2006).

The daily rainfall map that was generated using the radar network from the DARAM project unfortunately halted at the end of 2006. This was due to a number of factors but the most important was the loss of many key personnel that were required to maintain and upgrade the system. The MRL-5 radar at Bethlehem became outdated and spare parts were no longer available to sustain operation. Perhaps the most severe blow to the project was the appearance of Radio Local Area Network (RLAN/WIFI) devices. As explained in more detail in chapter 4 section 4.3.2, these RLAN devices caused interference on the C-band operating frequency, effectively rendering the radar data useless for hydrological purposes. This resulted in the introduction of the South African Radar Improvement Project, which was officially launched in 2010. A description of the radar upgrades is found in the next section.

### **2.3 The Current Radar Network in South Africa**

The pre-2009 SAWS radar network consisted of eleven Enterprise C-band (5 +/- cm wavelength) radars of various ages (Terblanche et al., 2001). These radars were installed at Cape Town, Port Elizabeth, East London, Mthatha, Durban, De Aar, Bloemfontein, Bethlehem, Irene, Ermelo and Polokwane. A 2° Beam width EEC S-band radar was also installed at Skukuza. The increasing age of the radars led to numerous down times (periods during which the radar was not operating) due to mechanical and/or electronic failures. The difficulty of obtaining spare parts for an aging radar network was just one of the many reasons the SAWS radar improvement project was launched. The R240 million government funded project allowed for the purchase of 10 METEOR 600S S-band Doppler radars of which 1 would be Dual-Polarized and 2 would be mobile METEOR 50DX X-band radars which are capable of detecting Doppler winds and are also Dual-Polarized.

The radars were deployed to replace 8 of the eleven Enterprise C-band radars at Irene, Polokwane, Ermelo, Bloemfontein, Bethlehem, Durban, Mthatha and East-London. The remaining 2 S-band radars were deployed at Ottosdal and George to expand the radar network coverage where it was previously lacking. The Dual-Polarized S-band radar was deployed at Bethlehem. The radars at De Aar, Port Elizabeth and Cape Town would remain Enterprise C-band radars. The S-band radar at Skukuza would also remain operational. Table 2-1 gives a

summary of when each radar became operational, the operating frequency band and its capabilities.

*Table 2-1: This table illustrates the radar network of the SAWS. Listed are the date the radar was commissioned, the frequency it operates at and its capabilities.*

Radar	Date Commissioned	Frequency Band	Capabilities
Bethlehem	March 2010	S-band (10cm)	Doppler & Dual-Pol
Bloemfontein	July 2011	S-band (10cm)	Doppler
Cape Town	< 1998	C-band (5cm)	Reflectivity Only
Cape Town Int. Airport	Not yet active	X-band (3cm)	Doppler & Dual-Pol
De Aar	< 1998	C-band (5cm)	Reflectivity Only
Durban	May 2011	S-band (10cm)	Doppler
East-London	May 2011	S-band (10cm)	Doppler
Ermelo	November 2010	S-band (10cm)	Doppler
George	January 2012	S-band (10cm)	Doppler
Irene	January 2010	S-band (10cm)	Doppler
OR Tambo Int. Airport	Not yet active	X-band (3cm)	Doppler & Dual-Pol
Ottosdal	November 2010	S-band (10cm)	Doppler
Mthatha	March 2010	S-band (10cm)	Doppler
Polokwane	November 2010	S-band (10cm)	Doppler
Port-Elizabeth	< 1998	C-band (5cm)	Reflectivity Only
Skukuza	February 2007	S-band (10cm)	Reflectivity Only

Figure 2-1 illustrates the current SAWS radar network, displaying the different radar locations and the range they operate at, with respect to the South African provinces. The white range rings represent S-band frequency radars and the green rings the C-band frequency radars. The smaller rings are at a 200km range, while the bigger rings are at 300km. The radars located by a red dot do not have Doppler capabilities while the blue dotted radars do have Doppler. The turquoise colour dotted radar at Bethlehem includes both Doppler and Dual-Polarization capabilities. The location of the radar was originally selected to maximise storm surveillance and was not originally deployed with hydrological application in mind (Terblanche et al., 2001). Large convective systems have deep vertical dimension, which allows them to be observed, at

least partially, at longer ranges from the radar. Shallower precipitation from stratiform systems becomes difficult to detect at long ranges due to the radar beam quickly increasing in height and overshooting the upper levels of the rainfall (Terblanche et al., 2001). For these conditions, the radars should not be more than 150 km apart, because Collier (1986a, b) and Mylne and Hems (1991) recommend a nominal inter-radar distance of 75km for meaningful quantitative purposes.

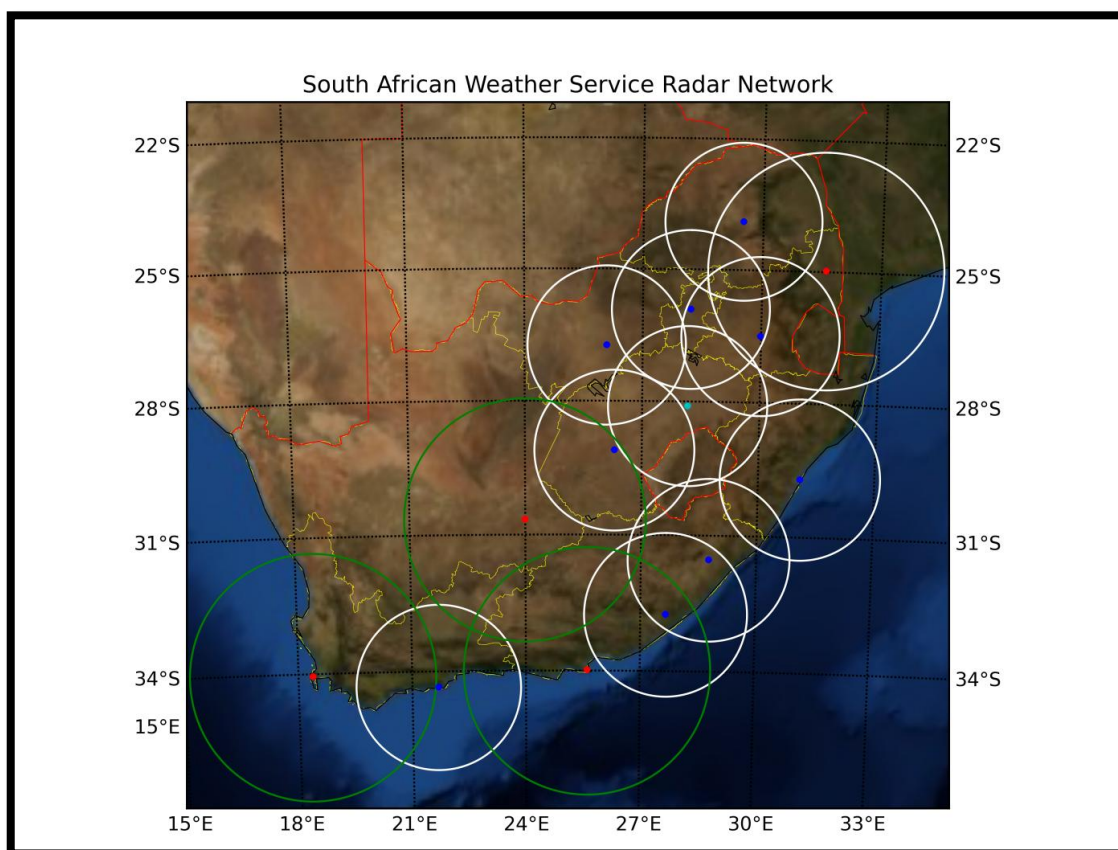


*Figure 2-1: The current SAWS operational radar network. The white range rings represents S-band frequency radars while the green rings the C-band frequency radars. The smaller rings are at 200km range while the larger rings are at 300km. The red dot radars do not have Doppler capabilities while the blue dot radar does have Doppler. The turquoise colour radar at Bethlehem includes both Doppler as well as Dual-Polarization capabilities. (X-band radar not include due to it not being operational. The radar will however be located at both CT int. Airport and OR Tambo Int. Airport.)*

## 2.4. Quantitative Precipitation Estimation

Why use radar rainfall? Radar remains the best tool for estimating rainfall over a large area and with high temporal resolution (5-10min). It is also the best means of producing short-term rainfall forecasts. The ever decreasing total number of reliable gauge data has made radar measurement more important than ever (van Heerden and Steyn, 1999). The concept of



estimating precipitation with radar involves careful consideration of measured reflectivities. Errors in precipitation estimation can result from errors in reflectivity measurements and Z-R conversion errors. Only through a thorough understanding of the limitations can the correction strategies be implemented successfully (Chumchean et al., 2006). The Australian Bureau of Meteorology (BoM) uses the procedure shown in Figure 2-2 to estimate real-time hourly radar rainfall estimates.

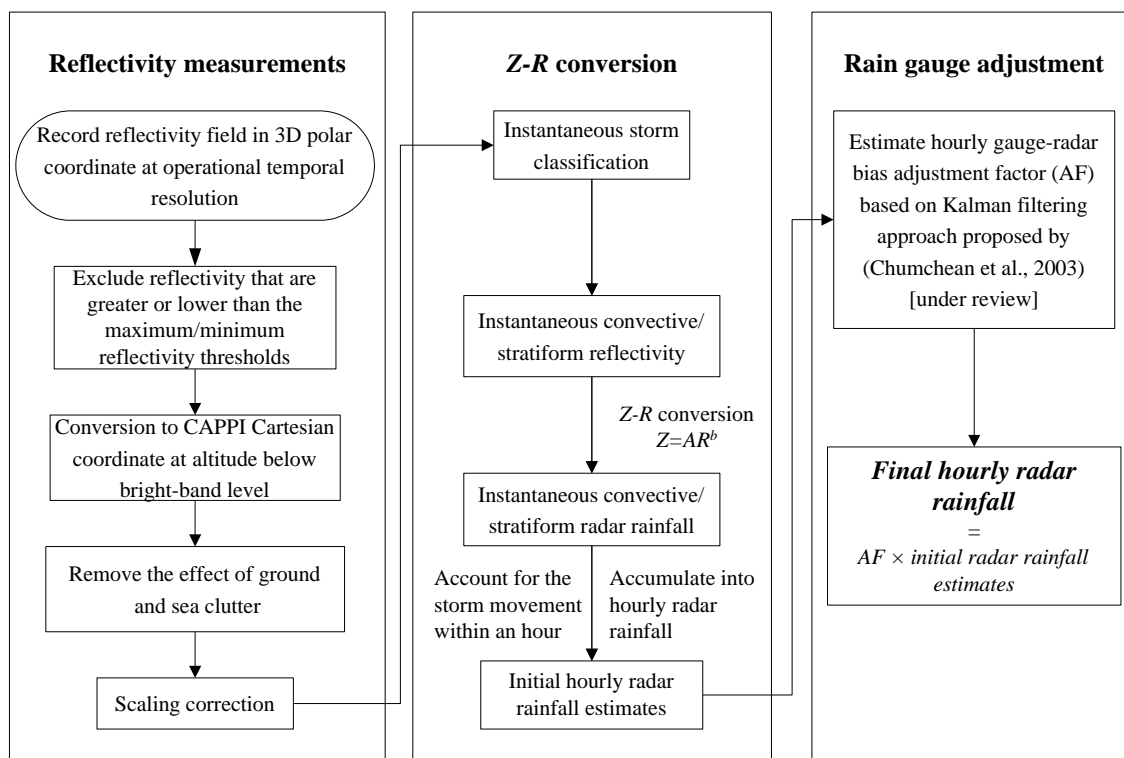


Figure 2-2: The Australian Bureau of Meteorology process for estimating 1 hour rainfall accumulations (Chumchean et al., 2006).

The process taken from Chumchean et al. (2006) involves 3 steps. The first is the correction of reflectivity measurements, the second is to introduce techniques to minimize the errors from Z-R conversions, and the third is a bias adjustment using rain gauge data. The SAWS also decided to adopt this process. However, this document primarily focuses on minimising errors from Z-R conversions.

### 2.4.1. Reflectivity Measurements

As seen in Figure 2-2 the radar reflectivity measurement needs to be carefully corrected and extracted before rainfall estimation can be calculated. These involve errors from ground and sea clutter, anomalous propagation, bright band, second trip echoes, beam blockage and scaling

effects to name a few. The next few sections will discuss some of these errors and their effects on reflectivity measurement in terms of estimating precipitation. In order to use the reflectivity measurement the data needs to be extracted from the volumetric scan stored in polar coordinates. Thus, Constant Altitude Plan Position Indicator (CAPPI) level will also be discussed.

### 2.4.1.1 Beam Blocking

When a radar beam strikes a fixed object like a building or mountain, it is said that the beam has undergone blocking. Correcting for beam blocking is not part of the study but is still a major source of error within precipitation estimation and it will be worthwhile understanding these effects better. In Figure 2-3, two types of beam blockage are possible. The first is, 1) partial beam blocking and the second 2) total beam blocking (Bech et al., 2002). Figure 2-3 only illustrates the concept of beam blocking. Partial beam blocking can result in power losses and precipitation can be severely under-estimated. Total beam blocking, block one hundred percent of the power and no precipitation can be detected beyond that range. Each radar has its own “finger print” when it comes to beam blocking that is dependent on the surrounding topography.

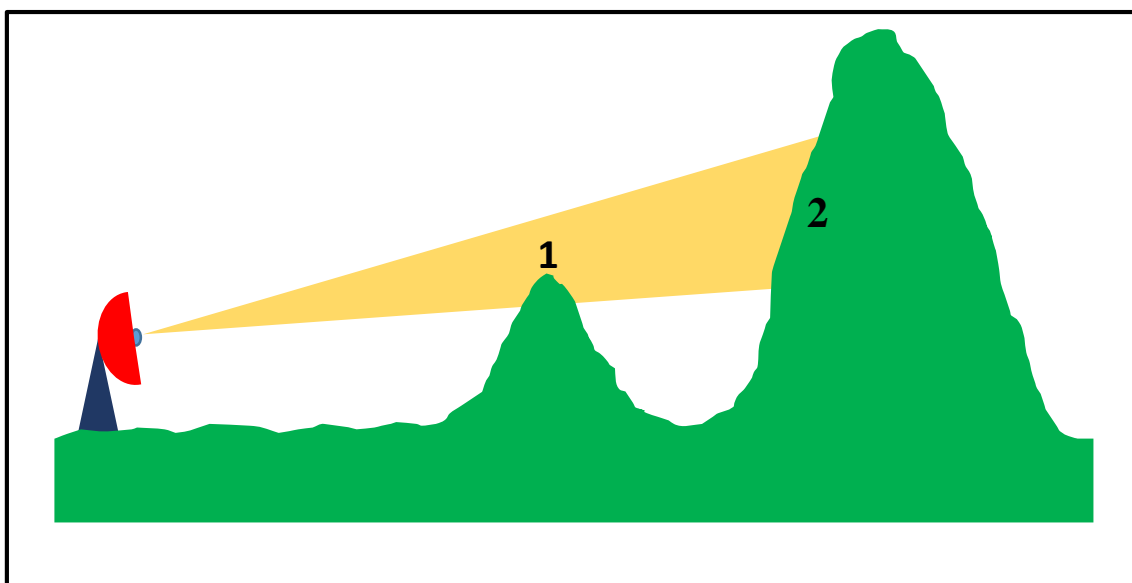


*Figure 2-3: A graphic illustration of 1) partial and 2) total beam blocking. It is assumed that atmospheric refraction and the curvature of the earth has no effect on the radar beam.*

Examples of beam blocking in a radar scan are shown in Figures 2-4 and 2-5. Figure 2.4 displays instantaneous composite reflectivities as measured by the East-London C-band radar in 2001. A section of shallow stratiform precipitation is present to the east of the radar over the Indian Ocean. Sectors of reduced to missing reflectivities are observed within this region of

stratiform precipitation. This is due to the terrain and structures surrounding the radar obscuring the lower elevation scans. This makes detecting low targets such as stratiform precipitation at long ranges very difficult.

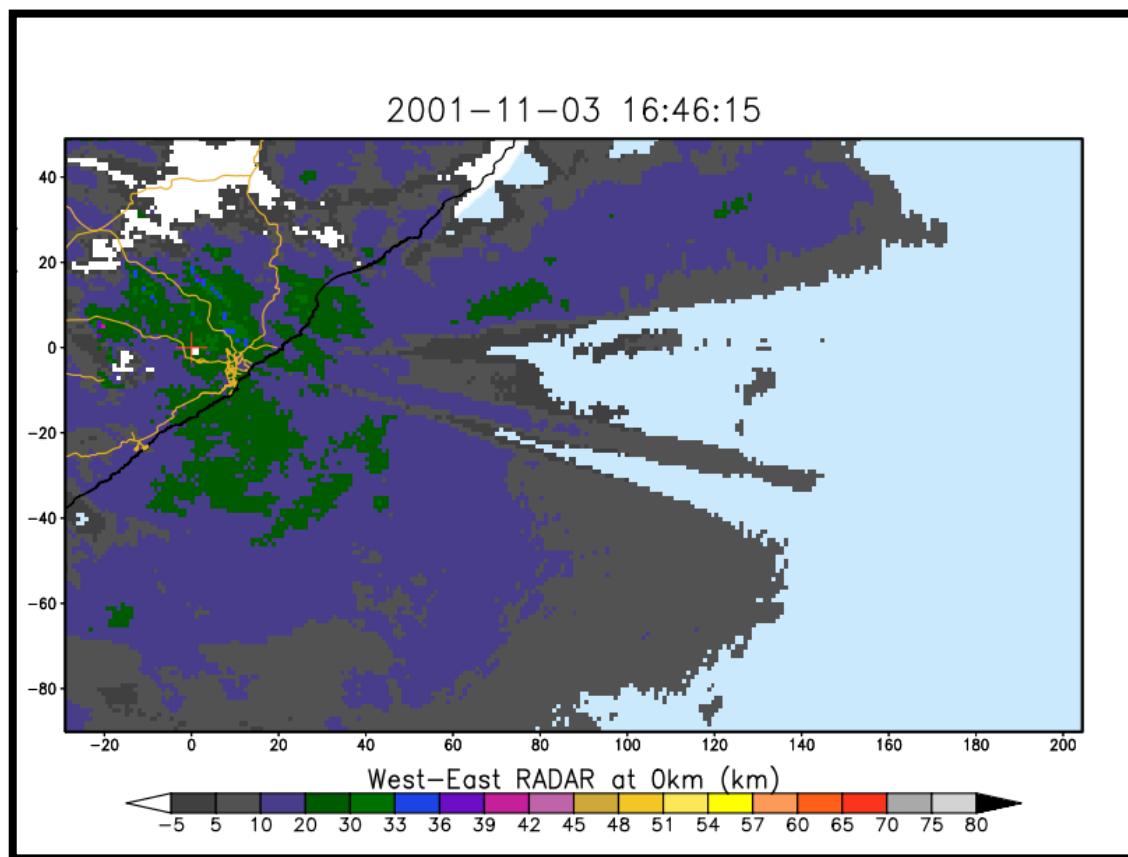


Figure 2-4: Instantaneous reflectivities at the East-London radar showing an example of beam blocking to the east of the radar.

Figure 2-5 illustrates the result when beam blocking is present in a precipitation field. The 24 hour precipitation field from the C-band radar at Irene was generated shortly after the S-band radar was constructed. The S-band radar is located around 100m to the south of the C-band radar and the resulting blockage caused by the S-band radar contributes to severely underestimated precipitation totals, which are clearly visible on the radar display. A large spike of apparently increased precipitation almost due south of the radar is also observed which is caused by RLAN interference.

The Irene S-band itself experiences partial beam blockage to the west of the radar due to the construction of large warehouse structure visible on the horizon from the Irene radar site. The structures are illustrated in Figure 2-6 with photographs taken from the top of the 15m tall radar tower. Figure 2-6 (a) illustrates and points out the largest building of the 3 structures with the arrow mark A. The structures located to the left and right from the structure in Figure 2-6 (a)

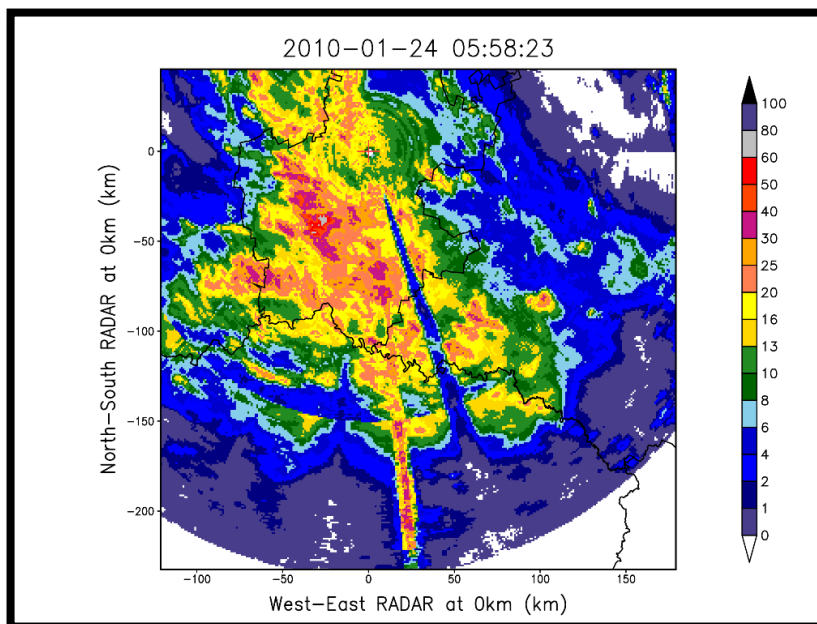


Figure 2-5: A 24 hour accumulation of the C-band radar after the installation of the new S-band radar at Irene. The S-band radar causes total beam blocking to the south of the radar resulting in severe under-estimation of precipitation, the large spike of apparently increased precipitation is caused by RLAN interference.

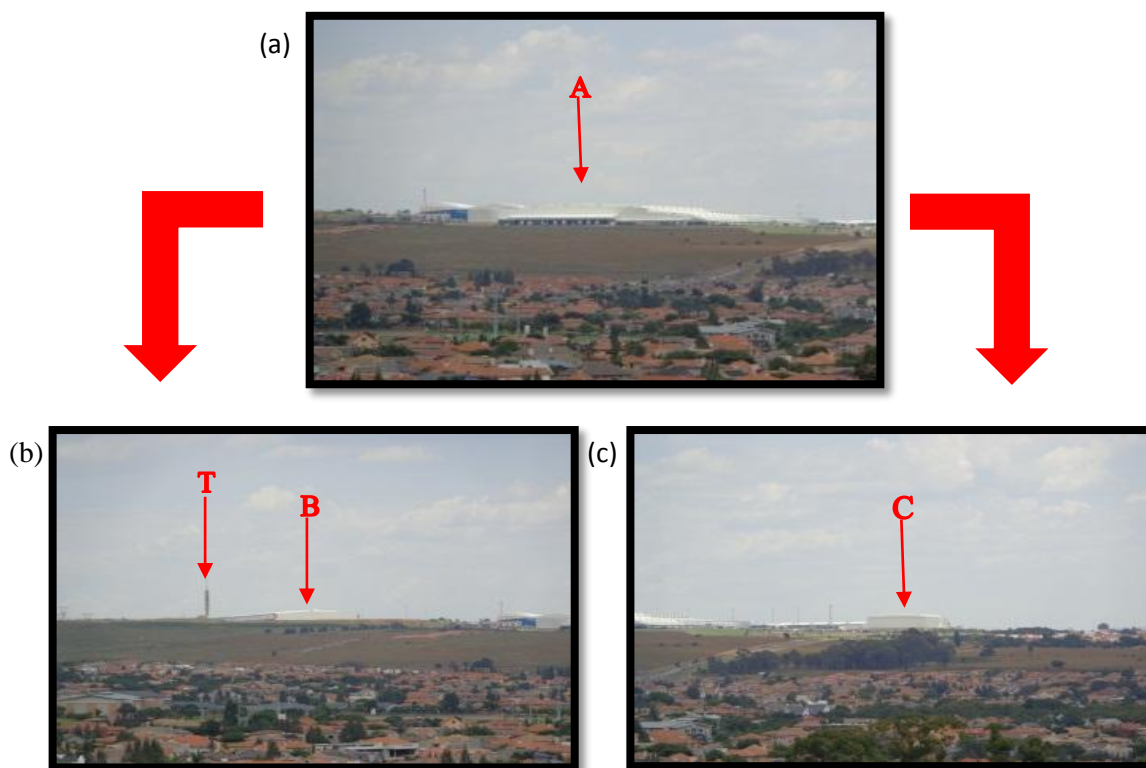
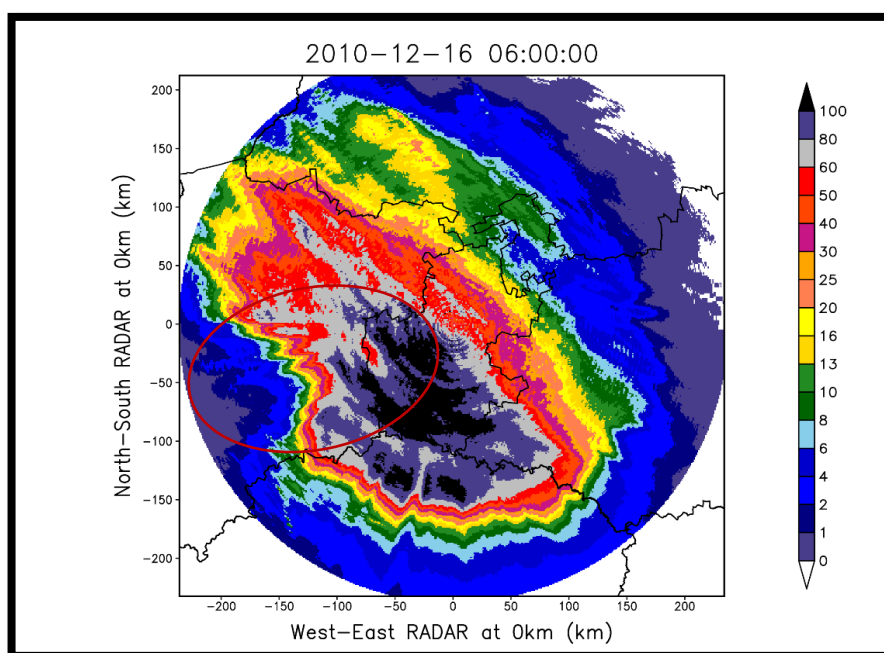


Figure 2-6: Images of the large warehouse structure as seen from the top of the S-band radar tower. The buildings are the cause of partial beam blocking as well as reflection of the electromagnetic wave.

are represented by Figure 2-6 (b) and Figure 2-6 (c). Figure 2-6 (b) also has a tower visible mark with the arrow T.

Figure 2-7 illustrates the effects these structures can have on precipitation estimates. On the 15<sup>th</sup> of December 2010, a day of significant flooding with wide spread precipitation, the 24 hour accumulation illustrates definite power losses to the west of the radar with low precipitation measurements. The effect from the partial beam blockage is aggravated with an increase in range.

A problem that is unique to the Irene S-band radar, in a South African context at least, is that the metal construction of warehouse buildings to the west of the radar not only causes blockages of the radar beam but also acts as a reflector and reflects electromagnetic radiation. Figure 2-8 displays 3 spiked like features to the west of the radar. During this time only storms to the north and east of the radar were present. The warehouse building reflected radiation to the east and the radar measured a power return with the receiver of the antenna pointing to the west, resulting in a false echo being detected. Figure 2-9 shows the effect it can have on the precipitation product.



*Figure 2-7: A 24 hour accumulation of precipitation for the Irene S-band Radar. The partial beam blocking to the west of the radar causes under-estimation to be observed (red ellipse).*

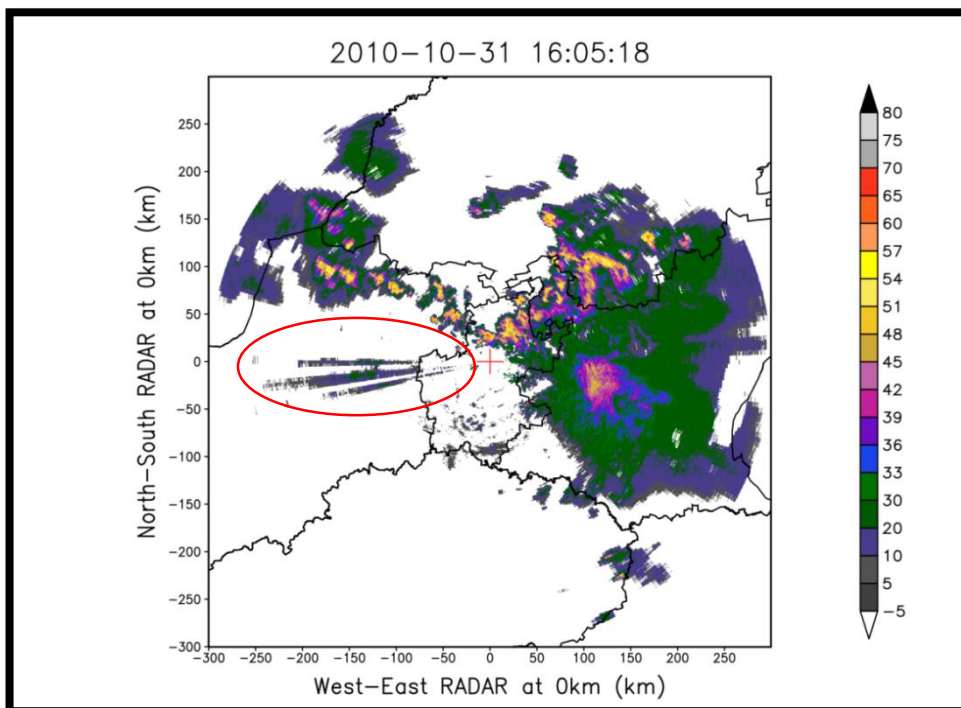


Figure 2-8: The radar at Irene detecting storms to the east and north. Reflectivity to the west is a result from radiation being reflected off the buildings (Figure 2-6) towards the storms to the east while the radar is facing west.

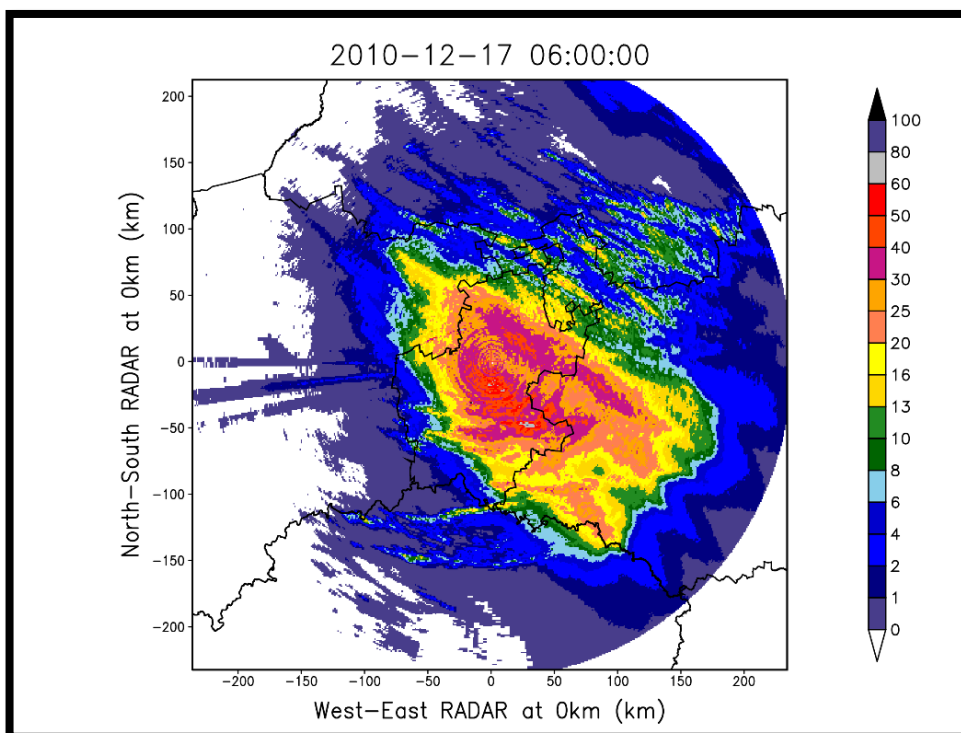


Figure 2-9: The effects the reflection (shown in Figure 2-8) can cause on the precipitation field.

Clearly the effect of beam blocking can be severe. Normally these blockages only affect the lowest level of the volume scan but it is also the most useful scan in terms of precipitation estimation at ground level (Collier, 1996). Thus most operational QPE's include correction algorithms for example, Harold et al. (1974), Kitchen et al. (1994), Joss and Lee (1995), Fulton et al. (1998), Chumchean et al. (2006) and Zhang et al. (2011). Zrníc and Ryzhkov (1998) also point out the advantage that Dual-Polarised products (like differential phase) can have over single polarisation radars in terms of estimating precipitation under beam blocking conditions.

#### **2.4.1.2. The Bright-Band**

Observations of a uniform band of higher reflectivities just beneath the zero-degree isotherm (freezing level), is known as the bright-band, so named due to its brighter appearance on the older radar displays and was first presented by Ryde (1946). The higher reflectivities are as a result of several characteristics of electromagnetic waves and hydrometeors within the atmosphere, such as the differences of ice and water with regard to their (i) reflective properties (dielectric constant), (ii) density above and below the melting level and (iii) terminal velocity (Battan, 1973).

This phenomenon is observed in more organised stratiform precipitation, where there is a clear distinction in particles between different layers in the atmosphere. When particles precipitate from the cloud and the ice particles move through the melting layer they start to melt from the outside inward. Equation 2-1 relates the backscattering cross-sectional area ( $\sigma$ ) of the hydrometeor, to  $|K^2|$  the dielectric constant,  $D$  the diameter of the hydrometeor and  $\lambda$  the radar wavelength. The backscattering cross-sectional area is the surface area of the hydrometeor relative to the radar. In the Rayleigh and Mie region (when the diameter of the hydrometeor is much smaller or close to the length of the radar wavelength) this area can differ significantly from the physical area of the hydrometeor. The hydrometeor type is also a factor. Thus, since the dielectric constant  $|K^2|$  in Equation 2-1 of water is 0.93 compared to ice of 0.192, an ice particle with a water coated surface will appear much larger and reflect more radiation back to the receiver of the radar. The reflectivity is much more dependent on the size of the particle than the number of particles in a sample volume. Thus the larger water coated ice particle can result in an increase of up to 7dB (7 Decibel) in return power. When the particles melt completely the size reduces and the terminal velocity increases, resulting in the particle to fall away from the melting layer faster. This causes a decrease in the measured power. The result is a band of higher reflectivities just underneath the freezing level (Reinhart, 2004).



$$\sigma = \frac{\pi^5 |K|^2 D^6}{\lambda^4} \quad (2-1)$$

Figure 2-10 illustrates an example of the bright-band observed at the Irene radar. The 3.4° elevation scan displays a ring of higher reflectivity at a range close to 50 km from the radar. At the 50 km range the 3.4° scan travels through the melting layer which is around 4.5 km Above Mean Sea Level (AMSL) at the Irene radar during the summer season. This results in an increase of reflectivity due to the bright-band which is observed. At a longer range the radar beam is above the melting layer where ice is the cause for lower reflectivities, i.e. lower dielectric constant.

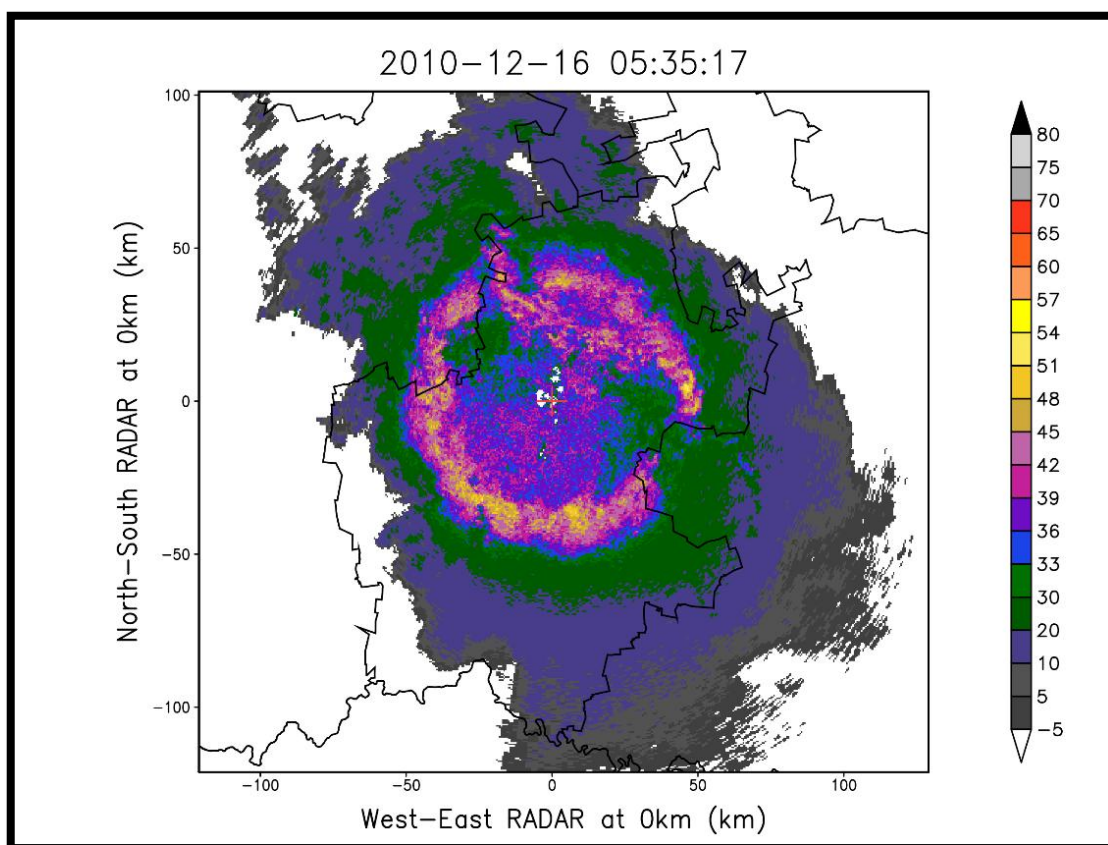


Figure 2-10: The 3.4° PPI illustrating a ring of higher reflectivity as the beam propagates through the melting layer. Clearly illustrating the bright-band

Figure 2-11 illustrates the effect the bright-band can have on precipitation estimates. The precipitation is generated from the maximum reflectivity within a vertical column above each specific grid point. The vertical column extends well above the freezing level. A detailed description of how the precipitation field is generated can be found in Chapter 4 section 4.4.3. A



24 hour accumulation over Irene on the 16<sup>th</sup> of November is shown where the bright-band rings from multiple elevation scans caused a significant over-estimation in precipitation. During stratiform precipitation events the bright-band can cause visible rings of high rainfall as illustrated by Figure 2-11. Although the bright-band is a major source of error in precipitation estimates, it is not the main focus of this study. However, several attempt in identifying and correcting for the bright-band can be found in (Smith, 1986; Cheng and Collier, 1993; Andrieu and Creutin, 1995; Sanchez-Diezma et al., 2000; Gourley and Calvert, 2003; and Zhang and Qi, 2010).

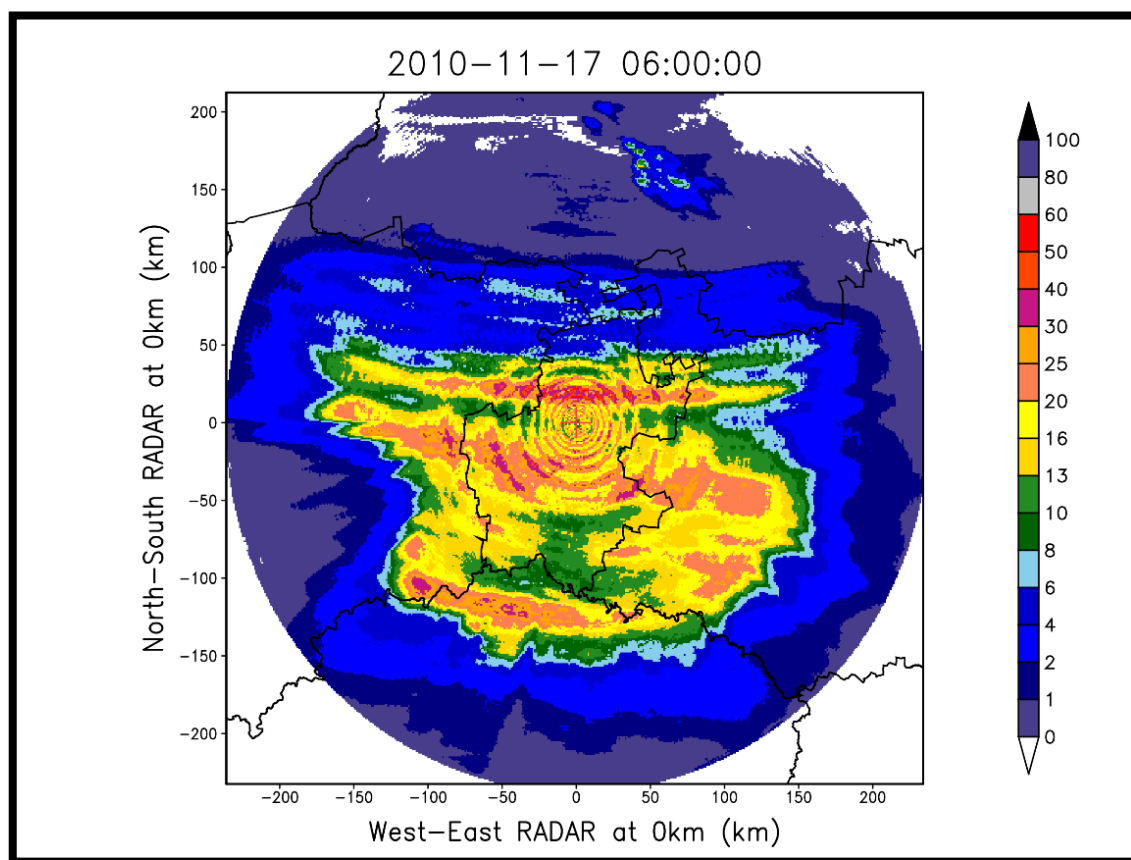


Figure 2-11: A 24 hour precipitation accumulation illustrating rings of over-estimated precipitation caused by bright-band interference.

### 2.4.1.3. Ground Clutter

Ground clutter appears when the main beam (or side lobes) intersects the ground and results in an echo returned to the radar. Targets usually consist of mountains and structures like towers and tall buildings in the immediate area around the radar. The structure would usually be easily recognisable (Doviak and Zrnica, 1993). In Figure 2-12 (a) a PPI display of the 0.5° elevation scan illustrates ground targets during standard refractive conditions. The Johannesburg CBD

with its tall buildings is visible with reflectivity values of over 70dBZ. The Magaliesberg Mountains are also visible as a line of higher reflectivity to the north-west of the radar.

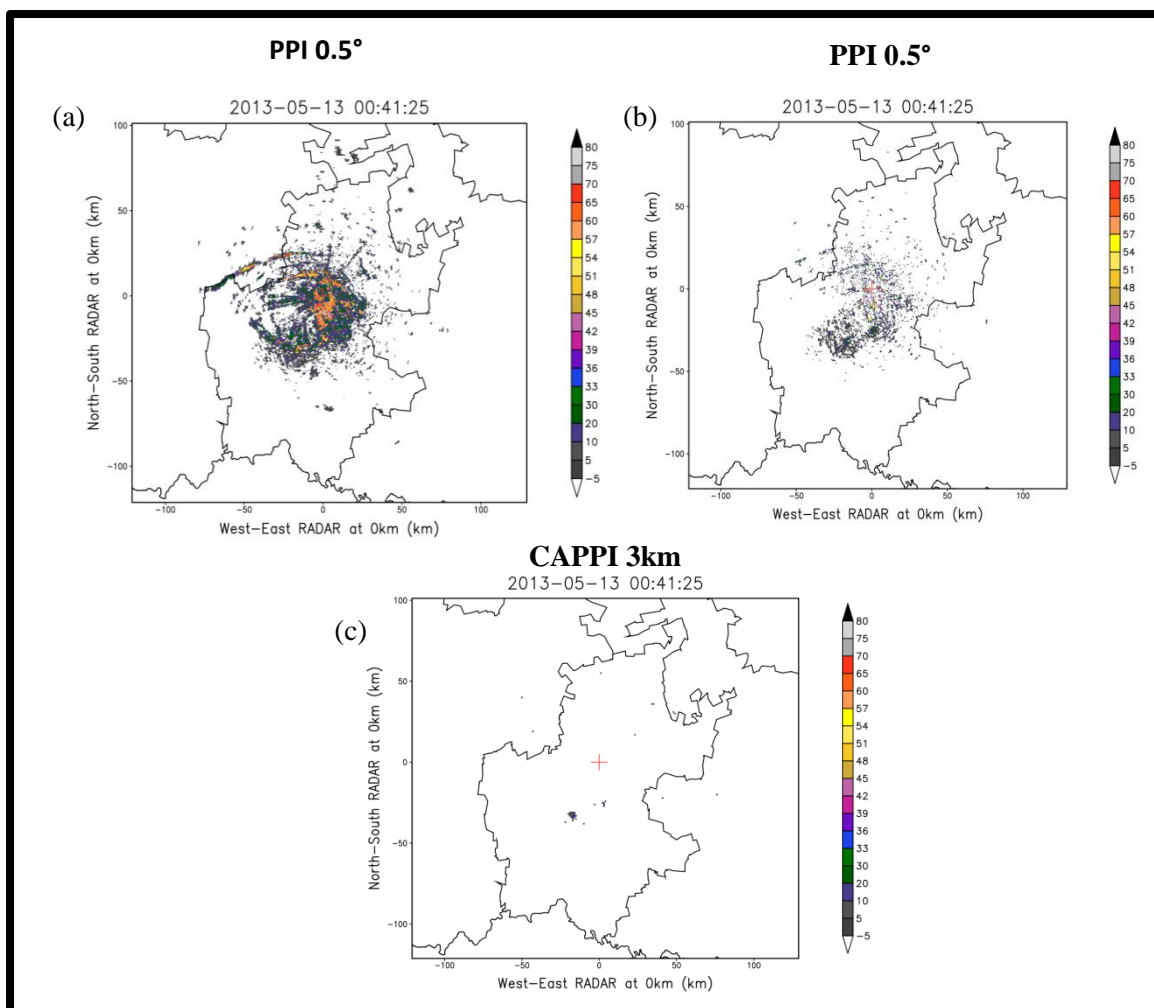


Figure 2-12: The  $0.5^\circ$  PPI display of uncorrected reflectivity data (a) illustrating ground clutter from the Irene S-band radar. After the Doppler filter has been applied (b) most of the clutter has been removed. When extracting the 3km AMSL CAPPI (c) results in virtually no clutter to be present when converting the estimates to precipitation.

Usually a radar clutter map is used to identify and delete ground clutter from a weather radar display, but the Irene radar makes use of a Doppler filter that is available on the Rainbow software suite and will be explained in more detail in chapter 4. Figure 2-12 (b) shows the  $0.5^\circ$  elevation scan after the filter has been applied. Most of the clutter has been removed but some reflectivity still remains over the Johannesburg CBD due to its intensity. However, this remaining clutter will not interfere when converting to CAPPI data for precipitation calculations. Figure 2-12 (c) shows the 3km CAPPI level ( $\sim 1.5$ km above the radar). The effects from ground clutter have been effectively removed.

### 2.4.1.4. Anomalous Propagation

Anomalous Propagation, Anaprop (or AP) is defined as the extended detection of ground targets (Reinhart, 2004). To understand the cause of anomalous propagation one must have a clear understanding of radar beam propagation and the refractive properties of the atmosphere. Reinhart (2004), as well as Doviak and Zrnic (1993) gives detailed descriptions on the theories behind beam propagation and anomalous propagation. It usually occurs in clear weather conditions with the presence of a temperature inversion or whenever the water vapour content of the atmosphere is high. The result is that the radar beam is refracted much more compared to normal atmospheric condition and in extreme cases, can cause the beam to curve towards the surface of the earth.

Figure 2-13 illustrates an example of severe AP that caused ground clutter to be detected at ranges from 100 to 200 km from the Irene radar. The AP results in very large echoes being

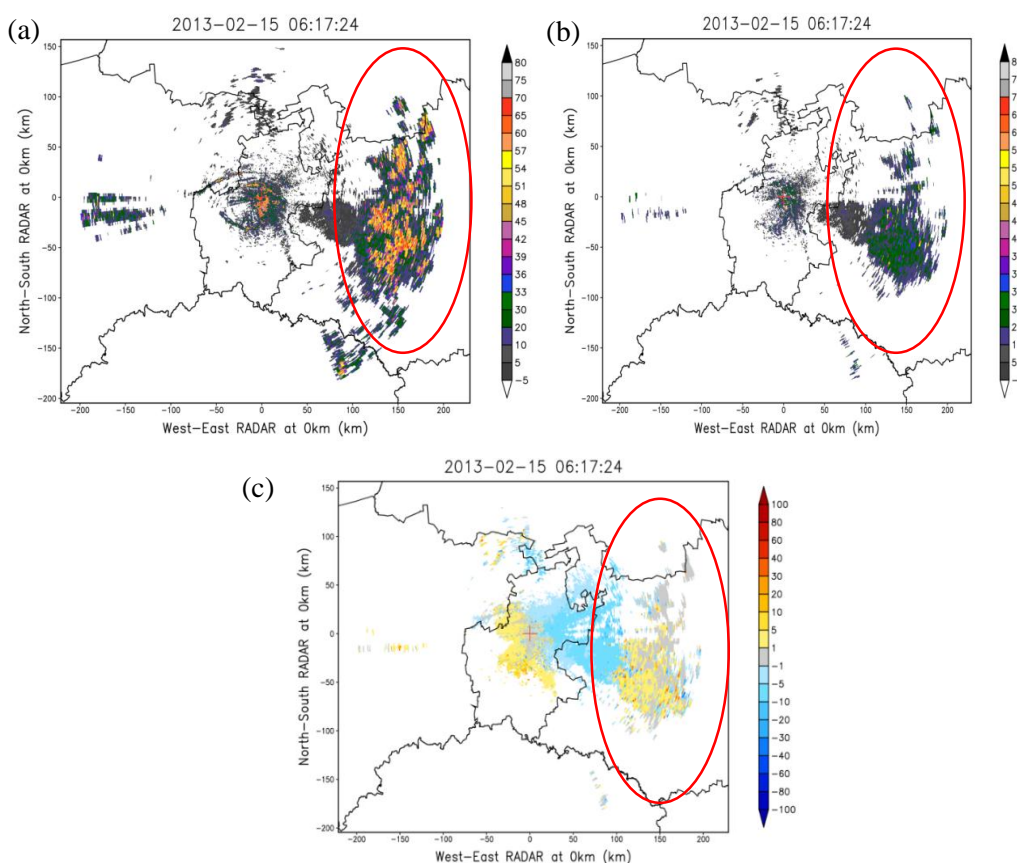


Figure 2-13: Example of Anomalous Propagation showing radar reflectivities in dBZ before (a) and after (b) Doppler filtering. The Velocity field (c) in  $\text{ms}^{-1}$  indicates  $0\text{ms}^{-1}$  over most of the area inside the red oval. The  $0\text{ms}^{-1}$  velocities is a clear indication that the beam is hitting the ground. Thus, the Doppler filter attempts to remove the reflectivities associated with it.

detected due to the radar beam reflecting off the ground to the east of the radar. This is illustrated by the uncorrected reflectivity field displayed but  $0.5^\circ$  PPI in Figure 2-13 (a). The velocity field in Figure 2-13 (c) illustrates the beam path clearly. Around the immediate vicinity of the radar the 0 ms<sup>-1</sup> velocity measurements are clear from the normal ground targets being detected. As the beam propagates and increases in height the velocity measurement increases. But the beam is bend downward through ducting and 0 ms<sup>-1</sup> velocity measurements are again observed due to the beam striking the ground. The Doppler filter makes a very good attempt in filtering the ground clutter, but it does not manage to remove it completely, as seen in Figure 2-13 (b). It is clear that the effects of AP can cause significant problems with precipitation estimates. Developing a filter to effectively remove all occurrences of AP will be beneficial.

#### 2.4.1.5. Scaling

Scaling refers to the technique used to correct range dependent biases in radar reflectivity. These range dependent biases are a result of partial beam filling and of the increase in observation volume with range. This is due to the conical shape of the radar beam. The volume of a measured radar bin is given by,

$$V = \frac{\pi r^2 \theta \phi h}{16 \ln(2)} \quad (2-2)$$

where  $\theta$  and  $\phi$  are the horizontal and vertical beam widths respectively,  $r$  is the distance to the sample volume from the radar, and  $h$  is the pulse length. Thus, from Equation 2-2, the bin volume will increase by the square of the distance to the radar (Reinhart, 2004). This leads to the small intense features within the rainfall estimation field, to be averaged out within the sample volume( $V$ ), thereby resulting in an under-estimation of the frequency of high-intensity echoes at far ranges. Subsequently, a bias in reflectivity measurement is present that will progressively increase with increase in range. The reflectivity measurement is further complicated due to the range resolution of the polar bins being invariant and that the three-dimensional precipitation fields show anisotropic scaling behaviour between the vertical and horizontal directions (Chumchean et al., 2004).

In a hypothesis popularized by Mandelbrot (1982), it can be assumed that these biases in reflectivity measurements can be modelled and corrected for by a simple scaling model. Gupta and Waymire (1990) verified that this scaling hypothesis holds true for the probability distribution of reflectivity measurements with range from the radar. Thus the bias correction can be approached through a transformation function derived using scaling theory as:

$$Z_d = (d/D)^{-\eta} Z_D \quad (2-3)$$

where  $Z_D$  is the measured reflectivity,  $d/D$  is a scale factor, where  $d$  (km) is the reference observation range interval;  $D$  (km) is the observation range of the measured reflectivity  $Z_D$ ;  $\eta$  is the scaling exponent; and  $Z_d$  (dBZ) is the transformed reflectivity of the measured reflectivity ( $Z_D$ ) to be equivalent to reflectivity at the reference observation range interval  $d$  (Chumchean et al., 2004).

#### 2.4.1.6. CAPPI Conversion

Normally radar volume scans are stored in polar coordinates in terms of radar range, elevation and azimuth angle of the scan. The polar coordinates can be interpolated to constant altitude planes, known as Constant Altitude Plan Position Indicators (or CAPPIs). It is an important derived product in the field of hydrometeorology. The advantage of a CAPPI level is that data close to the radar is derived from the higher elevation angles, which will reduce the effect of ground clutter observed by the lowest elevation scan. Even though a clutter filter removes most of the ground clutter some reflectivities still remain due to the clutter. Using reflectivities from higher elevation scans one can eliminate the clutter contaminated data from the lowest elevation scan. The disadvantage with CAPPI data is that it has a limited range at the lower levels. Higher CAPPI levels are needed to include data at further ranges, which in return will decrease the accuracy of the precipitation estimates. Figure 2-14, as illustrated by van Heerden and Steyn (1999), is a diagram that illustrates how CAPPI information is extracted from a polar coordinate system. The process is affected by the propagation of the radar beam. A description of the radar beam path with respect to the curvature of the earth and taking refraction of the beam into account, can be found in Battan (1973).

The interpolation from polar to Cartesian coordinate system simplifies the merging of information from a number of different radars as well as the calculation of precipitation estimates (Terblanche et al., 2001). It is also the required data format for the tracking algorithm in the TITAN software (Wiener and Dixon, 1993). The TITAN program performs an 8-point linear interpolation when converting to CAPPI data, which results in a 1km horizontal resolution with height given at AMSL. The process to generate CAPPI data can be classified into two broad methods, a visual projection- and an interpolation method. The projection method had been very popular in the past due to its simplicity, but discontinuities occur at ranges where the data transitions to different elevations, as illustrated by Figure 2-14. With the interpolation method these discontinuities were more gradual, but it was computationally

expensive to calculate (Mittermaier and Terblanche, 1997). The DISPLACE method was implemented on the MRL-5 radar and used addition and subtraction of the logarithms of reflectivities instead of multiplication and division that is characteristic of conversion algorithms. This resulted in calculations that were around 50% faster (Mittermaier and Terblanche, 1997). However, with the improvements in performance of computers the restrictions on interpolation methods on real-time radar data have been severely reduced.

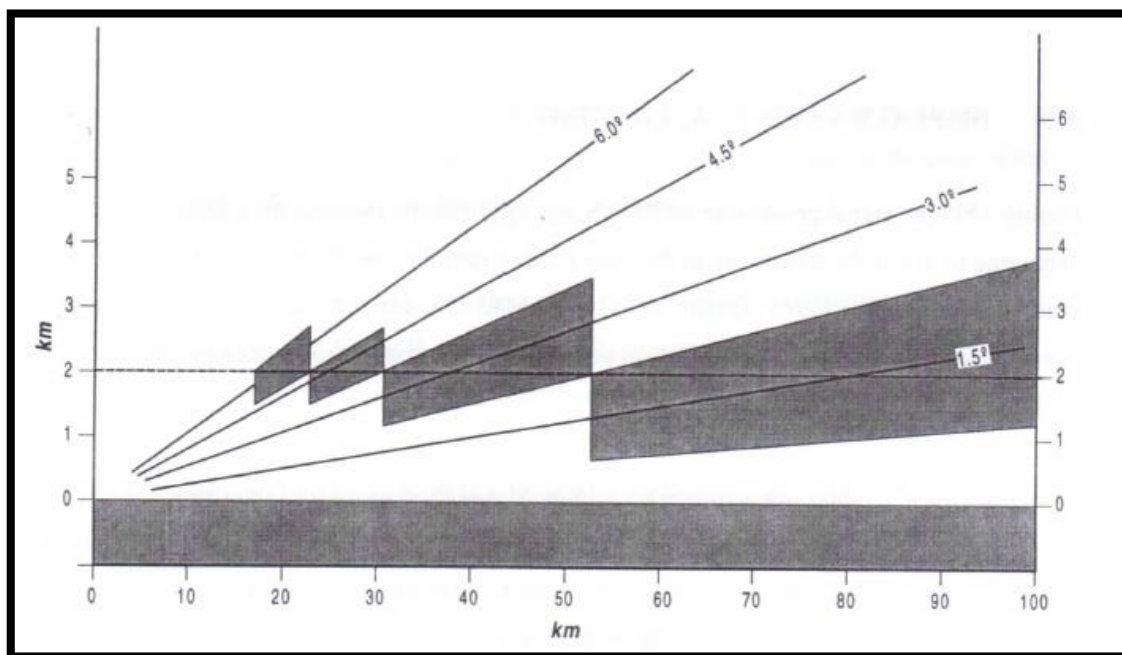


Figure 2- 14: A graphic illustration of how a 2km CAPPI will be interpolated from volumetric data sampling (van Heerden and Steyn, 1999).

## 2.4.2. Converting Reflectivity to Rainfall Rate

Once the reflectivity measurements have been corrected as far as possible and the CAPPI reflectivity extracted the second phase, as shown by Figure 2-2, can start. This involves converting the reflectivity to rain rate and the next section will give more details.

### 2.4.2.1. Radar-Rainfall Algorithms

Due to the fact that precipitation algorithms are the key focus of this study it is necessary to take a closer look at different methods of estimating rainfall from radar reflectivities.

#### *i. The Z-R Relationship*

The advantage of the 10cm S-band radar allows for the assumption that all power received from rainfall is within the Raleigh approximation (Battan, 1973). Thus the power received from a sphere can be expressed as,

$$\bar{P}_r = \frac{C|K|^2Z}{r^2}, \quad (2-4)$$

Where  $\bar{P}_r$  is the power received from a sphere in the atmosphere,  $C$  is a constant related to the radar parameters,  $|K|^2$  is related to the di-electric constant of water and ice,  $Z$  is the reflectivity calculated from the power received and  $r^2$  is the range from the radar. The reflectivity  $Z$  relates to the drop size distribution (DSD) and can be expressed as,

$$Z = \sum N_D D^6, \quad (2-5)$$

where  $Z$  is related to the number of drops ( $N_D$ ) and  $D$  to the drop size to the sixth power. Rain rate is also dependent on the DSD with the drop diameter (to the third power), as well as the terminal velocity of the raindrops. Terminal velocity is directly proportional to the diameter of the drops. Thus reflectivity and rain rate can be related through the empirical expression of the form

$$Z = AR^b, \quad (2-6)$$

where  $A$  and  $b$  are some constant value. In order to estimate rain from the calculated reflectivity it is necessary to understand the relation between reflectivity ( $Z$ ) and rainfall rate ( $R$ ).

Marshall and Palmer (1948) were some of the first to investigate the relation between reflectivity and rain rate. The approach was along statistical lines due to the large variations in time and space between reflectivity and rain rate for a number of different precipitation types. Marshall and Palmer (1948), plotted raindrop diameters against the distribution of the number of drops and for most of the data the general relation of

$$N_D = N_0 e^{-\Lambda D} \quad (2-7)$$

can be fitted, where  $D$  is the drop diameter,  $N_0$  is equal to  $0.08 \text{ cm}^{-4}$  and  $\Lambda$  can be expressed as  $4.1R^{-0.21}$  (specific to rainfall).  $R$  is then the rain rate in (mm/h). Using this relation and any specific rainfall rate, the drop size distribution (DSD) can be estimated. The estimated DSD, can then be used to determine a rain rate associated radar reflectivity through Equation 2-5.

Measuring  $Z$  alone is not enough to determine a unique measurement of  $R$ . The DSD needs to be known and it depends on an indefinite number of parameters. By adjusting the values of  $A$  and  $b$  in Equation 2-6, differences in DSD's under different climatic conditions and geographical locations can be accounted for. Battan (1973) lists over 60 different Z-R relations that show considerable differences for similar types of precipitation. Not only will the DSD influence the Z-R relations over different seasons, climatologies and geographical locations, but Wilson (1966) also found that Z-R relations will differ considerably from one storm to the next within the same radar domain. Even if the DSD were on average the same at two different locations, errors in radar calibration could lead to the development of different Z-R relations (Doviak and Zrnich, 1993). Zero vertical velocity is also assumed by a Z-R relation and significant over- and under-estimation of precipitation can occur in down- and up-drafts respectively. Despite the errors that can occur even with the use of a suitable Z-R relation, less than satisfactory results may be obtained. It is possible to include additional adjustment to the estimated rainfall to improve results from Z-R conversion (Wilson and Brandes, 1979).

*ii. The Area-Time Integral*

The Area-Time Integral (ATI) does not require the use of any Z-R relationship. However, a well-calibrated radar is vital to minimise errors within the estimates (Doneaud et al., 1984). The theory behind ATI is that rainfall accumulated over large areas and time is independent of how rain intensity is distributed within the storm. The volumetric rainfall  $V$  over an area  $A$  during the time  $T$  is given by:

$$V = \int_T \int_A R \, dadt \quad (2-8)$$

where  $R$  is the rainfall area. Assuming that rainfall is constant Equation 2-8 can be expressed as

$$V = R_c \int_T \int_A dadt = R_c ATI \quad \text{where } ATI = \int_T \int_A dadt \approx \sum_i A_i \Delta t_i \quad (2-9)$$

Here,  $A_i$  is the area over which rain was detected during the  $i^{\text{th}}$  observing period and  $\Delta t_i$  is the time interval between observations.  $R_c$  was taken as a constant to illustrate the area-time integral concept. However, in the process of data analysis, values of  $ATI$  can be calculated from Equation 2-9 without making any assumptions about the value of  $R$ . The concept of  $ATI$  is useful because it incorporates information about the areal extent and duration of the precipitation events. It will be most useful for global satellite rainfall (Doviak and Zrnich, 1993).



### *iii. Polarimetric Methods*

Polarimetric methods capitalize on the fact that rain drops are not perfect spheres but are oblate spheroids (Doviak and Zrníc, 1993). Polarimetric rainfall estimation techniques are more robust than the typical Z-R relations with respect to DSD variations and the presence of hail. This is due to the radar transmitting and/or receiving electromagnetic waves in horizontal and vertical polarizations; making it possible to determine specific characteristics of hydrometeors such as their size, shape, spatial orientation and thermodynamic phase (Doviak and Zrníc, 1993).

A number of quantities can be derived from polarization measurements but one of the most significant with regard to precipitation is the measurement of specific differential phase ( $K_{DP}$ ).  $K_{DP}$  is only sensitive to liquid water eliminating the error that small hail can produce with standard Z-R relations.  $K_{DP}$  is also immune to miss-calibrations of the radar, attenuation, and partial beam blockage.  $K_{DP}$  measurement provide benefits to the quality of precipitation estimation through utilising methods to correct radar reflectivity biases that result from the factors mentioned above or through the direct estimation of precipitation using  $R(K_{DP})$  relations (Zrníc and Ryzhkov 1996).

### *iv. Statistical Methods*

Due to high differences within measured and true reflectivity there is high variability within the fitted Z-R relationship. Thus, Rosenfeld et al. (1993) proposed a probability matching method (PMM) that transforms reflectivity measurements to rain rate by matching the probability distributions between them. The method was later improved by considered the change of reflectivity probability density functions (PDF) with range. This method was termed window probability matching method (WPMM), whereby pairs of spatial and contemporary windows small enough to maintain some physical relevance are used in comparing the two PDFs (Rosenfeld et al. 1994). The advantage of the WPMM is the variability normally associated with range and DSD is related to the selected Z-R relationship. However, this method is severely affected by the number of gauges available within the window to estimate PDFs. Calheiros and Zawazki (1987) also made use of probability densities between reflectivity Z and rain rate R to determine an appropriate Z-R relationship. The advantages of this method is that is can be applied to existing data even if the rain gauge data is not simultaneous with the radar data and there is no need for an extensive rain gauge network. However, this method still does not address the variability in DSD from storm to storm within the radar domain.

### 2.4.2.2. Classification

When Z-R relationships (Equation 2-7) are utilised for radar precipitation calculation, errors that are associated with the DSD occur. The variables  $A$  and  $b$  within Equation 2-7 are model parameters, which relate to a specific DSD. These model parameters assume the raindrops are falling at terminal velocity through still air and that the terminal velocity is a function of their diameter. Lee & Zawadzki (2005) illustrated the uncertainty in rainfall estimates due to day-to-day variation in DSD. Battan (1973) also mentions that appreciable differences can sometimes occur from one storm to the next within the same radar domain. Numerous Z-R relationships are listed that have been developed due to these variations to relate the quantities of  $A$  and  $b$  to parameters such as rainfall type, thermodynamic stability, and synoptic classification. Doviak and Zrnich (1993) and Zawadzki (2006) state that it is broadly believed that using distinct Z-R relationships for different rainfall types will lead to an improvement in radar rainfall. However, Zawadzki (2006) shows examples of Z-R relationships that were indistinguishable for stratiform and convective rainfall even though there was considerable variability in the DSD (Chumchean et al., 2008).

It has been suggested that the variation of DSD can be reduced by distinguishing and classifying different rainfall types namely convective and stratiform rainfall. Stratiform precipitation occurs when there is a uniform region of air moving upward. This vertical upward motion of air needs to be small compared to the fall velocity of the ice crystals present within the cloud. This will allow ice crystals to fall towards the earth and through the melting layer. The ice crystal will melt below the freezing layer and result in precipitation on the surface (Houze, 1997). Stratiform precipitation usually occurs within large scale synoptic or topographical forcing that result in an uplift of air. It is also observed within convective cloud systems falling to the ground away from the main convective core. Stratiform precipitation is normally associated with light to moderate precipitation rates, weak horizontal reflectivity gradients (no defined core visible), and is accompanied by frequent observation of the bright-band near the melting layer (Battan, 1973; Houze, 1993). The processes involved with convective precipitation contrast distinctly from stratiform precipitation processes (Houze, 1993). The vertical upward motion of air with convective precipitation is equal to or much higher than the fall velocity of the precipitation particle due to the strong vertical winds. This strong vertical uplift is a localised feature and is usually driven by thermodynamic forcing. A well-defined core of high reflectivities is normally observed by the radar. The bright-band is normally not observed due to the mixing of ice and water within the convective cloud (Chumchean et al., 2008).

Early technique to classify radar precipitation was the background-exceedance technique (BET), which is a simple threshold method, it used rain gauge data to try to identify areas of convective rainfall (Austin and Houze, 1972; Houze, 1973). Churchill and Houze (1984) used this method but modified it to be applied to radar reflectivities. A fixed radius of influence was defined for each identified convective core. Tao et al. (1993) expanded the method by adding two additional criteria, namely the inclusion the updraft velocity and the cloud water content. Steiner et al. (1995) proposed to utilise a two-dimensional classification technique using only radar reflectivity. He also allowed for the length of the convective radius of influence to vary. A number of convective–stratiform classification techniques were introduced. These utilised the microphysics and horizontal gradient of the convective and stratiform cloud structure, as well as the use of Vertical Integrate Liquid (VIL) content and bright-band signature in the Vertical Profile of Reflectivity (VPR) to confirm stratiform or convective precipitation (Yuter and Houze, 1997; Sanchez-Diezma et al., 2000; Sempere-Torres et al., 2000; Tokay and Short, 1996; Zhang and Qi, 2010). Chumchean et al. (2008) introduced a minor modification into the classification method by Steiner et al. (1995), which they incorporated into a real-time operational radar rainfall algorithm.

In terms of radar precipitation estimates the objective of a classification scheme is to limit the variability in DSD and therefore the Z-R relationship from the climatological mean by grouping precipitation with respect to their physical structures. Yuter and Houze (1997) suggest that separating convective and stratiform precipitation based on DSD will likely be inaccurate and is not fully justified. However, Atlas et al. (1999) illustrate that within each classification the DSD are remarkably consistent. They concluded that classification of rainfall types is possible based on DSD and rain rate.

#### **2.4.2.3. Optical Flow Constraint**

In order to determine the movement of precipitation it is necessary to determine the speed and direction of travel. This is of particular interest when forecasting precipitation and a number of advection techniques have been developed and tested over the years. These advection techniques make use of extrapolation methods that can be summarised, very generally, as correlation techniques, centroid tracking and Numerical Weather Prediction (NWP) wind advection (Bowler et al., 2004). Older schemes defined areas of precipitation known as contiguous rain area's (CRA's). The problem with CRA's is that the associated velocities are often generalized. Intense precipitation embedded within the CRA, such as convective showers within stratiform rain areas, often exhibit a noticeable different velocity to that of the larger rain area.

Rinehart and Garvey (1978) introduce a new approach with the Tracking Radar Echoes by Correlation (TREC) method. They made use of a series of blocks to divide the CRA into different sections. Two consecutive time scans separated by a short interval were cross-correlated to find the appropriate correlation for each block. This allowed for multiple advection vectors to be calculated within the CRA. However, the vectors often diverge due to inconsistencies from ground clutter or beam blocking. The continuity of TREC vectors (COTREC) was then developed to try to address this issue (Li et al. 1995). The COTREC method minimises the divergence of the vectors. In reality, this minimises the difference between the vector velocity and the average velocity of neighbouring blocks. This is known as a smoothness constraint and forces the flow of vectors to be smooth (Reyniers, 2008). Bowler et al. (2004), used the optical flow method to try and improve on velocity vector calculations. Optical flow is based on Lagrangian persistence and allows for the direct calculation of motion vectors.

The optical flow method was developed to determine the motion of objects in a series of images (Horn and Schunck, 1981). It originated from the field of robotics as a tool for detecting motion in computer vision. They can provide information on the spatial orientation of objects and rate at which they change between successive images. Central to the study of optical flow is the Optical Flow Constraint (OFC) equation,

$$D_t Z = u \frac{\delta Z}{\delta x} + v \frac{\delta Z}{\delta y} + \frac{\delta Z}{\delta t} = 0 \quad (2-10)$$

where  $u$  and  $v$  are the velocity vectors and  $Z$  is the radar reflectivity (dBZ) at a given point ( $x$ ,  $y$ ). Equation 2-10 is modified slightly from the original equation given by Horn and Schunck (1981) to accommodate reflectivity data and it makes the explicit assumption that the intensity of the reflectivity would only change shape and not in size or intensity. This is not an appropriate assumption to make as the growth and decay of precipitation patterns can result in noisy data. Since  $Z$  is known at every point, solving the partial derivatives can produce a value for  $u$  and  $v$  at every point. However, Equation 2-10 still has insufficient information to determine the  $u$  and  $v$  vectors at every point. Thus, a number of techniques have been developed to supply extra information (Bab-Hadiashar and Suter, 1998). One technique involves aggregating a box of pixels, similar to that of the TREC algorithm. This will produce a set of over-determined linear equations that can be solve to determine  $u$  and  $v$ . Methods such as a least squares approximation to multiple robust techniques can be utilised to solve the system of linear equations; which is more appropriate in the presence of noise. A smoothness constraint still

needs to be applied after the calculations. More details on this technique will be given in chapter 3

### 2.4.3. BIAS Corrections

As far back as the 1950's Hitschfeld and Bordan (1954) suggested that a radar needs to be calibrated against rain gauge measurements. The leading cause of errors within radar measurements of precipitation result from variations in the Z-R relationship due to the microphysical and dynamical processes that effect the DSD and drop fall speed (Wilson and Brandes, 1979). To correct for these errors an adjustment factor, based on the mean multiplicative bias of the radar field, can be uniformly applied to the estimates. The adjustment factor can be calculated with one of the following equations:

$$F = \sum_{i=1}^N G_i / \sum_{i=1}^N R_i \quad (2-11)$$

Or

$$F = \frac{1}{N} \sum_{i=1}^N \frac{G_i}{R_i} \quad (2-12)$$

In Equation 2-11 the observations receive a weight that is proportional to the rainfall depth, while in Equation 2-12 all observations have equal weight (Wilson and Brandes, 1979). Spatial adjustments are necessary due to the fact that smaller errors from gauges near the radar are observed than from the ensemble of all available gauges within the radar domain. Thus, the adjustments can be weighted according to the distance. Although bias adjustments can significantly improve on radar precipitation estimates restraint needs to be exercised when rainfall is extremely light or when radar precipitation variability (i.e. convective storms) in the vicinity of the rain gauge is large (Wilson, 1975; Collier, 1986).

More sophisticated methods to combine radar observations with adjusted gauge measurements have been devised from as early as the 1970's (e.g. Brandes, 1975). These focus primarily on correcting the bias within radar estimates using an adjustment factor. One of the biggest challenges when implementing merging techniques is the difficulty of estimating the error structure associated with rain gauge and radar observations. Sinclair & Pegram (2005) worked around this problem by introducing a conditional merging technique. This technique utilises the spatial information from radar estimates to condition the spatially limited information obtained from interpolating between rain gauges. A precipitation estimate is produced that includes the correct spatial structure. This method results in the spatial detail of the final merged precipitation field to be improved while still maintaining the mean field

characteristics measured by the gauges (Sinclair & Pegram, 2005). In essence the technique eliminates the bias between radar and gauge estimates.

## **2.5. Summary**

It is clear that South Africa has an extensive and rich history when it comes to research with weather radars. The recent addition of 10 Gematronik 600S S-band radar systems has opened the door for future research and development on weather radars in South Africa. The three main component in generating real-time precipitation estimates from radar were reviewed. The first is the correction of reflectivity measurements that include bright band, beam blocking, anomalous propagation and ground clutter were all discussed and illustrated. The second is to introduce techniques to minimize the errors from Z-R conversions. These techniques involve the Z-R conversion relation, classification and OFC vector calculation to minimize the effects of drop size variations with different precipitation types. The third step was a bias correction using rain gauge adjustments. The next chapter will focus on the second part of radar precipitation estimation to include techniques like classification and OFC vector to minimize the errors from Z-R conversion.

---

## CHAPTER 3

# AN ENHANCED QPE ALGORITHM FOR THE IRENE RADAR

---

### 3.1 Introduction

The problem of errors associated with Z-R conversions is the focus of the study and the techniques incorporated in the precipitation estimation algorithm will attempt to minimize these errors. This chapter discusses the algorithm written in FORTAN 90 in more detail. The computer algorithm consists of four main parts:

1. The Classification scheme.
2. Calculation of the motion vectors.
3. Reflectivity to Rainfall conversion.
4. Accumulation through the morphing with motion vectors.

The first part, the classification routine, will assign the radar reflectivity values with the appropriate stratiform or convective rainfall flag. The second part will use the Optical Flow Constraint (OFC) equation to calculate the motion vectors. The third part uses the results from the classification scheme to convert the reflectivity to rain rate with the appropriate Z-R relationship. This will hopefully minimize the errors due to different microphysical properties between stratiform and convective precipitation. The final phase is to morph (definition: to transform an image by computer) the motion vectors with the precipitation field and utilise the time difference between successive scans to yield the final accumulated precipitation field. Adding these techniques to the QPE calculation will hopefully yield favourable results.

### 3.2 The Enhanced QPE Algorithm

The enhanced QPE algorithm consists of four main parts. The process flow of the algorithm is illustrated in Figure 3-1. The process was adapted for the Irene radar and is based on the Australian BoM methodology (Chumchean et al., 2006). The algorithm uses CAPPI reflectivity data that is extracted from the radar volume scan and ingested into the program. Details of this pre-processing algorithm will be made clear in chapter 4. CAPPI data from consecutive volume

scans are included in the calculations. In an operational environment this entails the latest volume scan available in real-time at time  $t_2$  (Figure 3-1) and the previous scan at time  $t_1$ . When the CAPPI data are extracted, no distinction between no-data values and low-reflectivity values are made. Thus, values below -30dBZ needed to be ignored so that they will not become a hindrance in the averaging calculations later in the program. The CAPPI data are then processed within the algorithm to estimate precipitation values from the reflectivity data.

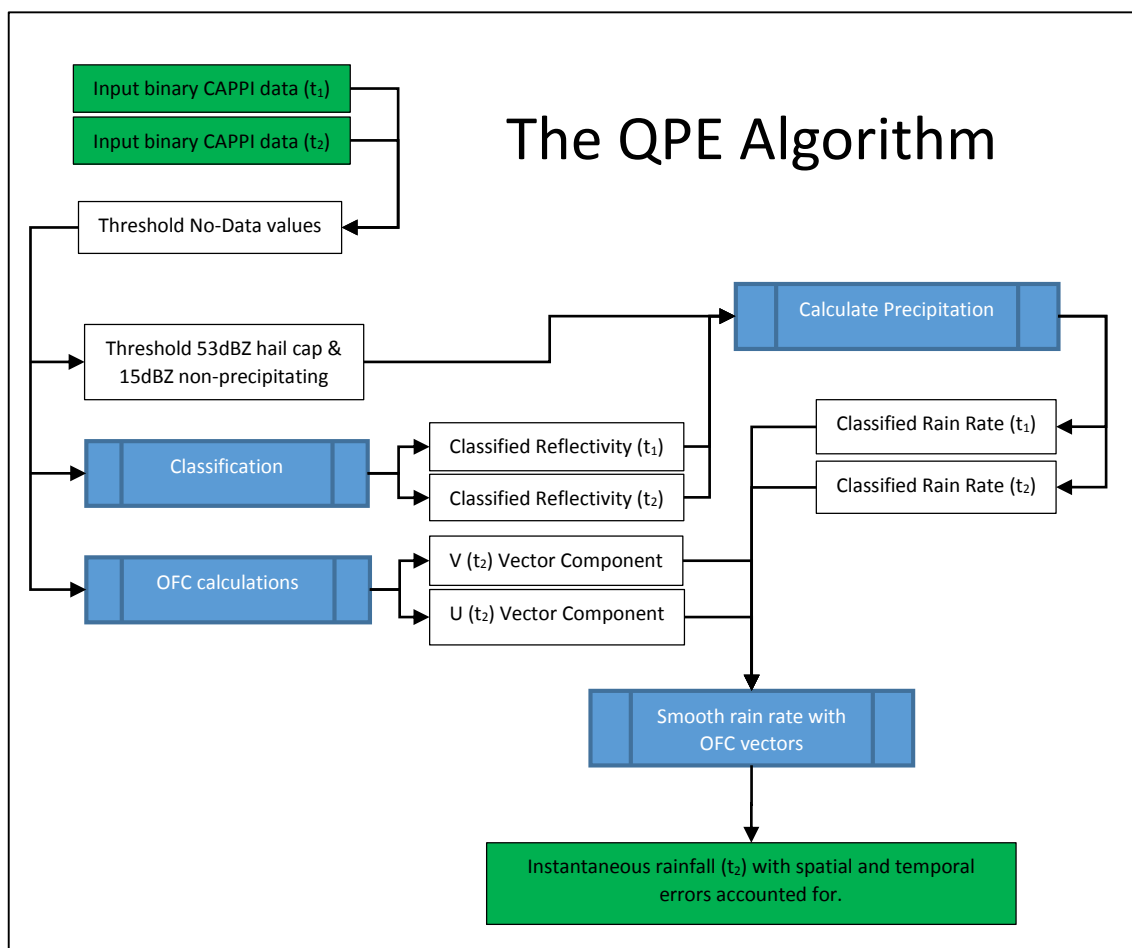


Figure 3-1: The Flowchart indicating the processes involved in calculating the enhanced QPE.

In the first phase of the QPE algorithm the CAPPI reflectivity data is introduced to the classification scheme which was adopted from Chumchean et al. (2008). It is an operational approach to classify radar reflectivity as either convective or stratiform precipitation by using a two dimensional reflectivity field such as CAPPI data. The classification is done on the reflectivity with the intention of assigning the appropriate Z-R relationship to the classified reflectivity value. The output resulting from the classification routine are two fields where the reflectivities at time  $t_1$  and  $t_2$  have been flagged as either no-precipitation, stratiform



precipitation or convective precipitation. The two sequent classified fields will then be later used in the 3<sup>rd</sup> phase of the program for the precipitation calculations.

The second phase of the program is the calculation of the OFC velocity vector  $\mathbf{x} = (u, v)$ , where  $u$  and  $v$  are the velocity vectors in the East-West and North-South direction respectively. By using a series of images the motion of specific object can be determined by solving the OFC equation (Equation 2-10, chapter 2). However, the equation contains insufficient information to determine the velocity at each pixel. A number of techniques can be implemented to provide extra information to establish a best fit (Bab-Hadiashar and Suter, 1998). Thus, consecutive scan times are needed to calculate each pixel's propagation or motion at each point on the gridded field. The CAPPI data at times  $t_1$  and  $t_2$  provides this information and the OFC routine can thus produce a velocity field, with  $u$  and  $v$  components for each pixel at time  $t_2$ . These velocity components will later be morphed with the precipitation field.

The third phase of the QPE algorithm is the actual precipitation calculation. Here the classified values are used to determine which Z-R relationship to apply to the reflectivity data. First, hail and non-precipitation thresholds need to be applied. Any reflectivity below the 15 dBZ threshold, which corresponds to around 0.3 mm/h was considered to be non-precipitating reflectivity values. A default value of 53 dBZ was used for the lower hail threshold. While it is difficult to determine a specific hail threshold, this threshold is also the default setting for radar rainfall estimations in the United States (Fulton et al., 1998). The 53 dBZ threshold yields a rain rate of 75 mm/h using the standard Marshall-Palmer relationship. Thus in this scheme, all reflectivities equal to and greater than the set threshold would have a rain rate of no greater the 75mm/h. The reflectivity data is converted to rain rate using the appropriate Z-R relationship corresponding to the convective or stratiform classified flag value.

The fourth and final phase of the QPE algorithm morphs the OFC vector field with the calculated precipitation values to produce a smoothed accumulated rainfall field that accounts for storm movement, thus minimizing the spatial errors made by the temporal resolution of the radar scan strategy. The reason is that the temporal resolution of a radar volume scan, usually of the order of 5-10 minutes, can cause errors as a pocket of high precipitation rate, such as due to a thunderstorm, shifts position. By integrating the precipitation over the calculated vector path, this error in storm motion can be considerably reduced, if not eliminated.

### 3.3 The Classification Scheme

The classification technique is based on a texture synthesis algorithm. This allows for fast calculations and the use of individual instantaneous reflectivity maps based on 2 dimensional CAPPI data. This is an advantage, as rapid techniques are of great importance within an

operational nowcasting environment. The classification scheme discussed in this section was acquired from Chumchean et al. (2008). It was adopted from work done by Steiner et al. (1995) which builds on earlier work by Churchill and Houze (1984). Figure 3-2 illustrates the classification process by means of a flow diagram. In order for a reflectivity pixel to be classified as a convective centre it must satisfy the following criteria (Chumchean et al., 2008) in equations (3-1) to (3-4):

$$Z \geq 42 \text{ dBZ} \quad (3-1)$$

where  $Z$  is the pixel reflectivity. If it is greater than or equal to 42 dBZ it is immediately classified as a convective centre pixel. If the pixel does not satisfy the criterion in Equation (3-1) then both of the following criteria needs to be evaluated to true,

$$Z_{bg} > Z_c \text{ and } Z - Z_{bg} > \Delta Z \quad (3-2)$$

where  $Z_c$  is the minimum convective centre threshold in dBZ which is selected to be 35 dBZ (Chumcheam et al., 2008) and  $Z_{bg}$  is background reflectivity or background average,

$$\Delta Z = \begin{cases} 10, & Z_{bg} < 0 \\ 10 - \frac{Z_{bg}^2}{P}, & 0 \leq Z_{bg} < 42.43 \\ 0, & Z_{bg} \geq 42.43 \end{cases} \quad (3-3)$$

with,

$$P = \max\left(\frac{(Z_c+2.5)^2}{10}, 140\right) \quad (3-4)$$

$Z_{bg}$  is defined as the average reflectivity within an 11km radius of the current pixel (See Figure 3-4). The reflectivity difference ( $\Delta Z$ ) is calculated by Equation 3-3 and is a function of the background average. It can be graphically interpreted through Figure 3-3.  $\Delta Z$  is a modification from the original to account for the minimum convective centre threshold ( $Z_c$ ) and will default back to the original Steiner et al. (1995) algorithm when  $Z_c$  in Equation 3-4 is selected to be equal to 40 dBZ.

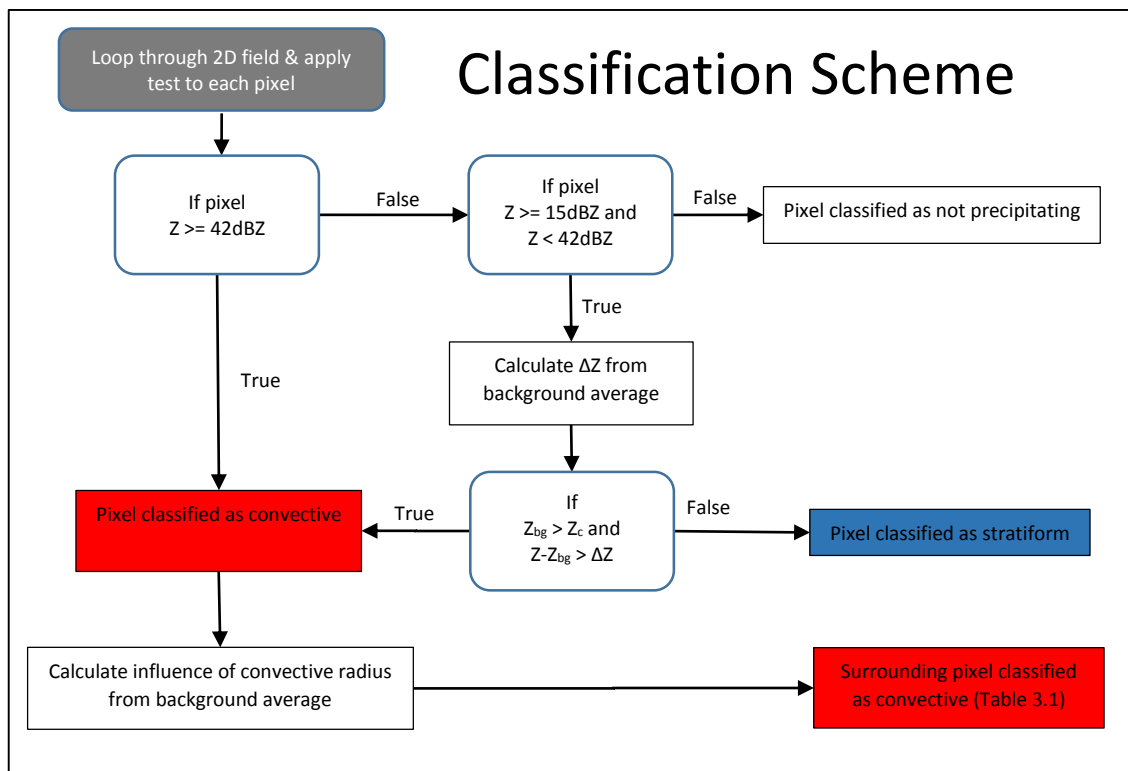


Figure 3-2: A flowchart illustrating the process of classifying a given reflectivity pixel as convective or stratiform precipitation.

From Figure 3-3 it can be determined that when the difference between the pixel value and background average ( $Z - Z_{bg}$ ) is greater than the calculated  $\Delta Z$  for the corresponding background average, the pixel will qualify as a convective centre. However, the background average must also be larger than the selected minimum convective centre threshold. Thus, a pixel value that satisfies the criteria in Equation 3-1 or in Equation 3-2 will be classified as a convective centre. If it does not, the pixel is flagged as stratiform precipitation (See Figure 3-2). Any value below the 15 dBZ threshold is assumed to be non-precipitating and is not classified.

Once a pixel has been flagged as a convective centre the convective radius needs to be determined. The convective radius is a function of the background average. The relationship between the background average and the convective radius is listed in Table 3-1. The larger the value of the background average the greater is the influence of convection of the neighbouring pixels around the convective centre. The pixels that fall within this radius are then also flagged as convective pixels. Figure 3-4 illustrates a convective radius of 5 km (the red circle) around the flagged convective centre (the green pixel). All the pixel centres that fall within this radius are also flagged as convective. The end result is a classified reflectivity field that is flagged as either no-precipitation, stratiform precipitation or convective precipitation pixels.

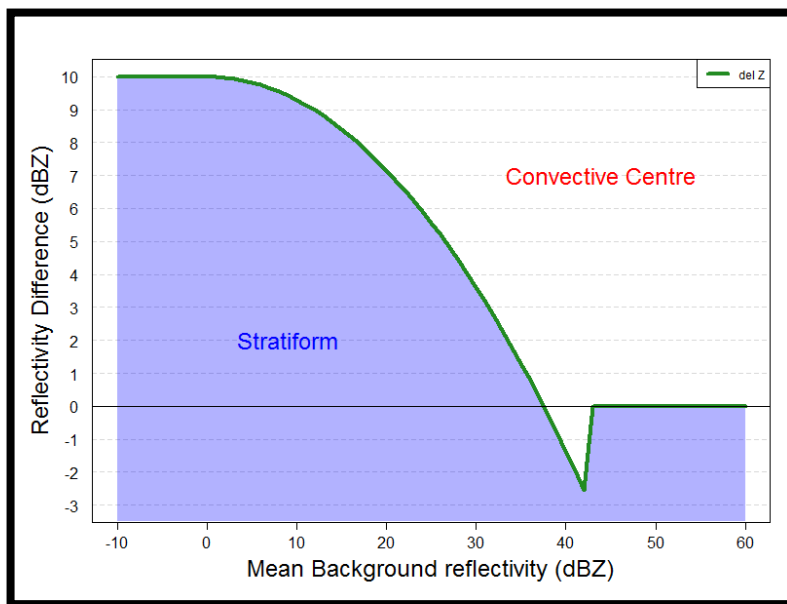


Figure 3-3: The reflectivity difference ( $\Delta Z$ ) compared to Mean Background Average ( $Z_{bg}$ ), with  $Z_c$  selected at 35 dBZ. If the difference ( $Z - Z_{bg}$ ) is above the green line the pixel will be classified as a convective centre, below the line it will be a stratiform classified value.

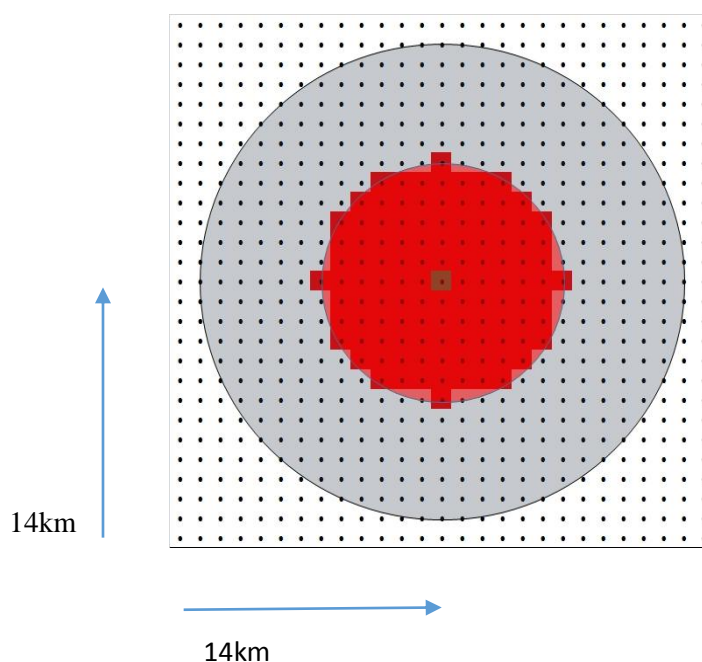


Figure 3-4: A graphical representation of the classified pixel (green), the mean background average (grey) and convective radius (red). Pixels are included for calculations when the pixel centre is within the determined radii.

Table 3-1: The Table lists radius of influence around the convective centre for the appropriate background average (Chumchean et al., 2008).

<b>Relationship between mean background reflectivity and convective radius</b>					
<b>Mean Background Reflectivity - <math>Z_{bg}</math> (dBZ)</b>	<b>15-25</b>	<b>25-30</b>	<b>30-35</b>	<b>35-40</b>	<b>40-50</b>
<b>Convective Radius (km)</b>	<b>1</b>	<b>2</b>	<b>3</b>	<b>4</b>	<b>5</b>

In the original Steiner et al. (1995) scheme each grid point pixel, usually taken from CAPPI reflectivity below the melting layer, needs to be greater than 40dBZ or it needs to exceed the average intensity of reflectivity taken from the surrounding values (selected radius of 11 km), by a specified threshold ( $\Delta Z$ ), to be considered a convective centre. Then for each point that has been identified as convective, a surrounding area similar to the background reflectivity, which also depends on the intensity of the surrounding background reflectivity, is also classified as convective (see Table 3-1).

Steiner et al. (1995) suggested that criteria be modified to best distinguish convection and stratiform precipitation depending on the particular geographic location of radar, precipitation regime and radar attributes such as, receiver sensitivity, beam width, scanning strategies, etc. The Darwin radar in Australia was originally used to classify instantaneous CAPPI reflectivity data form. The radar had a beam width of  $1.65^\circ$  and CAPPI data was interpolated to Cartesian Coordinates with a horizontal resolution of 2 km (Steiner et al., 1995). The convective radius is a function of the grid resolution of the CAPPI data rather than the precipitation regime. Thus, Chumchean et al. (2008) re-calibrated the associated parameters for use at the Kurnell radar in Sydney, Australia. This radar had a beam width of  $0.9^\circ$  and could interpolate the instantaneous CAPPI reflectivity to Cartesian coordinates with a 1 km horizontal resolution (Chumchean et al., 2008). Calibration of the classification parameters were done through visual interpretation of convective and stratiform cells. The spatial resolution of the CAPPI data (1 km-square) allows for the use of 42 dBZ as a threshold instead of the 40 dBZ threshold proposed by Steiner et al. (1995).

It is worth noting that no changes to the associate parameters of the classification scheme have been made for the Irene radar which was adopted 'as is' from the Kurnell radar in Sydney, Australia. It was decided to test the current classification scheme performance and then make appropriate change from the findings at a later stage. The physical attributes of the two radars

are largely similar in terms of beam width and grid resolution. Thus, differences in the performance of the classification scheme are assumed to be small.

Figure 3-5 illustrates a classified field on 28 October 2010 at 02:29:16 UTC and is compared with the instantaneous reflectivity field. The classified convective cells correspond well with the high reflectivity cells observed within the reflectivity field, likewise for the stratiform classified precipitation.

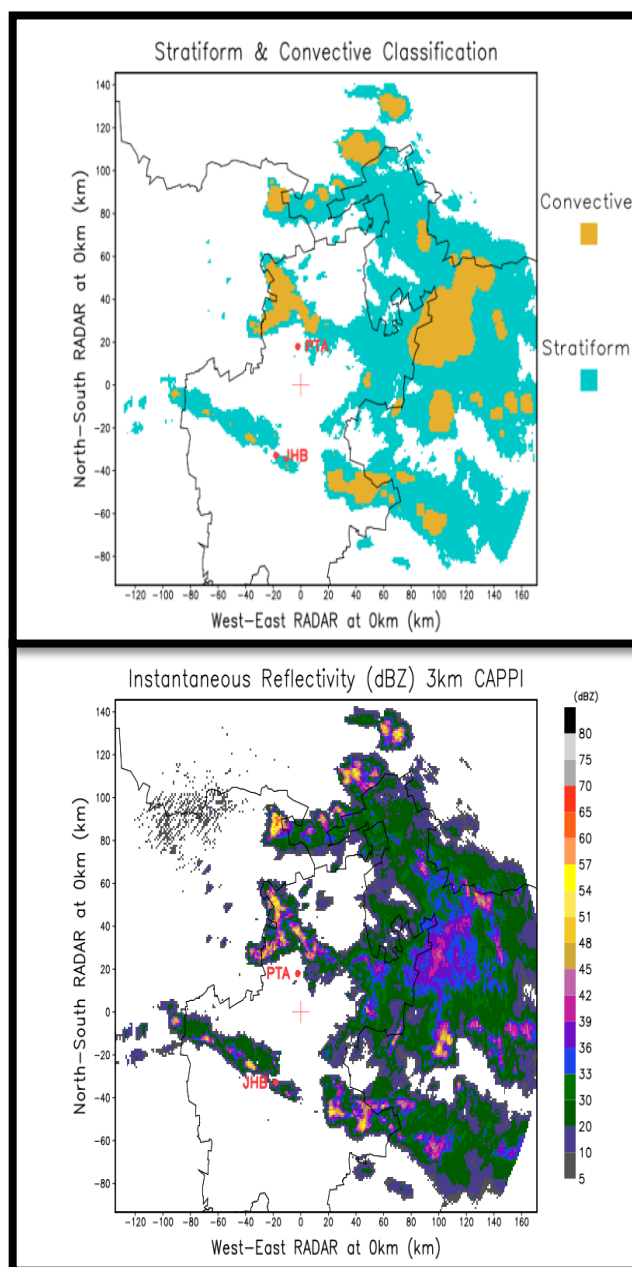


Figure 3-5: The classified field on 28 October 2010 at 02:29:16 UTC (above) and the corresponding instantaneous reflectivity field (below).

This region might be contaminated with bright-band effects, which can influence the classification scheme. The only area of concern is that the stratiform region of high reflectivities

to the east of the radar, is classified as convective. It is well-known that the classification algorithm from Steiner et al. (1995) classifies bright band contaminated areas as convective precipitation. One way to improve on the algorithm is to make use of volumetric data. Convective storms usually show strong vertical development, thus by taking the average reflectivity within a vertical column favourable results could be achieved (Franco et al., 2006). However, as stated above this will only be explored in future work.

### 3.4 Velocity Vector Calculations Using Optical Flow Constraints

After the classification has been done the algorithm moves on to determine the velocity vectors. The process flow of the calculations is illustrated in Figure 3-6. The following section will give a more detailed description of how the optical flow vectors are calculated, following from the discussion in section 2.4.2.3.

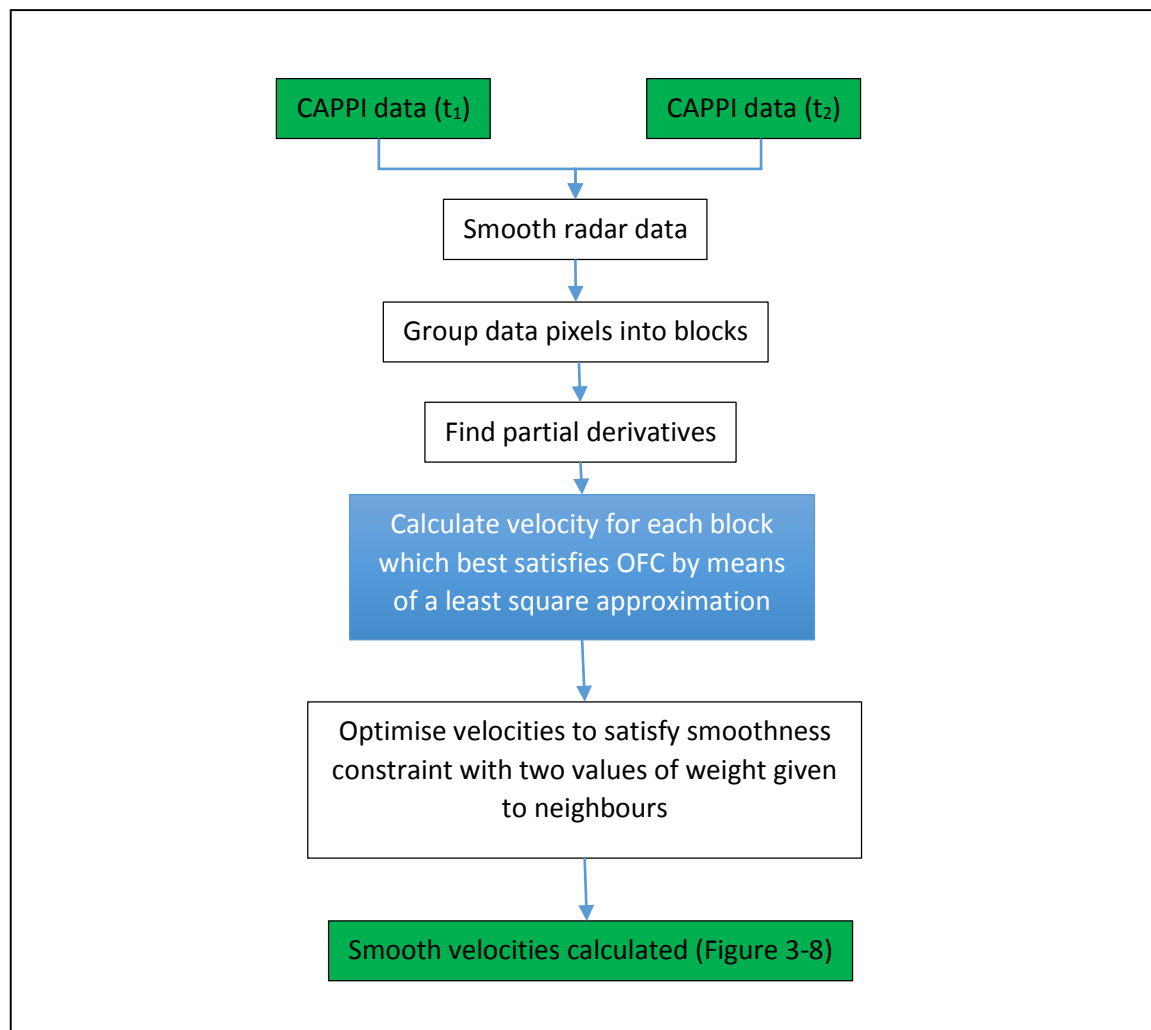


Figure 3-6: Flowchart illustrating the process to calculate motion vectors from two consecutive radar scans using an optical flow method

The radar reflectivity data first has to be smoothed so that the partial derivatives for the OFC equation (Equation 2-10) can be calculated using a finite-difference method. The smoothed reflectivity data are partitioned into blocks, so that a least squares method can be used to solve the OFC for each block. The velocity field is then interpolated back to the original grid resolution and a smoothness constraint is applied so that each pixel is equal to the average of its neighbours.

### 3.4.1 Determine the OFC Partial Derivatives

In order to calculate the partial derivatives with a simple finite-difference method it is necessary to smooth the radar reflectivities to obtain a stable estimate of the local derivatives (Bowler et al., 2004). To smooth the values, a square box is centred over a pixel intended to be averaged. The smoothed reflectivity intensity is thus given by

$$Z_S(x, y, t) = \frac{1}{(2L_S + 1)^2} \sum_{i=x-L_S}^{x+L_S} \sum_{j=y-L_S}^{y+L_S} Z(i, j, t) \quad (3-5)$$

where  $L_S$  is equal to 15. This choice of  $L_S$  means that the smoothing occurs over a box of 31 by 31 pixels. Thus the speed of reflectivities moving at more than 30 pixels per time step cannot be estimated accurately. For example, considering a storm moving at 100 km/h (about the maximum speed observed during the study period) the storm will only shift 10 pixels separated by a 6 minute scan intervals on a 1km grid resolution. This is well within the limit to estimate accurate velocities by solving the derivatives. It might be tempting to choose  $L_S$  to be very large, given that the size influences the upper limit of the velocities that can be accurately estimated. However, this will result in a decrease in spatial resolution of the derivative estimates. Thus, the choice of  $L_S$  is a compromise between estimating large velocities accurately, and capturing the differential motion exhibited by neighbouring pixels (Bowler et al., 2004).

Once the reflectivity field has been smoothed, the partial derivatives from Equation 2-10 can be determined using a centred finite difference method following Horn and Schunck (1981). First the smoothed field is separated into blocks similar to the TREC algorithm discusses in section 2.4.2.3. The derivatives can then be calculated using an image sequence of aggregating blocks with the following equations:

$$\frac{\delta Z(x, y, t)}{\delta x} \approx \frac{1}{16} (Z(x + 1, y + 1, t) + Z(x - 1, y + 1, t))$$



$$\begin{aligned}
& -\frac{1}{16}(Z(x+1, y+1, t-1) + Z(x-1, y+1, t-1)) \\
& +\frac{1}{8}(Z(x+1, y, t) + Z(x-1, y, t)) \\
& -\frac{1}{8}(Z(x+1, y, t-1) + Z(x-1, y, t-1)) \\
& +\frac{1}{16}(Z(x+1, y-1, t) + Z(x-1, y-1, t)) \\
& -\frac{1}{16}(Z(x+1, y-1, t-1) + Z(x-1, y-1, t-1))
\end{aligned} \tag{3-6}$$

$$\begin{aligned}
\frac{\delta Z(x, y, t)}{\delta y} \approx & \frac{1}{16}(Z(x+1, y+1, t) + Z(x+1, y-1, t)) \\
& -\frac{1}{16}(Z(x+1, y+1, t-1) + Z(x+1, y-1, t-1)) \\
& +\frac{1}{8}(Z(x, y+1, t) + Z(x, y-1, t)) \\
& -\frac{1}{8}(Z(x, y+1, t-1) + Z(x, y-1, t-1)) \\
& +\frac{1}{16}(Z(x-1, y+1, t) + Z(x-1, y-1, t)) \\
& -\frac{1}{16}(Z(x-1, y+1, t-1) + Z(x-1, y-1, t-1))
\end{aligned} \tag{3-7}$$

$$\begin{aligned}
\frac{\delta Z(x, y, t)}{\delta t} \approx & \frac{1}{16}(Z(x+1, y-1, t) - Z(x+1, y-1, t-1)) \\
& +\frac{1}{8}(Z(x, y-1, t) - Z(x, y-1, t-1)) \\
& +\frac{1}{16}(Z(x-1, y-1, t) - Z(x-1, y-1, t-1)) \\
& +\frac{1}{8}(Z(x+1, y, t) - Z(x+1, y, t-1)) \\
& +\frac{1}{4}(Z(x, y, t) - Z(x, y, t-1)) \\
& +\frac{1}{8}(Z(x-1, y, t) - Z(x-1, y, t-1))
\end{aligned} \tag{3-8}$$

$$\begin{aligned}
& + \frac{1}{16} (Z(x+1, y+1, t) - Z(x+1, y+1, t-1)) \\
& + \frac{1}{8} (Z(x, y+1, t) - Z(x, y+1, t-1)) \\
& + \frac{1}{16} (Z(x-1, y+1, t) - Z(x-1, y+1, t-1))
\end{aligned}$$

After determining the derivatives in Equation 2-10, there is still insufficient information to determine the  $u$  and  $v$  vector components at every point.

### 3.4.2. Calculating the Velocity of a Block

By solving for the partial derivative within the block, a system of over-determined linear equations is reached and given by,

$$a_{i1}u + a_{i2}v = b_i + e_i, \quad i = 1, 2, \dots, m \quad (3-9)$$

where  $m = 2500$ ,  $a_{i1}$  and  $a_{i2}$  are the spatial derivatives  $\frac{\delta Z}{\delta x}$  and  $\frac{\delta Z}{\delta y}$  respectively and  $b_i$  is the negative temporal derivative  $-\frac{\delta Z}{\delta t}$  for every pixel  $i$  within the defined block, as mentioned in section 2.4.2.3 a method using robust to least squares. In matrix form Equation (3-9) can be written as:

$$\mathbf{Ax} = \mathbf{b} + \mathbf{e} \quad (3-10)$$

where  $\mathbf{x}$  is the two-component vector,  $\mathbf{x} = (u, v)$ ,  $\mathbf{A}$  is a 2 dimensional matrix of dimensions  $m \times 2$ ,  $\mathbf{b}$  has dimensions  $m \times 1$  and the error vector  $\mathbf{e}$  is also  $m \times 1$ . Plotting the set of linear equations known as constraint lines will result in the examples shown in Figure 3-7. When considering noiseless data, i.e. data that only changes its position, but does not change its shape or intensity over time is illustrated by Figure 3-7 (a).

The result of the noiseless data will cause all of the constraint lines to intersect at the appropriate value for  $u$  and  $v$ . This is not the case when working with radar reflectivity data. It is well known that weather echoes can rapidly change in shape and intensity over time and will be the product of very noisy data. The constraint lines will not intersect at one point, but rather at multiple points as show in Figure 3-7 (b). In order to find a single vector that best represents all pixels within the block a method of solving the set of linear equation in the presence of noise is

needed. As mentioned in section 2.4.2.3, a method using robust least squares can be applied. The advantage of a robust approach, instead of a rational approach, is that outliers within the input data will not influence the calculated result significantly (Bab-Hadiashar and Suter, 1998). A simple least squares approximation was selected to solve the vectors for each block. It is not a robust method, which makes the algorithm sensitive to the influences of outliers, particularly around the boundaries of the reflectivity field, such as the edges of precipitating areas and at the limits of the radar range. However, the algorithm is fast to compute, which is a valuable attribute in the Nowcasting field.

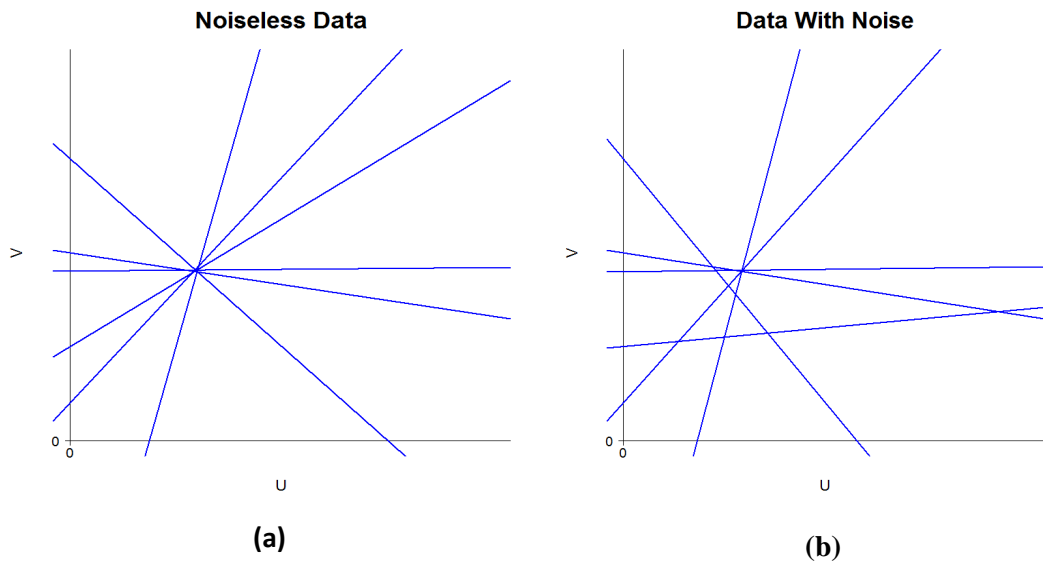


Figure 3-7: Plotting constraint lines with noiseless (a) and noisy (b) data.

With the least squares method, we seek to minimise the sum of squares of the errors  $e$  in Equation 3-9. This is expressed as:

$$U = \sum_{i=1}^m (a_{i1}u + a_{i2}v - b_i)^2 \quad (3-11)$$

which can also be written in matrix form as:

$$\mathbf{A}^T \mathbf{A} \mathbf{x} = \mathbf{A}^T \mathbf{b} \quad (3-12)$$

where the transpose of  $\mathbf{A}$  is multiplied into Equation 3-10. Solving Equation 3-12 will result in matrices, which are minimised and are of dimensions  $2 \times 2$  and  $2 \times 1$  for  $\mathbf{A}$  and  $\mathbf{b}$  respectively. Thus, it is possible to determine  $\mathbf{x} = (u, v)$  by applying the LU decomposition algorithm to the resulting matrices. LU decomposition is useful due to the fact that it can easily be built into a computer algorithm to solve a system of linear equations. Press et al. (1992) gives a thorough explanation on the principals behind LU decomposition and how to implement it successfully in an algorithm. Thus, only a short summary on LU decomposition will be given below and the reader is encourage to refer back to Press et al. (1992) for more details with regards to implementation.

LU decomposition assumes that the matrix  $\mathbf{A}$  can be the product of two matrices as follow:

$$\mathbf{A} = (\mathbf{L} \cdot \mathbf{U}) \quad (3-13)$$

Where  $\mathbf{U}$  is the upper triangular matrix of  $\mathbf{A}$ , and  $\mathbf{L}$  is the Lower triangular matrix of  $\mathbf{A}$ . For example,

$$\begin{bmatrix} a_{11} & a_{12} \\ a_{21} & a_{22} \end{bmatrix} = \begin{bmatrix} l_{11} & 0 \\ l_{21} & l_{22} \end{bmatrix} \cdot \begin{bmatrix} u_{11} & u_{12} \\ 0 & u_{22} \end{bmatrix} \quad (3-14)$$

Equation 3-10 can be decomposed by substituting Equation 3-13 into Equation 3-10,

$$\mathbf{A} \cdot \mathbf{x} = (\mathbf{L} \cdot \mathbf{U}) \cdot \mathbf{x} = \mathbf{L} \cdot (\mathbf{U} \cdot \mathbf{x}) = \mathbf{b} \quad (3-15)$$

The vector  $\mathbf{x} = (u, v)$  can then be solved first by forward substitution of the vector  $\mathbf{y}$  such that,

$$\mathbf{L} \cdot \mathbf{y} = \mathbf{b} \quad (3-16)$$

Then through back substitution such that,

$$\mathbf{U} \cdot \mathbf{x} = \mathbf{y} \quad (3-17)$$

Equations 3-18 and 3-19 below illustrates how the vector  $\mathbf{y}$  is calculated from Equation 3-16,

$$y_1 = \frac{b_1}{l_{11}} \quad (3-18)$$

$$y_2 = \frac{1}{l_{22}} [b_2 - l_{21}y_1] \quad (3-19)$$

and Equations 3-20 and 3-21 illustrates how to solve Equation 3-17 to obtain vector  $x$ ,

$$x_2 = \frac{y_2}{u_{22}} \quad (3-20)$$

$$x_1 = \frac{1}{u_{11}} [y_1 - u_{12}x_2] \quad (3-21)$$

Note that the complexity of the LU decomposition can be avoided by inverting the 2x2 matrix  $\mathbf{A}^T \mathbf{A}$  directly as  $\mathbf{Z}$  to obtain  $\mathbf{x} = [\mathbf{A}^T \mathbf{A}]^{-1} \mathbf{A}^T \mathbf{b}$ , a very simple and speedy calculation. Whichever method is used, the result is that the vector  $\mathbf{x}$  for each block now has mean values for the two components  $u$  and  $v$ , because  $\mathbf{x} = (u, v)$ . The velocity vectors of each block are interpolated back to the original grid size. The next step is to apply a smoothness constraint so that the vector cannot deviate substantially from the average neighbouring velocity vectors.

### 3.4.3 Optimising the Velocity

The last step in calculating the velocity vectors is to find the velocity for each block that best satisfies the smoothness constraint. The method describe below was taken from Bowler et al. (2004). As mentioned in the previous section the least squares method is very sensitive to outliers. Thus, by forcing the velocity to be equal to its neighbouring velocity the outliers in the velocity field can be effectively smoothed. The first step is to assign a weight denoted  $K(x, y, t)$ , to the velocity that is dependent on the smoothed reflectivity value within the defined block surrounding the velocity vector. A block with infinite reflectivity will receive a weight of 1 while block with no total reflectivity will have a weight of 0; the velocity is calculated as follows:

$$K(x, y, t) = 1 - \exp \left( - \sum_{i=x}^{x+L} \sum_{j=y}^{y+L} \sum_{k=t-1}^t \frac{Z_s(i, j, k)}{2wL^2} \right) \quad (3-22)$$

where  $w$  is a parameter greater than 0, and  $L$  is the block size. The parameter  $w$  is usually set to 0.75 because it gives favourable results (Bowler et al., 2004). The weighted velocity is then calculated as

$$V_w(x, y, t) = K(x, y, t)V_{OFC}(x, y, t) \quad (3-23)$$

where  $V_{OFC}$  is the velocity calculated from the OFC equation. The weighted velocity vectors  $V_w$  can then be used to calculate the average velocity of the neighbouring velocity vector  $V_n$  and is given by

$$V_n(x, y, t) = \frac{1}{6} \left( V_w(x+L, y, t) + V_w(x-L, y, t) + V_w(x, y+L, t) + V_w(x, y-L, t) \right) + \frac{1}{12} \left( V_w(x+L, y+L, t) + V_w(x+L, y-L, t) + V_w(x-L, y+L, t) + V_w(x-L, y-L, t) \right) \quad (3-24)$$

The velocity field that will satisfy the smoothness constraint can thus be calculated for every block as

$$V(x, y, t) = ((1 - r_n)K(x, y, t)V_{OFC}(x, y, t) + r_n V_n(x, y, t)) / K_{total}(x, y, t) \quad (3-25)$$

where  $r_n$  is a parameter between 0 and 1.  $K_{total}$  is the average weight of the block and its neighbours. The value of  $r_n$  is chosen to be 0.35 as this appears to give favourable results. The result of the calculation through section 3.4 is illustrated in Figure 3-8. The calculated velocity vector  $V$  replaces  $V_{OFC}$  and thus satisfies the smoothness constraint. The final step is to replace regions of zero velocities with the calculated average velocity of the entire field.

### 3.5 Precipitation Estimates with Dual Z-R Relationships

The next step in the QPE algorithm outlined in Figure 3-1 is to convert the reflectivity measurement into rain rate estimates. Dual Z-R relationships are applied to the different classifications calculated in section 3.3. Poolman et al. (2014) tested a number of Z-R relationships at the Irene and Port-Elizabeth radars and found the relationships in Equation 3-26

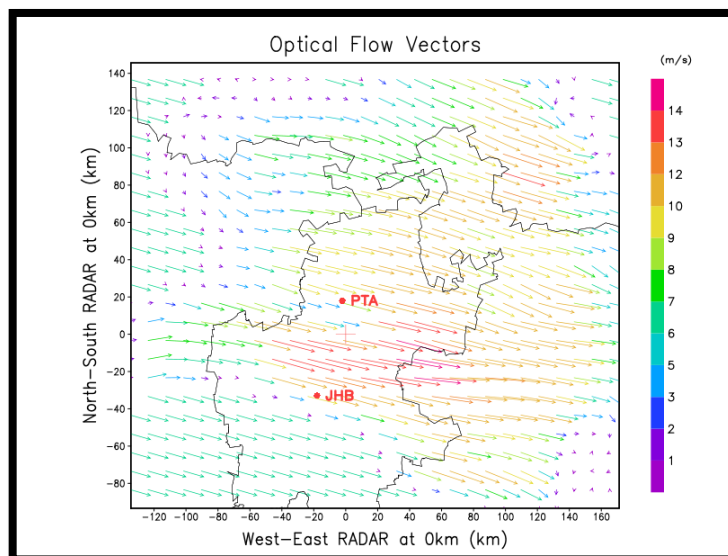


Figure 3-8: Velocity vectors on 28 October 2010 at 02:29:16 UTC, calculated from the OFC equation indicating the direction and speed of the reflectivity field.

and 3-27 outperforms all other Z-R relationship. The use of a dual Z-R relationship gave better results than using a single Marshall-Palmer relationship. Thus, when reflectivities are classified as stratiform precipitation the standard Marshall-Palmer Z-R relationship is applied. From Equation 2-7 the relationship is expressed as

$$Z = 200R^{1.6} \quad (3-26)$$

where the units of  $Z$  are in  $\text{mm}^6\text{m}^{-3}$  and  $R$  is in  $\text{mmh}^{-1}$ . The Marshall-Palmer relationship is one of the most commonly used relationships not only for stratiform precipitation, but for radar derived precipitation in general (Battan, 1973). The relationship was derived by comparing Drop Size Distributions (DSD) and radar reflectivity measurement from numerous precipitation events (Marshall and Palmer, 1948). A different Z-R relationship is applied when reflectivities are classified as convective. The relationship is expressed as

$$Z = 300R^{1.4} \quad (3-27)$$

with units similar to Equation 3-26 and is widely used for convective precipitation (Fulton et al., 1998; Zhang et al., 2011). Figure 3-9 illustrates a 1 hour accumulations calculated from the classification scheme and the Z-R relationships in Equations 3-26 and 3-27. Figure 3-9 also

illustrates the problem of temporal sampling frequency. The long sampling time results in the loss of important evolutionary features of the precipitation field.

### 3.6 Algorithm to Smooth the Spatial Rainfall Field for Accumulations

The accumulation technique shown here (following Hanesen (2002) and improved by Sinclair (2007)) handles the problem of temporal sampling illustrated in Figure 3-9. The accumulation technique that accounts for the spatial and temporal evolution of the rainfall field between successive radar scans can be expressed as:

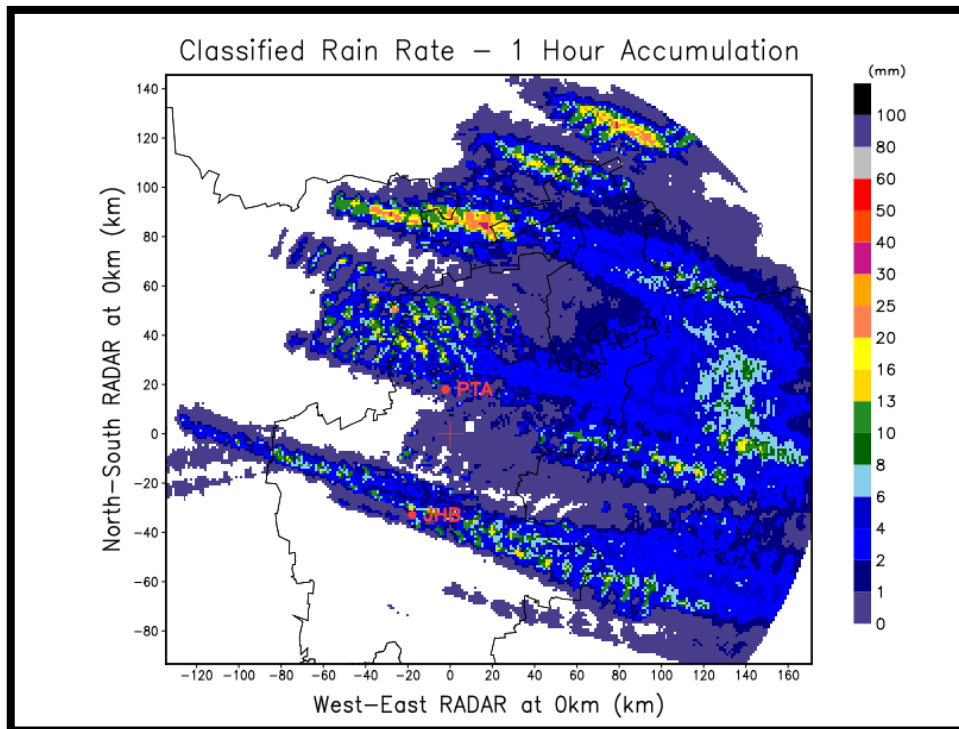


Figure 3-9: A one hour accumulation using dual Z-R relationships on 28 October 2010 at 03:00:00 UTC. Stratiform classified precipitation makes use of Marshall-Palmer ( $Z=200R^{1.6}$ ), while convective classified precipitation is converted with the convective Z-R relationship ( $Z=300R^{1.4}$ ).

$$A_P = \int_{t_1}^{t_2} R(P_t) dt \quad (3-28)$$

where  $P_t = (x, y, t)$  is any point at time  $t$  and  $t_1 \leq t \leq t_2$ . The problem is that  $R(P_t)$  is not known. However, the rain rate  $R(P_{t_1})$  at point  $P_{t_1}$  and  $R(P_{t_2})$  at point  $P_{t_2}$  is known and assuming a constant rate of change in rainfall intensity we can express  $R(P_t)$  as:



$$R(P_t) = \frac{t_2 - t}{t_2 - t_1} R(P_{t_1}) + \frac{t - t_1}{t_2 - t_1} R(P_{t_2}) \quad (3-29)$$

and  $\Delta t = t_2 - t_1$  so that Equation 3-29 becomes,

$$R(P_t) = \frac{t_2 - t}{\Delta t} R(P_{t_1}) + \frac{t - t_1}{\Delta t} R(P_{t_2}) \quad (3-30)$$

Equation 3-30 is a linear combination of the rainfall rate  $R_{t_1}$  and  $R_{t_2}$ , where the weighting factors  $\frac{t_1 - t}{\Delta t}$  and  $\frac{t - t_2}{\Delta t}$  ensures a smooth transition of rain rate from time  $t_1$  to  $t_2$ . In order to change the time integral in Equation 3-28 into a path integral, Equation 3-30 needs to be expressed in terms of the vector path. Figure 3-10 is a schematic representation of the situation. The Rainfall is desired at point  $P_t$  and is spatially represented by the point  $S_{P|t}$ . For Figure 3-10 it can be safely inferred that all the precipitation ( $R_{t_1}$ ) along the path  $S_{t_1}$  to  $S_{P|t}$  has passed the point  $P_t$ . Similarly precipitation ( $R_{t_2}$ ) has also passed point  $P_t$  along the path  $S_{P|t}$  to  $S_{t_2}$ . Therefore, the linear weighting factors in Equation 3-30 can be expressed in terms of the vector path as,

$$\frac{t_2 - t}{\Delta t} = \frac{S_{P|t_1} - S_{t_1}}{\Delta s}; \quad \frac{t - t_1}{\Delta t} = \frac{S_{t_2} - S_{P|t_2}}{\Delta s} \quad (3-31)$$

where  $\Delta s = S_{t_2} - S_{P|t} = S_{P|t} - S_{t_1}$ . Substituting Equation 3-31 into Equation 3-30,

$$R(S_{P|t}) = \frac{S_{P|t_1} - S_{t_1}}{\Delta s} R(S_{P|t_1}) + \frac{S_{t_2} - S_{P|t_2}}{\Delta s} R(S_{P|t_2}) \quad (3-32)$$

Considering that,

$$\vec{V}_P = \frac{\Delta s}{\Delta t}; \quad dt = \frac{1}{\vec{V}_P} ds \quad (3-33)$$

and substituting Equation 3-32 and Equation 3-33 into Equation 3-28, an equation with known values for  $A_p$  is obtained:

$$A_P = \frac{1}{\vec{V}_P} \left( \int_{S_{P|t}}^{S_{P|t_1}} \left| \frac{S_P - S_{t_1}}{\Delta S} \right| R(S_P) ds + \int_{S_{P|t}}^{S_{t_2}} \left| \frac{S_{t_2} - S_P}{\Delta S} \right| R(S_P) ds \right) \quad (3-34)$$

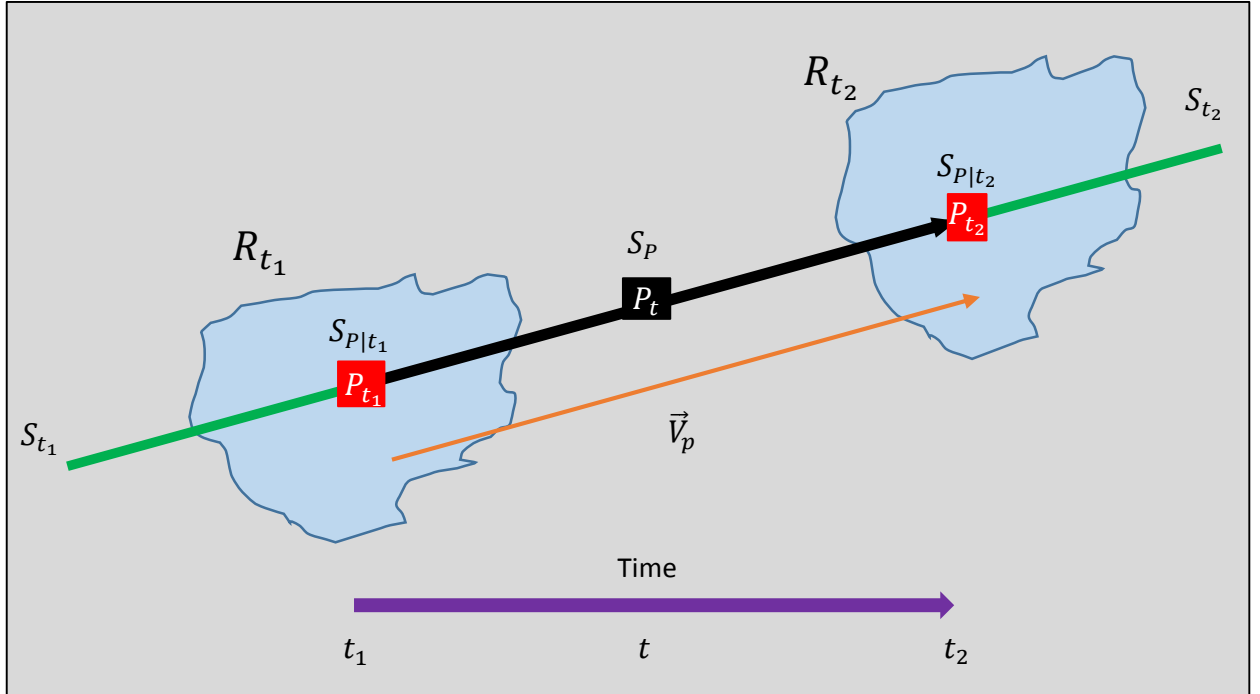


Figure 3-10: A schematic representation of the accumulation scheme. If the advection were not taken into account, the pixel at  $S_P$  would not receive any precipitation during this scan interval. The figure illustrates the location of a precipitation cell in two consecutive radar scans ( $R_{t_1}$  and  $R_{t_2}$ ). The motion vector  $\vec{V}_p$  illustrates the direction and speed of the precipitation cell. The total rainfall on the pixel located at  $S_P$  is the weighted sum of the integrals along the paths  $S_{P|t} - S_{t_1}$  and  $S_{t_2} - S_{P|t}$ .

A Trapezoidal approximation can then be utilized to solve the integrals in Equation 3-34. A number of iterations are performed which is depicted by the velocity vector. However, the velocity vector is related to the pixels per time step and is a non-integer value. The result is that the rainfall pixel will not correspond to a single ground value pixel, but will rather be spread over 4 neighbouring pixels. The rainfall pixel is calculated from the percentage overlap of each pixel (Figure 3-11). The calculated rainfall pixel can then be used for computation within the path integral.

The number of iterations within the path integral directly relates to its computational time. Computation time is reduced by relating the length of the vector to the number of iterations that needs to be performed (Sinclair, 2007). Thus, longer vectors will have sufficient iterations within the path integral, while vectors of length 0 will simple be an average of the

consecutive scans. In this way, computation time is much less while not sacrificing the quality of the calculations.

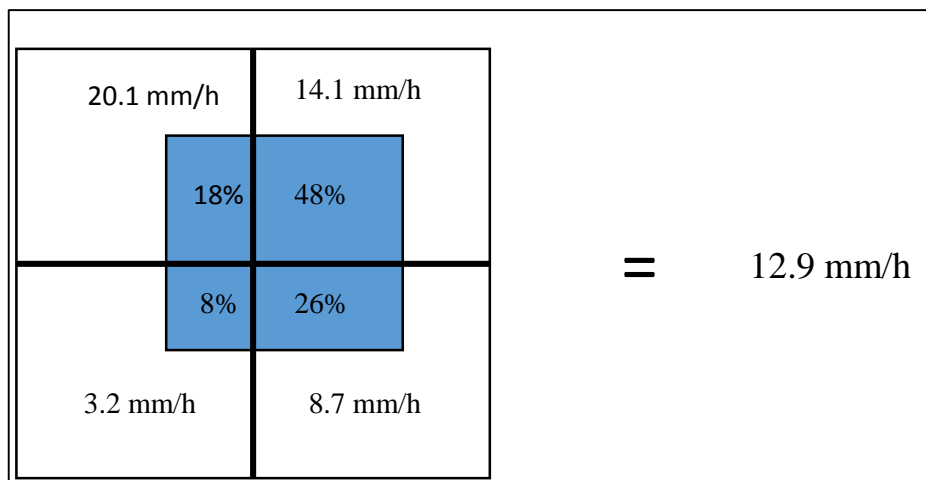


Figure 3-11: The figure illustrates an example of the percentage overlap for any given iteration of the integral. The pixel value is calculated by weighting the corresponding ground values.

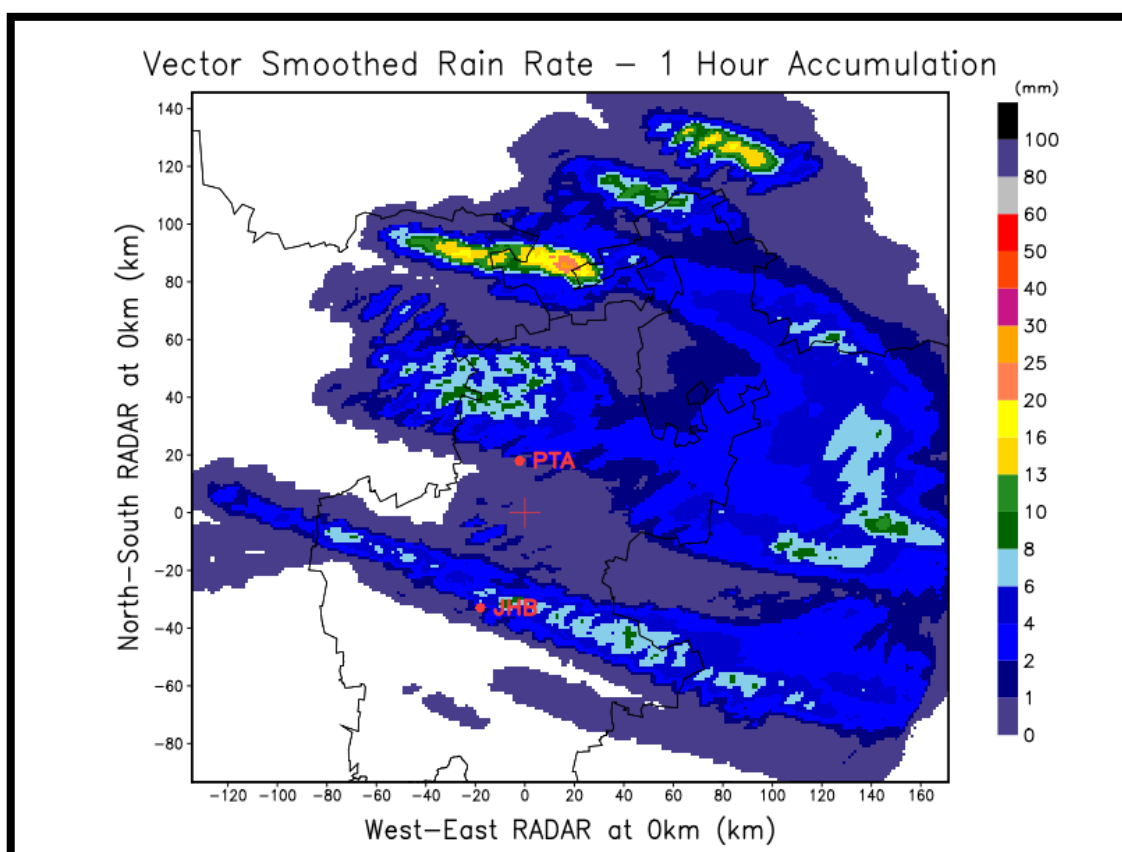


Figure 3-12: The same one hour accumulation illustrated in Figure 3-9 on 28 October 2010 at 03:00:00 UTC. The figure illustrates the difference after the accumulation technique was applied.

The result of this final step in the precipitation calculations produces a precipitation field that utilises a dual Z-R relationship and also accounts for the spatial and temporal evolution of the estimates. The result is illustrated in Figure 3-12 with the same hour accumulation illustrated within Figure 3-9. The technique preserves the precipitation depth while producing a realistic swath pattern, which is what one would expect a realistic precipitation pattern to look like.

### **3.7 Summary**

The QPE algorithm described in this chapter introduced techniques in calculating precipitation that were not previously available at the SAWS. The use of a classification scheme to categorise reflectivity allows for the use of dual Z-R relationships to try to reduce the errors associated with the DSD within different types of precipitation. Spatial errors associated with the temporal resolution of the scan strategy are accounted for by morphing a motion vector with the precipitation field. Then the desired motion vectors are obtained by employing an OFC technique. The next step is to evaluate the performance of the classification scheme. This will include determining with what skill the classification scheme can classify precipitation, the performance of the Z-R relationships, as well as the spatially smoothed precipitation. The data and methods used to evaluate the algorithm will be described in the next chapter.

---

## CHAPTER 4

# DATA AND EVALUATION METHODS

---

### 4.1. Introduction

The methods introduced in chapter 3 needs to be properly verified so that a conclusion can be drawn if they are in fact an improvement on the current precipitation scheme at SAWS. The algorithms' performance is measured by comparing their output to rain gauge measurements. It is assumed that rain gauges are a true measurement of surface precipitation. The algorithms are then compared with one another relative to their performance against the gauges. This chapter will describe the shortcomings and benefits of using rain gauge data for comparison. It will also highlight the benefit gained from switching to S-band wavelength radar. Finally the chapter will also discuss the methodology used to compare the radar estimates to gauge data, as well as give a summary on the advantages and limitations with the verification scores.

### 4.2. Rain Gauge Data

Rain gauges have an extensive history and are seen as the traditional method to measure the amount of rainfall within a determined period. It is often regarded as the true precipitation for a particular point of measurement. Ironically, this is also a limitation of the rain gauge and the next couple of sections will discuss the SAWS rain gauge network and its advantages and limitations.

#### 4.2.1. Rain Gauge Network over South Africa

As of November 2013 the SAWS rain gauge network consists of 22 manual weather stations of which 2 are first order stations, 3 second order and 17 third order stations. The station order is classified according to the amount of observations that are taken each day. First order stations record observations 3 times daily at 08:00, 14:00 and 20:00 SAST, second order twice a day at 08:00 and 14:00 SAST and third order once at 08:00 SAST. SAWS also coordinates 1254 rainfall stations, of which 26 are at official SAWS weather offices. The manual rainfall stations are being systematically replaced by the SAWS. A total of 33 Automatic Weather Stations (AWS) and 173 Automatic Rainfall Stations (ARS) have been deployed. The rainfall data is collected by the SAWS through a rainfall report send in by an observer or through an SMS

service by the AWS and ARS stations. Figure 4-1 illustrates the locations of the SAWS surface based rainfall observation stations. From Figure 4-1 the irregular spacing and scarcity of the rain gauges are evident. This will add to the difficulty of determining an accurate representation of the rainfall across large areas and/or the entire country (Deyzel, 2004).

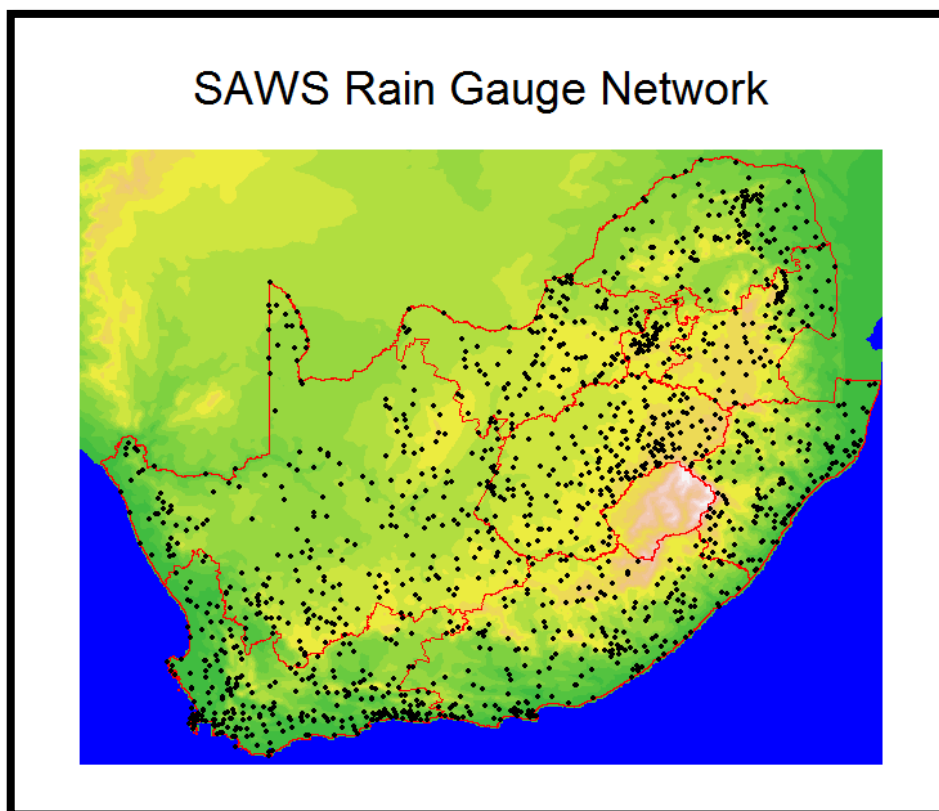


*Figure 4-1: A map illustrating the locations of the 1254 SAWS ground precipitation observation network*

#### **4.2.2. Advantages and Limitations**

Certainly, the biggest advantage with rain gauge measurements is their ability to directly measure the precipitation rate at the ground. The data collected can be easily interpreted to assist with any study. The instrument is easy to install and can become a reliable source of precipitation data provided that the instrument is properly maintained. Rain gauge data sets have a very long history which makes them favourable for climatological studies. They have also proven themselves invaluable with regard to radar calibration (Collier, 1986).

One of the more prominent limitations with rain gauges is their failure to capture the spatial variability of precipitation. It is difficult to interpolate or extrapolate rain gauge data in any accuracy or significant detail. At shorter time scales and distances the accuracy of the measurement are also dependent on rainfall type. Habib and Krajewski (2002) also

demonstrated that random errors exist between rain gauges situated within a distance of 1 metre from one another, and highlighted the discrepancies that can occur between radar and rain gauge accumulations. Rain gauges are also becoming increasingly elaborate, thus becoming more expensive thus opening up a new set of problems. The typical tipping bucket system is limited with a measurement resolution of no finer than 0.2 mm. Rain gauges tend to underestimate the rainfall in situations of heavy rainfall by as much as 20 to 40%, where the main sources of error are turbulence and increase wind flow above the gauge (Wilson and Brandes, 1979). The density of the SAWS rain gauge network is also decreasing over time. With fewer and fewer gauges available the accuracy of estimating the spatial variability of precipitation is decreasing.

### **4.2.3. Study Period**

The main aim of this study is to improve on an operational radar product. Thus, the goal is to evaluate the performance of the algorithms under operational conditions. The 2010/11 summer rainfall season (October 2010 – March 2011) was the period selected for evaluation of the Quantitative Precipitation Estimation algorithms. Since October 2010 the Irene radar provided high-quality data at a favourable temporal resolution of 6 minute intervals. Details of the scan strategy operational at the time at Irene are discussed in section 4.3.3. The relatively large collection of data will help to assess the radar's performance during the periods when precipitation is prevalent within the radar domain.

To put the season in perspective WB42 records (30 year climatological average from 1981 to 2010) were obtained from the SAWS. The stations, 8 of them in total within the radar domain, are listed in Table 4-1. Not Available (NA) is inserted where there was no data available. The total precipitation, together with the climatological average for each month of the study period is listed. The monthly average total precipitation over for the 8 stations for the rainfall season of October 2010 – March 2011 is illustrated by Figure 4-2. The orange bars represent each corresponding month the recorded precipitation for the study period, while the blue bars represent the climatological average as calculated from the WB42 records. The months of October, November and February indicate that the rain gauges received below normal rainfall, with October being the driest receiving only 48% of the climatological monthly average. However, December, January and March indicates more precipitation than normal, with December being particularly wet receiving 69% more precipitation than the norm. For the season the average precipitation over the 8 gauges for the six month period was 105.2 mm, while the average climatological precipitation for the 8 station of the same six month period is 93.0 mm. Thus, the season received 13% more precipitation than normal.

Table 4- 1: Rain gauge stations listing the total precipitation per month compared to the Climatological value. Not Available (NA) is inserted where there was no data available and the direction to gauge and range to gauge is respective to the Irene S-band radar.

Total Precipitation (mm)														
STATIONS	Direction to Gauge (°)	Range to Gauge (km)	October 2010		November 2010		December 2010		January 2011		February 2011		March 2011	
			Station Tot.	Clim	Station Tot.	Clim	Station Tot.	Clim	Station Tot.	Clim	Station Tot.	Clim	Station Tot.	Clim
IRENE WO	0.0	0.0	24.2	67.4	62.8	99.2	197.7	119.0	196.3	120.8	117.8	100.6	106.2	90.5
JHB BOT TUINE	218.1	34.0	35.6	63	51.6	79	186.2	111	111.2	123	82	97	157.6	85
JOH INT WO	175.7	26.8	29.4	79	109.9	103	209.6	124	170.1	135	63.8	112	135	101
PILANESBERG	306.1	122.0	6.6	51	60.6	63	249	101	130.4	86	32.6	87	147.8	77
RUSTENBURG	286.2	102.3	5.2	56	90.6	69	NA	94	NA	108	NA	85	86.6	69
SECUNDA	124.1	117.8	65.4	88	77.8	114	193.4	136	178.2	149	20.6	89	NA	81
VEREENIGING	199.4	77.9	23.4	63	79.4	86	208.6	104	NA	106	NA	69	66.8	74
WARMBAD	6.2	113.0	65	59	29.8	86	112.6	129	NA	112	NA	82	102	83
Average =			31.9	65.9	70.3	87.4	193.9	114.9	157.2	117.3	63.4	90.2	114.6	82.5
											<b>Ave Total =</b>		<b>105.2</b>	<b>93.0</b>



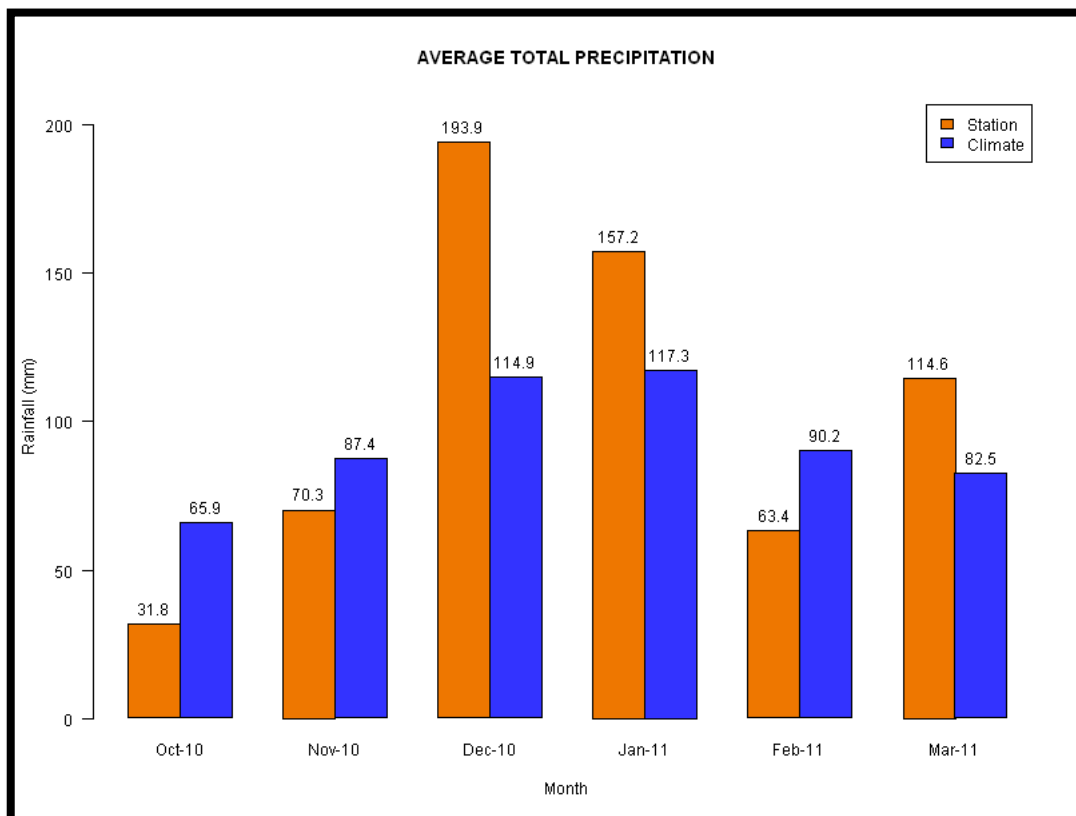


Figure 4-2: The average precipitation for the rainfall season of October 2010 – March 2011 for the 8 station with WB42 data. The average total precipitation for each month (orange) is compared to the average total climatological precipitation (blue).

#### 4.2.4. Quality Control of Gauge Data

Rain gauges within a 300km radius of the Irene radar was selected for the study period. Due to gauge measurement errors and unreliable gauge hardware, the gauges needed to be extensively quality controlled (QC) before comparisons with radar data could be made. The first step was to examine the data for unrealistic values such as negative numbers and extreme maxima. The next step was to flag gauges that had less than 22% of data available. This equates to  $\pm 40$  days of data out of the 182 day study period. Most of the flagged gauges had intermittent reports, were not reliable and had to be removed from the data set. A 25km<sup>2</sup> box was then aggregated over the Irene radar domain. The correlation-coefficient between precipitation measurements and corresponding p-values were calculated, as defined by Wilks (2005), and compared between gauges within this 25km<sup>2</sup> box. Thus, all gauges that exceed the p-value test level of 5%, the most commonly used significance level (Wilks, 2005), were considered as insignificant and were removed from the dataset. This resulted in removing gauges that were reporting zero millimetres of rainfall for more than 90% of the study period. Finally, the data of the remaining

gauges was plotted and manually inspected for any irregularities in the data and gauges with unrealistic precipitation data were removed.

Figure 4-3 illustrates the locations of the rain gauges that made it through the QC process. The blue dots in the figure represent gauges that are capable of measuring precipitation in an hourly temporal resolution while the red dots are 24 hour totals of precipitation measured at 08h00 SAST daily. A total of 70 hourly gauge and 333 twenty-four hour gauges were available for the study. It is worth noting that even with the strict QC procedures that there still may be some errors present within the rain gauge dataset.

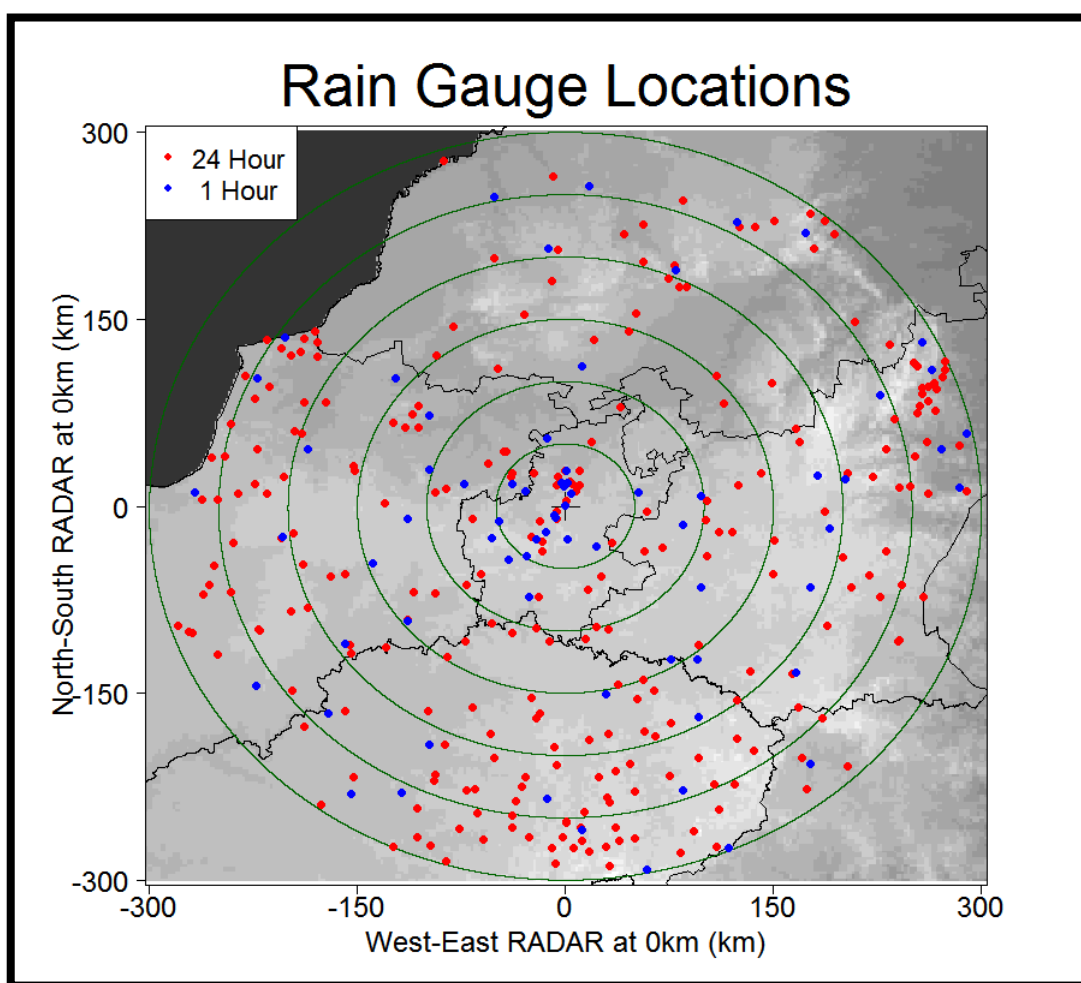


Figure 4- 3: Locations of rain gauge that made it through Quality Control (QC) within a 300km radius of the Irene radar. Red gauges are only capable of daily totals while blue gauge are capable of an hourly temporal resolution.

### 4.3 Weather Radar Data

The following subsections will discuss the Irene weather radar data and some of the advantages and limitation associated with it.

### 4.3.1. The Irene Radar

This study primarily focuses on the Irene Weather Radar (See Figure 4-4). The radar is 1560 m Above Mean Sea Level (AMSL) and is situated at 25.91°S and 28.21°E, about 25km North of O.R. Tambo International Airport. Construction of the radar started in October 2009 and was completed by mid-November 2009. The first volume scan was subsequently received on the afternoon of 12 November 2009. After some fine tuning of the system the radar was commissioned in January 2010 for operational use. A scan strategy, which is described in section 4.3.3., was implemented. The scan strategy ran operationally until October 2010 when the use of the Doppler filter was introduced. This decreased the effects of Ground Clutter (GC) and Anomalous Propagation. In July 2011 the radar firmware and controller software were upgraded. A new scan strategy with reduced range to improve data quality and unambiguous Doppler velocity measurements was installed. This scan strategy is not discussed in detail because it only became operational after the data was collected for this study.

This METEOR 600S radar from the German company, Gematronik Weather Radar Systems, operates at a frequency of 2.7 – 2.9 GHz, which is designated as the S-band frequency. Thus the radar has an electromagnetic wavelength of  $\pm 10$ cm. The radar can alternate between pulse durations of 0.8-3.3 $\mu$ s as well as a Pulse Repetition Frequency (PRF) of between 250-1400Hz. Four volume data files are created:

1. The raw or uncorrected reflectivity field in dBZ, which show the reflectivity field without undergoing any filtering.
2. The corrected reflectivity field in dBZ with pre-processed filters applied such as the Doppler filter
3. The Doppler velocity in m/s, which is the radial component of the wind velocity relative to the radar
4. The spectrum width or standard deviation in m/s, within a sample volume relative to the mean Doppler velocity in m/s.

The antenna has a diameter of 8.5 m, which allows for an antenna gain of 44.5 dB as well as a half power beam width of 1°. The magnetron transmitter is capable of producing a peak power output of 850 kW and the super heterodyne receiver has a dynamic range of 105 dB.

Software that allows for maintenance and control of the radar is provided by the Ravis® software suite and meteorological products are controlled through the Rainbow® software suite. The 600S radar can also be easily upgraded to Dual-Polarized capabilities if the need arises. This will allow four additional products to be generated, namely:



*Figure 4-4: The Irene METEOR 600S S-band radar during construction in 2009, (a) and (b), as it stands today (c) at the Irene WO just outside Pretoria, Gauteng.*

1. Differential Reflectivity (ZDR),
2. Differential Phase shift ( $\Phi$ DP),
3. Specific Differential Phase Shift (KDP) and,
4. Polarimetric Correlation Coefficient ( $\rho$ HV).

Currently the radar at Irene is operated in single polarisation, pulsing with the electric component of the electromagnetic wave at a horizontal orientation. For a detailed description of the METEOR 600S specifications, please refer to the online documentation available on Gematronik webpage.

Figure 4-4 (c) is a photograph of the S-band Radar as it stand today at the Irene WO. In Figures 4-4 (a) and (b) the radar can be seen during different phases of construction. Figure 4-4 (a) show the construction of the 15m tower completed and the 8.5m reflector assembled, ready to be hoisted onto the tower. In Figure 4-4 (b) the reflector is secured on top of the tower and construction of the radome is underway. The tiles from which the radome is constructed will form a round sphere protecting valuable radar equipment from damage due to weather elements.

### 4.3.2 Advantages and Limitations

Moving from a C-band radar network to a network that will operate in the S-band frequency has a number of advantages that will be described in this section. The only real disadvantage S-band radars have is that they are expensive to build and maintain. Below, two advantages are described that make the S-band worth its while, if the budget allows for it.

#### *i. Attenuation*

In a radar context, attenuation is defined as the loss of power when electromagnetic radiation passes through a medium. The amount of power that is lost is dependent on (i) the frequency of the beam and (ii) the density of the medium through which the radiation has to travel. Thus attenuation is the loss of power that the electromagnetic radiation will experience travelling from the antenna to the target and back again. This reduction of intensity along the transmitted path can be expressed as:

$$d\bar{P}_r = 2k_L\bar{P}_r d_r \quad (4-1)$$

where  $d\bar{P}_r$  is the incremental reduction of backscattered power  $\bar{P}_r$  caused by absorption and scattering of the medium between the radar set and the target,  $d_r$  is the increment of the range  $r$ , and  $k_L$  is the attenuation coefficient having dimension (length)<sup>-1</sup> (Battan, 1973). The factor 2 is

included in the equation due to the path having to travel to and from the target. By integrating Equation 4-1 over a path of range  $r$  and expressing it in terms of decibels, it can be written as:

$$10 \log \frac{\bar{P}_r}{\bar{P}_{r0}} = -2 \int_0^r (k_g + k_c + k_p) dr \quad (4-2)$$

where  $\bar{P}_{r0}$  is the power which would have been received had there been no attenuation. The advantage of expressing the equation in decibels per unit is that the different causes of power loss can be simply added to give the total attenuation. Here  $k_g$ ,  $k_c$  and  $k_p$  represent attenuation by atmospheric gases, clouds and precipitation respectively.

Attenuation effects can result from both absorption and scattering. Gases and clouds primarily act as absorbers but scattering needs to be considered when large hydrometeors are present. Attenuation through gases at the 3 most used weather radar frequencies (10cm, 5cm and 3cm) are usually small and can be ignored. However, when shorter wavelengths are used such as the K-band (1.25cm) gases like water vapour can cause significant power losses. Gunn and East (1954) illustrated that water in clouds attenuates electromagnetic radiation more than ice particles. However, at the 5- and 10cm wavelengths cloud attenuation can be safely ignored.

Attenuation can also be caused by precipitating particles, these include rainfall, snow and hail. When considering rainfall Wexler and Atlas (1963) list a table (Table 4-2) of one way rain attenuation at different frequencies. The values listed in the first column as M-P were calculated from the standard Marshall-Palmer distribution assuming Mie scattering. The Modified M-P took into account that at diameters below 1.0-1.5mm the drop-size spectra differ from the standard M-P. Mueller and Jones (1960) used raindrop spectra attained from shower-type precipitation. The last column lists  $K' = \frac{k_p}{R}$  as a function of wavelength at the temperatures indicated in the column. Attenuation for most wavelengths is proportional to  $R$ . From Table 4-2 it can be concluded that rain attenuation at the 10cm wavelength can be safely ignored. Using the values from Mueller-Jones an S-band wavelength radar at a precipitation rate of 100 mm/hr will only lose 0.092 dB/km. Thus, the power loss through a storm that is 10 km wide will only be 1.84 dB. A C-band radar will experience losses of around 6.6 dB travelling through a similar storm. With the standard Marshall-Palmer reflectivity to rain-rate conversion a 100 mm/hr is equivalent to 55dBZ. Power losses for an S- and C-band radar would result in a rain-rate measurement of 76.6 mm/hr and 38.6 mm/hr respectively. Although snow and hail affects attenuation of the electromagnetic radiation differently than rain, the effects on the different wavelength remain the same. The advantages an S-band radar has over a C-band radar with precipitation measurements are clear.

Table 4-2: One-Way Rain Attenuation  $K' \left( \frac{dB/km}{mm/hr} \right) =$  (Wexler and Atlas, 1963)

Wavelength (cm)	M-P (at 0°C)	Modified M-P (at 0°C)	Mueller-Jones (at 0°C)	Gunn and East (at 18°C)
<b>0.62</b>	0.50-0.37	0.52	0.66	-
<b>0.86</b>	0.27	0.31	0.39	-
<b>1.24</b>	$0.117R^{0.07}$	$0.13R^{0.07}$	0.18	$0.12R^{0.05}$
<b>1.8</b>	-	-	-	$0.045R^{0.11}$
<b>1.87</b>	$0.045R^{0.10}$	$0.050R^{0.10}$	0.065	-
<b>3.21</b>	$0.011R^{0.15}$	$0.013R^{0.15}$	0.018	$0.0074R^{0.31}$
<b>4.67</b>	0.005-0.007 *	0.0053	0.0058	-
<b>5.5</b>	0.003-0.004 *	0.0031	0.0033	-
<b>5.7</b>	-	-	-	$0.0022R^{0.17}$
<b>10</b>	0.0009-0.0007 *	0.00082	0.00092	0.0003

\*The first value applies at 2 mm/hr, the second at 50 mm/hr, and there is a smooth transition between them.

Figure 4-5 illustrates an example of how attenuation would look on a radar display. In this particular case at the Bloemfontein Enterprise C-band radar the storm detected on 20 November 2001, directly to the west of the radar caused attenuation, resulting in precipitation behind the storm (from a radar perspective) to be under-estimated. A large sector of stratiform precipitation (indicated by the red V shape on Figure 4-5), is not being detected by the radar due to the presence of the heavy precipitating storm to the west of the radar.

Figure 4-6 illustrates the Enterprise C-band radar at Bloemfontein detecting a severe storm 80km to the North-West of the radar. Figure 4-6 (a) displays the storm's position relative to the radar. Figure 4-6 (b) displays the storm and illustrates a feature that often accompanies severe storms when operating in the C-band range. The feature pointed out by the arrow marked A is attenuation caused by the storm core. It consists of very large water drops and water coated hail, which is evident from the reflectivity above 60 dBZ. The bean shape echo is thus a result of attenuation to the back of the storm causing under-estimation of its intensity. This feature will shift its position relative to the position of the radar as the storm progresses. This will cause errors in estimating areal rainfall. Trying to correct for these errors before estimating

precipitation can often lead to larger errors. Hitschfeld and Bordan (1954), showed that precipitation estimates that had no attenuation correction applied to the reflectivity field often illustrated better results. By estimating precipitation at non-attenuating wavelengths, like the S-band radar located at Irene, would yield the best result for quantitative precipitation estimations.

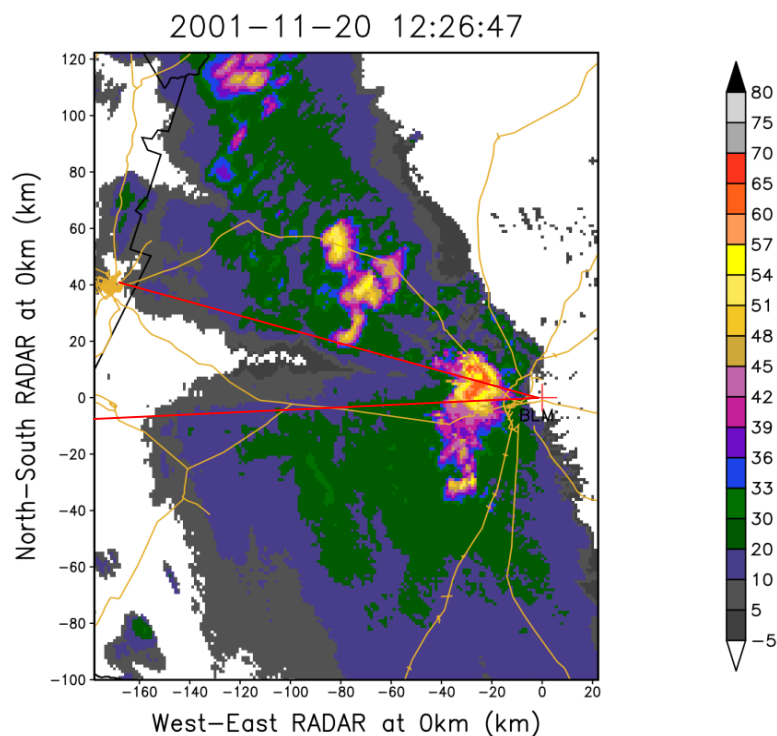


Figure 4-5: The Enterprise C-band Radar at Bloemfontein illustrating signs of attenuation. A sector of lower reflectivity is observed directly to the West of the storm (relative to the radar) compared to the surrounding region. This sector is mark by the red lines.

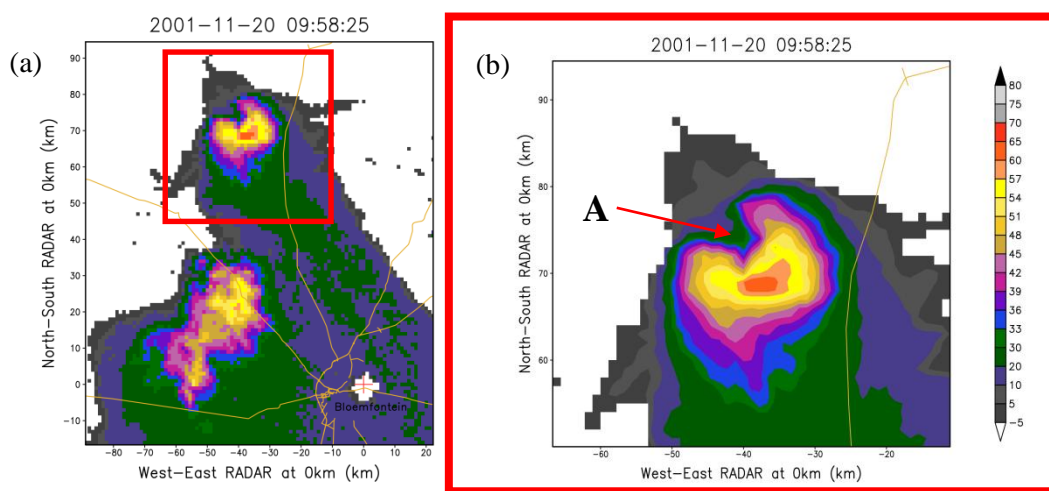


Figure 4-6: Reflectivities from a storm detected by the Enterprise C-band Radar at Bloemfontein show signs of attenuation. The location of the storm relative to the radar is



*illustrated in (a). Hail inside the storm (b) is causing significant attenuation, so part of the storm away from the radar is significantly underestimated. This region is pointed out by the arrow marked A. Note the high reflectivities in the core in the range 65 – 70 dBZ.*

## *ii. Radio LAN Interference*

Originally, the main open band used by wireless transmitting devices was about 2.4GHz. However, the overwhelming popularity of these devices, and a number of other services that share the spectrum, led to the frequency range becoming congested. At the World Radio Conference in 2003 portions of the 5GHz band were allocated for unlicensed use by mobile and Radio LAN (RLAN) devices. The 5150 – 5350 MHz and 5470 – 5725 MHz bands were allocated for these devices and the use of dynamic frequency selection (DFS) was made mandatory for these frequency bands. DFS allows for an access-point to automatically select a frequency with low interference. The Independent Communication Authority of South Africa (ICASA) is responsible for issuing licenses for devices to operate in specific frequencies in South Africa. Unfortunately, ICASA did not enforce DFS to be switched “ON” in RLAN devices approved for use in South Africa. The resulting interference to the C-band weather radars, which operate in the “meteorological” band of 5600 – 5650 MHz, is shown in Figure 4-7. The first RLAN interference was observed at the end of 2006. ICASA played a big role in locating and attempting to ensure the closing down of RLAN links operating in the C-band radars’ frequency, but due to the large number of devices, the Authority could not keep up with policing the users of the technology (de Waal et al., 2008).

The consequence is that any attempt to accumulate precipitation reflectivities in the C-band range is severely compromised. The RLAN interference effectively renders the precipitation products from the radar useless. In an attempt to minimize the damage from the interference, the National Centre for Atmospheric Research (NCAR), which is also developers of the TITAN software, developed a filter to reduce the unwanted interference. Since the radar is a non-Doppler system, the only data available for filtering is the radar reflectivity. Using the signal-to-noise ratio (SNR) the filter considers one beam at a time. The interference shows as the SNR at some level above the calibration noise of the radar receiver. The filter algorithm computes a histogram of the SNR values and looks for a strong peak in the histogram. Weather signals are generally spread across the histogram while interference signals will have a spikier SNR and will show up concentrated in a small number of bins. The Power received from the interference is estimated by the chosen SNR. This estimated power is then subtracted at each range gate and the reflectivity is then computed from the remaining power (de Waal et al., 2008).

The filter manages to remove most of the interference but the result is not perfect. It also has a tendency to remove weak stratiform precipitation. Figure 4-8 illustrates an example of this at the Port Elizabeth radar. The first image at 10:21:10 UTC shows that the filter was active; in the next image at 10:25:52 UTC the filter was deactivated. At this instance no interference was detected during this stratiform rain event, but the active filter still removed a crucial amount of precipitation information.

### RLAN interference on the C-band radar frequencies at various locations

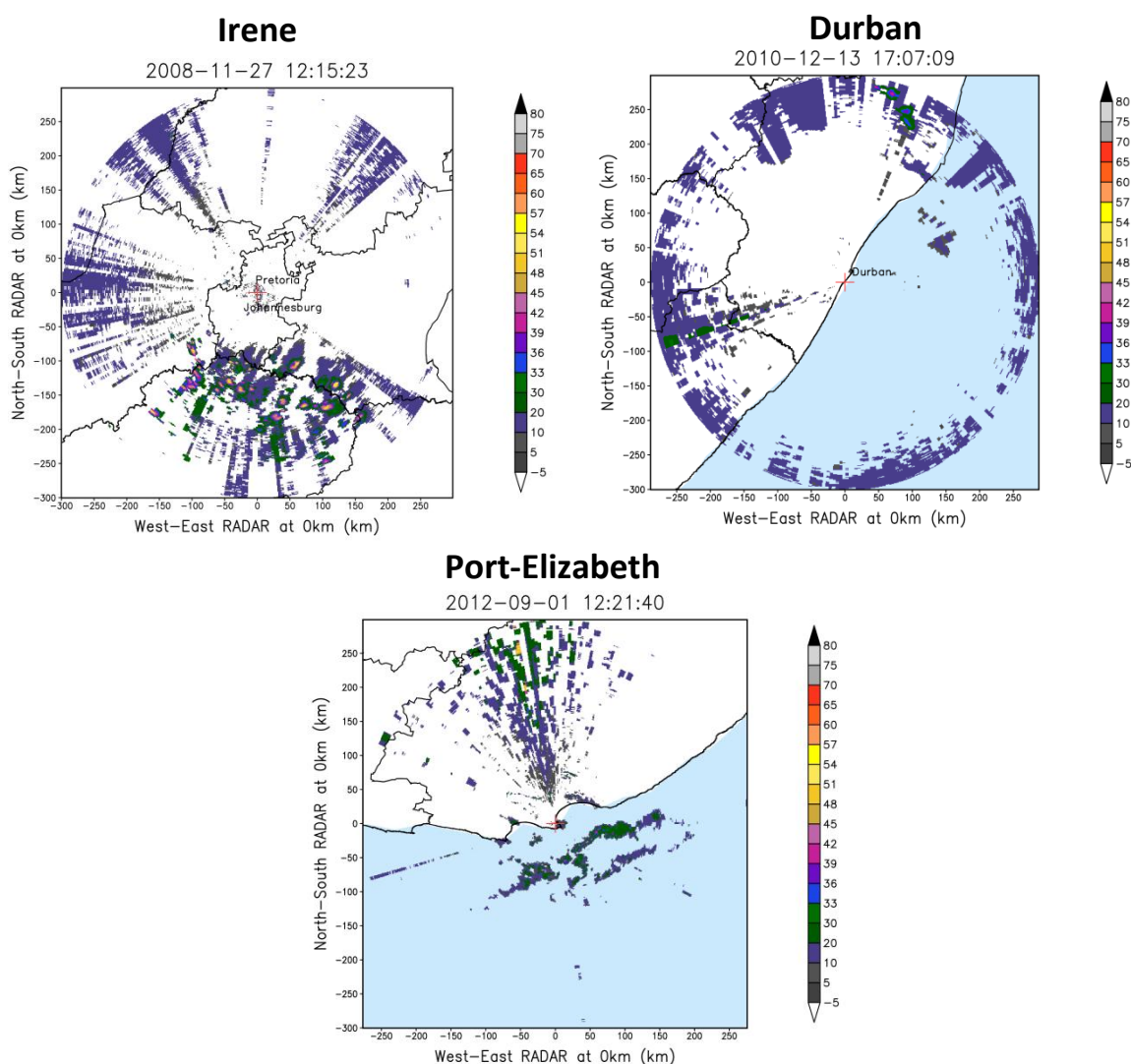


Figure 4-7: Radar displays showing RLAN interference at Irene, Durban and Port-Elizabeth radars.

The consequence is that, even if the interference filter worked perfectly and removed none of the weather related echoes and all of the inference echoes, RLAN interference will still cause significant errors in precipitation estimation. The reason for this is that, when a storm

moves into an area suffering from severe interference, the storm will be filtered with the rest of the inference or its intensity significantly reduced. The best solution is to change the operating frequency of the radar, hence the decision of the SAWS to shift to the 2.8GHz S-band radar systems.

### 4.3.3 Scan Strategy

The S-band radar at Irene makes use of a volume scan technique. The Antenna rotates in azimuth at  $1^\circ$  intervals while continuously pulsing. The first scan starts at the highest elevation of  $30^\circ$  and make twelve steps down to an elevation of  $0.5^\circ$  where the scan finishes, before repeating. The elevation scans are graphically illustrated in Figure 4-9 by the blue lines. Each blue line represents the centre of the beam axis and the corresponding height above level ground with range takes the earth's curvature and standard refraction of the atmosphere into account. The scan process takes about 355 seconds and gives the radar an overall temporal resolution of 360 seconds (6 minutes).

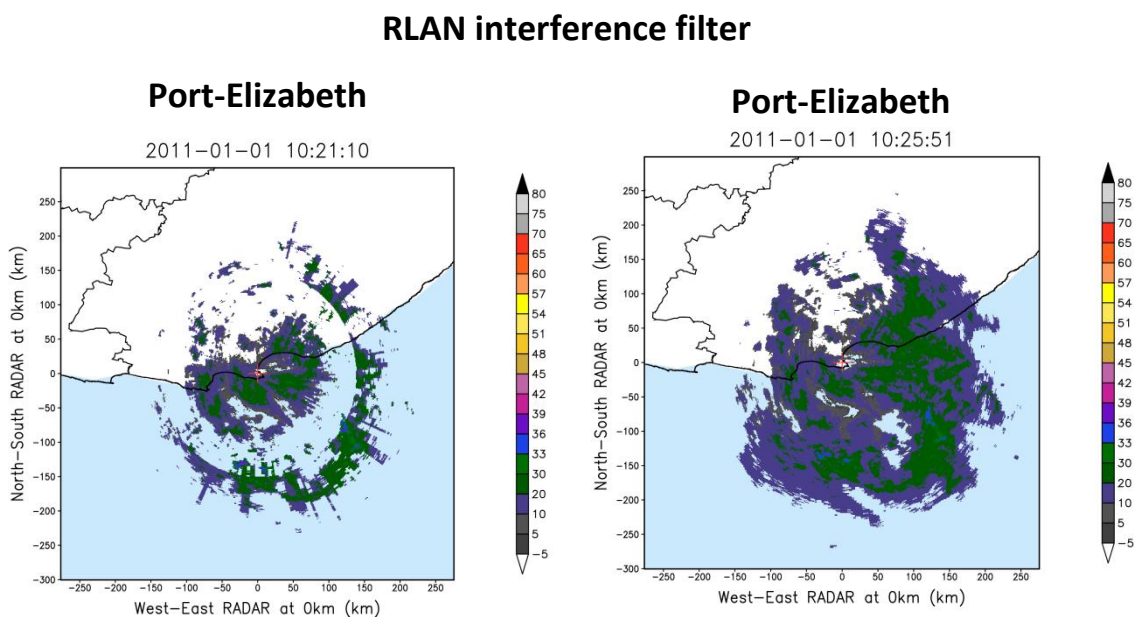


Figure 4-8: Example of the Port Elizabeth radar running with the filter (Left), and without (Right). The two image are five minutes apart.

The high temporal resolution was selected due to the nature of thunderstorms on the Highveld. A single cell thunderstorm life-cycle can be as short as 30 minutes. To fit twelve elevation scans within a 6 minute time frame the antenna speed varies from the top elevation to the bottom. The antenna will rotate a  $30^\circ/s$  at the top to  $10^\circ/s$  at the bottom, because the lower the radar beam gets, the further it needs to travel through the atmosphere to capture the reflectivities due to

precipitation below a typical maximum height of 16 km. The pulse duration will alternate from  $0.85\mu\text{s}$  for the higher elevation and  $1.64\mu\text{s}$  for the lower elevation. The longer pulses at the lower half of the scan ensure that enough power is transmitted to observe meaningful reflectance. The resulting pulse length is 125 m, which are range-averaged over 4 samples to produce 500 m range bins.

Due to the radar having Doppler capabilities the Doppler Dilemma influences the setup to the radar. The maximum range a radar can operate at and the maximum unambiguous velocity the radar is capable of detecting is all depended on the Pulse Repetition Frequency (PRF). Solving the equation that determines the maximum range and maximum unambiguous velocity results in the follow equation known as the Doppler Dilemma:

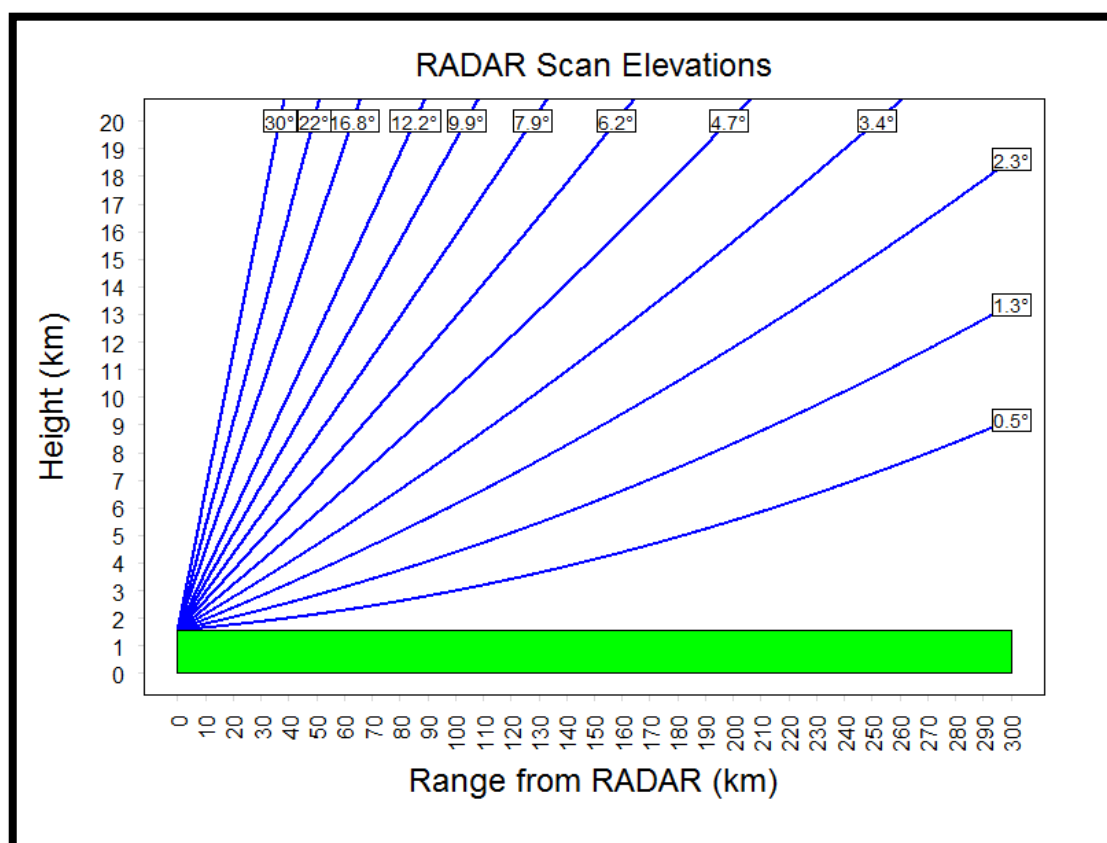


Figure 4-9: An illustration of the height AMSL with range of each elevation in the radar scan strategy (blue line).

$$V_{max}r_{max} = \frac{c\lambda}{8} \quad (4-3)$$

Here  $V_{max}$  is the maximum unambiguous velocity and  $r_{max}$  the maximum range. The speed of light is represented by  $c$  and the radar wavelength by  $\lambda$  (Reinhart, 2004). The term on the right is

a constant because the wavelength of the radar cannot be changed. The result is that, in order to detect large velocities, the range of the radar needs to be small (and vice versa) in order to detect echoes at long ranges. A partial solution to this is to increase the wavelength of the radar, which is another advantage the S-band radar has over its C-band counterpart. The PRF can be no higher than 500 Hz for the radar to operate successfully at a 300 km range. However, this results in a maximum unambiguous velocity of only  $13.1 \text{ ms}^{-1}$  ( $47.1 \text{ kmh}^{-1}$ ), even with the use of the S-band's longer wavelength. A dual-PRF setting can be activated that allows the radar to pulse at alternate PRF's of 500 Hz and 400 Hz (Joe and May, 2003). The result of this strategy is that the radar can operate at a 300 km range and detect a maximum unambiguous velocity of  $52.3 \text{ ms}^{-1}$  ( $188.28 \text{ kmh}^{-1}$ ). This allows the Doppler filter to operate more efficiently, which is crucial for filtering ground clutter and anomalous propagation. This in return will allow for better precipitation estimation.

*Table 4-3: The volume scan strategy used during the study period.*

Elevation Scans (°) (top-bottom)	<b>30, 22, 16.8, 12.2, 9.9, 7.9, 6.2, 4.7, 3.4, 2.3, 1.3, 0.5</b>
Beam Width (°)	1
Range (km)	300
Bin resolution (km)	0.5
Pulse Duration (µs)	0.85-1.64
PRF (Hz)	500 - 1200
Azimuth Interval (°)	1
Samples per Beam	18 to 22
Antenna Speed (°/s)	30 to 10
Temporal resolution (S)	355

However, the dual-PRF method has its drawbacks due to the fact that it decreases the beam sampling to between 18 and 22 samples per beam. The result is that the signal-to-noise filter will remove crucial information. Thus, the decision was made in July 2011 to reduce the radar's range to 200 km in order to receive higher quality data from the radar. Table 4-3 lists a summary of the scan parameters of the S-band at Irene as set during the study period of the 2010/2011 summer rainfall season.

#### **4.3.4 Data Pre-Processing**

After each scan interval, four data files are produced as mentioned in section 4.3.1. The files are in the Gematronik volume format (VOL). These files consist of 2 parts, an XML and binary

part. The XML part consists of Meta data describing the data set and the binary data that accompanies the file. The binary data is stored in polar coordinates, with each value corresponding to a particular elevation and azimuth angle scanned as well as the range from the radar. However, the SAWS radar data processing system is built around the MDV (Meteorological Data Volume) format and uses the TITAN system extensively. The MDV file is also in binary format whose main advantage is the fast data access speed that is a result of its binary nature. Each MDV file consists of a file header, which defines the layout and content of the data portion which follows. The format is capable of storing multiple “Fields” (such as reflectivity, precipitation, velocity, etc.) within one file at a number of “Levels” and coordinate systems. This allows for the data to be represented in its 3 dimensional structure relative to the radar.

In order to utilise the data in this study the VOL data needed to be converted into MDV format. The TITAN system has an application **GemVolXml2Dsr** that allows the unpacking of VOL data as FMQ (File Message Queue) data. FMQ data is a temporary storage file that holds information about the current radar scan, which is then later converted in to MDV format for permanent storage. From the FMQ file, the TITAN application **Dsr2Vol** can generate the user specified MDV files. For this study the corrected reflectivity file (dBZ.vol), assuming that all ground clutter is removed by the Doppler filter, was used to create the instantaneous MDV file. The raw VOL data was interpolated to a Cartesian coordinate system with 1 km square horizontal grid cell size and a stack of 37 vertical levels separated by 0.5km.

## **4.4 Quantitative Precipitation Estimation (QPE) Algorithms**

The next few section will discuss how the QPE algorithms were calculated using TITAN applications and extracted CAPPI levels.

### **4.4.1 CAPPI Levels**

One of the objectives of the study was to evaluate how the algorithm performs at different heights above the radar. Thus, a number of CAPPI levels were extracted on which to run the precipitation algorithm. The extracted CAPPI levels chosen were: 2.5, 3.0, 3.5, 4.5, 5.5, 7.0, 8.5 and 10.0 km AMSL. With the Radar at 1.5km AMSL the CAPPI levels translate to 1.0, 1.5, 2.0, 3.0, 4.0, 5.5, 7.0 and 8.5 km respectively above the Radar. The choice was limited to 8 CAPPI levels due to computation time limitations. Because of the logical assumption that precipitation measurement will be more representative of the rain gauge measurements closer to the surface of the earth, the CAPPI levels are separated by 0.5km in the lower atmosphere, 1.0km in the middle and 1.5 km in the upper atmosphere. The CAPPI levels are graphically illustrated in Figure 4-10 by the red lines. It shows clearly that the lower CAPPI levels will have the least

amount of information due to increase in height with range of the lowest elevation scan of  $0.5^\circ$ . The 2.5 km level CAPPI will have a maximum range of only 73 km from the radar. The range of the CAPPI levels will increase with the increase in height of the CAPPI level as the base-scan rises above ground. Thus, only the 10.0 km CAPPI level has the 300 km range of the radar. A similar situation is observed with the near-by range of the CAPPI levels at height. This is due to the blind spot above the radar known as the cone of silence. The result is that the 10.0 km CAPPI level will not have any data within 17km range of the radar.

#### 4.4.2 Precipitation Algorithms

For each of the extracted CAPPI levels the dBZ reflectivity is converted into precipitation estimates as described in chapter 3. Two precipitation products are created at different stages in processing the CAPPI levels. The first precipitation product, which is referred to as the Classified Rain Rate (CRR), is generated using the dual Z-R relationship with the classification technique applied, i.e. no morphing of the motion vectors was done. The CRR algorithm created from CAPPI data will be used in the verification process to determine if it is an improvement to the single Z-R relationship used in the TITAN algorithm currently operational at the SAWS (see section 4.4.3).

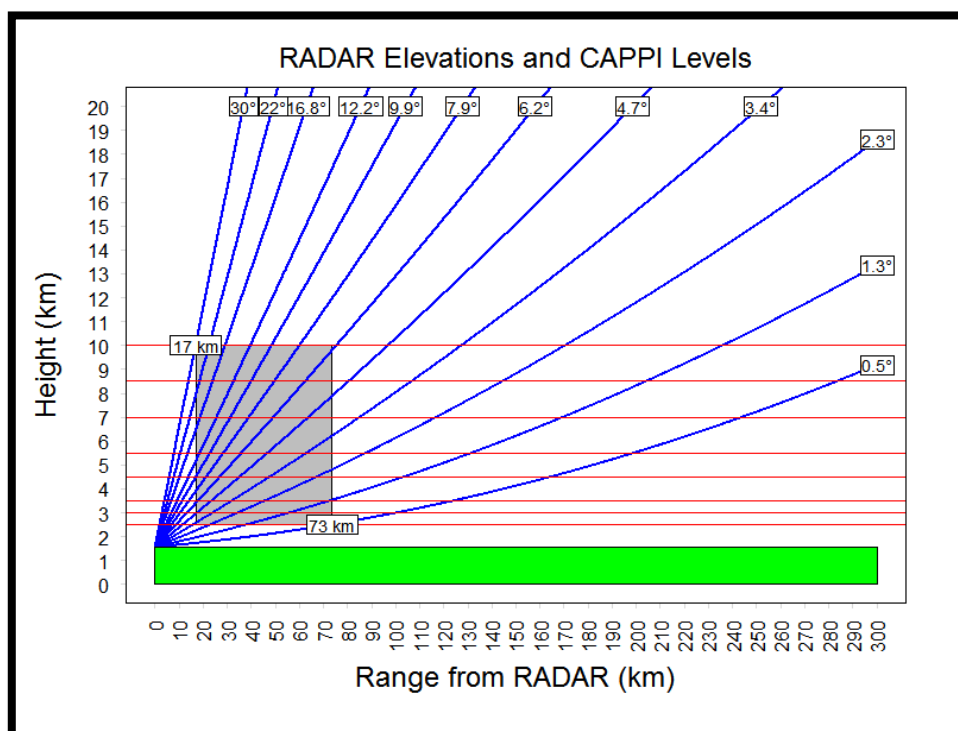


Figure 4- 10: An illustration of the height above AMSL with range of each elevation in the radar scan strategy (blue line). The extracted CAPPI levels are represented by the red lines. The grey rectangle illustrates the region of 17 – 73 km range from radar where all the CAPPI levels are comparable to rain gauges, which lie below the cylinder.

The second algorithm is the CRR precipitation estimate which is morphed with the motion vectors and will be referred to as the Optical Flow Rain Rate (OFRR). This algorithm will then be verified against the other precipitation algorithms in order to determine if there are any improvements obtained by using the motion vector morphing technique.

Both algorithms produce instantaneous precipitation estimates valid for the current 6 minute scan. The files are ingested into the **PrecipAccum** application in the TITAN software (describe further in section 4.4.3 below) to produce 1 hour and 24 hour accumulations so that a comparison with gauge data can be made.

### 4.4.3 TITAN Precipitation

The TITAN algorithm that runs operationally at the SAWS for the Irene radar is generated by the **PrecipAccum** application within TITAN. The data is converted into a Cartesian coordinate plain MDV file as described in section 4.3.4. The MDV file is input to the **PrecipAccum** application, which is set up to search for the maximum reflectivity within a 0 – 30 km vertical column in the Cartesian plane. A single Z-R relationship, the Marshall-Palmer relationship ( $200R^{1.6}$ ), is applied to the maximum reflectivity across the field to produce precipitation estimates. As one of the objective is to see if the CRR and OFRR algorithms can improve on the TITAN algorithm, it was decided not to adjust any of parameter that were currently producing operational precipitation product. A 2 dimensional MDV file with the surface precipitation estimates in millimetres of rain (mm) is produced by the application. Due to discrepancies with the start and end time within the MDV file as a result of the conversion from raw volume data, the precipitation estimates are forced to be scaled by 6 minute intervals so that they will correspond to the radar scan temporal resolution.

Accumulations are also generated by the **PrecipAccum** application. By altering the input parameters so that the application reads precipitation values instead of reflectivity values, accumulations can be calculated for any desired time interval. One hour and twenty-four hour accumulations were created by the application. The application was setup to produce an output file at the top of each hour, weighting the start and end scans for the accumulation appropriately if they should overlap. However, this latter effect should be trivial because the radar scan was synchronised to start its scanning with the start of every hour. The precipitation values can now be extracted and compared with surface gauge observations.

## 4.5 Verification of QPE Performance

The next few sections will discuss the verification techniques used to evaluate the algorithm with gauge measurements.



### 4.5.1 Evaluation Method

Due to the limitations of gauges to point locations, and their relative errors in measurement discussed in section 4.2.2, a point location evaluation method was selected instead of a spatial comparison. The natural variability of precipitation can affect the verification scores. Rain gauges underneath the Irene radar are sparse and irregularly spaced. Thus, interpolating the gauge observations will increase the uncertainty in the rain gauge data, which will be dependent on the particular weather event and spatial resolution. By doing a point comparison, the only uncertainty with the data remains with the gauges' physical measurement.

Contemporaneous pixels of precipitation were extracted for comparison with collocated gauges. Because radar measures precipitation within the atmosphere and not on the surface the extracted precipitation estimate needs to account for wind drift to be comparable to the rain gauge measurement. Thus, an average of 9x9 pixels over the corresponding gauge is used for the comparison. A series of continuous variable and dichotomous scores obtained through using a threshold were used to evaluate the precipitation algorithms. The TITAN algorithm using a single Marshall-Palmer Z-R relationship was used as a baseline score. The CRR and OFRR algorithms will be compared to the each other and the TITAN algorithm to illustrate any improvements.

A cylindrical region within 17 – 73 km from the radar was defined due to radar scan geometry effects, as discussed in section 4.4.1 on CAPPI level extraction. The region is illustrated by the grey rectangle in Figure 4-10. It allows for the direct comparison of all precipitation algorithms on all CAPPI levels. Figure 4-11 illustrates how the gauges, which are distributed around the radar within this region, will be used for the verification. In total the region includes 56 gauges, of which 15 are capable of 1 hour accumulation.

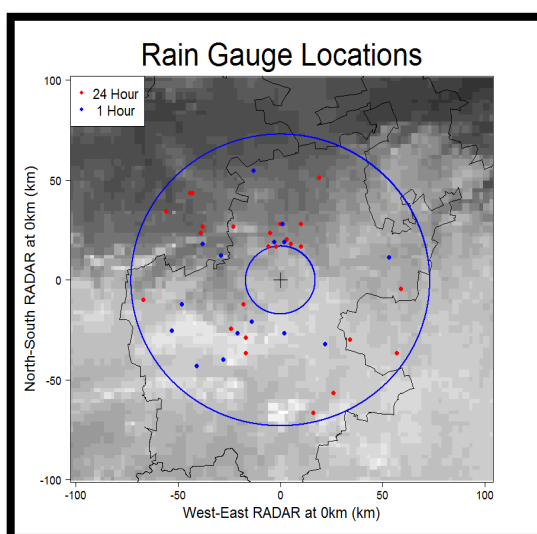


Figure 4- 11: Range gauges locations within 17 – 73 km range from radar where all CAPPI levels are comparable to the rain gauges.

How the different algorithms perform with respect to range from the radar also needs to be analysed. It is for this reason that the gauges have been divided into circular regions related to the range from the radar. An interval of 30km was selected because it allows for a reasonable amount of hourly and daily gauges to be included within each interval. Figure 4-12 illustrates the distribution of the gauges within each region.

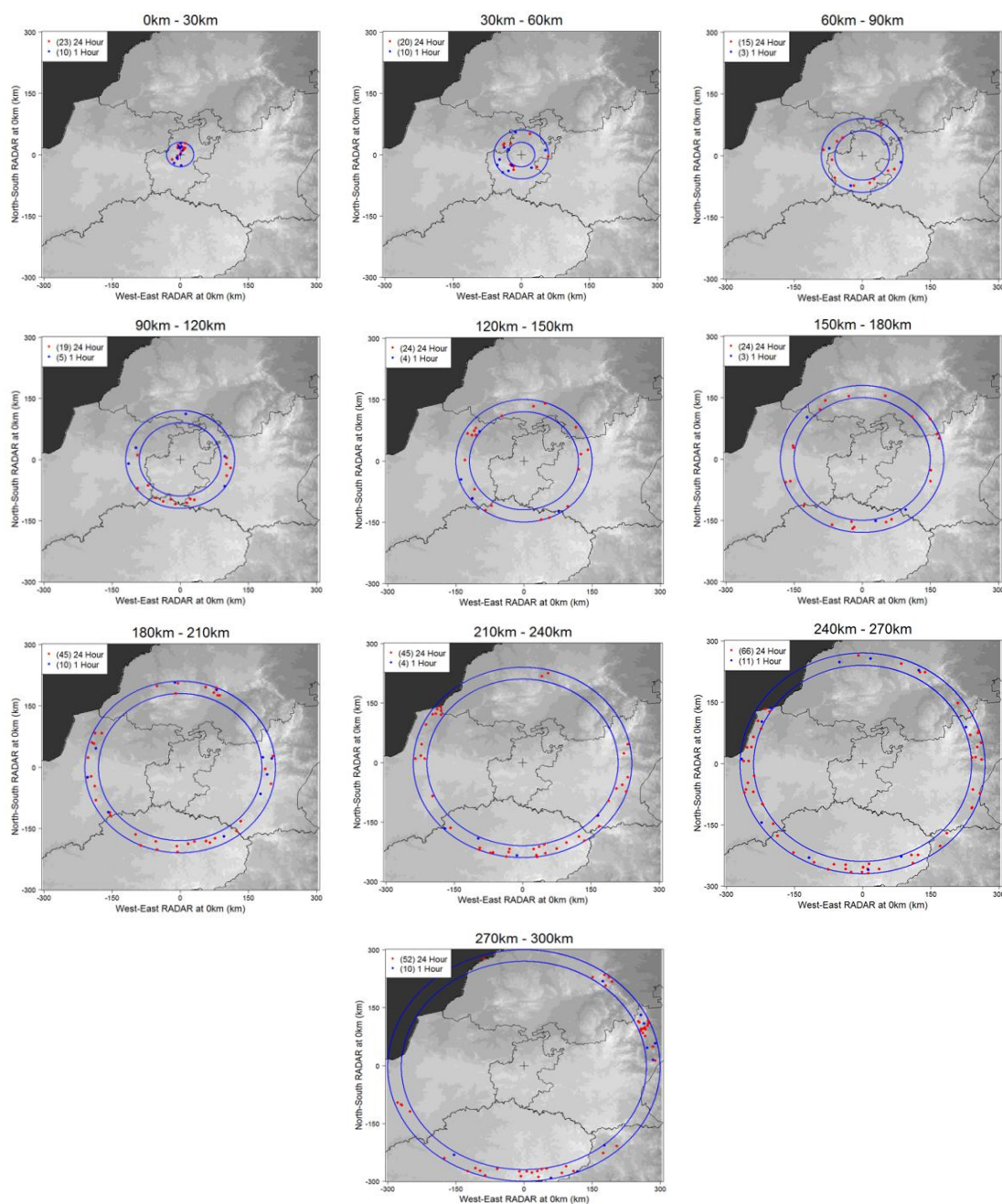


Figure 4- 12: A sequence of plots separated by a range interval of 30km. The plots illustrate the gauge distribution between each range interval. The number in parenthesis shows the number of each gauge type available

There is a reasonable distribution of gauges for each interval. However, large gaps do start to appear in the Northern and North-Western sectors when a range 210 km is reached. Continuous variable and dichotomous scores obtained through thresholds can be compared to determine the algorithms performance with range.

## 4.5.2 Evaluation Scores

This section discusses the evaluation scores using (i) continuous variable and (ii) dichotomous (yes/no) verifications. A brief overview will be given below discussing the advantage of the scores in terms of radar precipitation. The reader is referred to Stanski, et al. (1989) and Wilks (2005) for further details.

### *i. Continuous Variable Verification*

A good first look at the data and a simple way to visualize them is by drawing a scatter plot. The scatter plot will give a first indication of how well the radar estimates correspond to the observed values. A perfect representation of the data will be if the plot of data-points is located on the 45 degree diagonal of the scatter plot. A bias or a tendency for the radar to over or under estimate precipitation, from the observed values, will be indicated if the plotted values have a tendency to lie above or below the 45 degree diagonal. Scores like the correlation coefficient, Mean Error (BIAS) and root mean square error (RMSE) can be calculated to get a summary of the correspondence of the two sets of data. The correlation coefficient is calculated by,

$$r = \frac{\sum_i (E_i - \bar{E})(O_i - \bar{O})}{\sqrt{\sum_i (E_i - \bar{E})^2}} \quad (4-4)$$

where  $E$  is the radar estimate and  $O$  the observed gauge value and over-bars indicate means. The correlation coefficient measures the linear association of the data, i.e. it shows how well the radar estimates correspond to the observed values. A score as close to the perfect score of 1 is desirable. The correlation coefficient is sensitive to outliers in the data. Thus, it can easily be influenced by poor quality of gauge measurements so great care in quality control of the gauge data is required.

The Mean Error or additive BIAS is a good indicator of the average error within the dataset and is calculated by,

$$ME = \frac{1}{N} \sum_{i=1}^N (E_i - O_i) \quad (4-5)$$

where  $E$  and  $O$  is the same as Equation 4-4 and  $N$  is the total number of observations. The score indicates the direction of the error rather than the magnitude and a perfect score of 0 is sought-after. It is possible to get a good score if there are compensating errors.

The root mean squared error (RMSE) gives the average magnitude of the estimates error and a perfect score of 0 is desirable. The square law will put greater influence on large errors which is good when large errors are undesirable.

$$RMSE = \sqrt{\frac{1}{N} \sum_{i=1}^N (E_i - O_i)^2} \quad (4-6)$$

*ii. Dichotomous (yes/no) Verification*

Dichotomous verification is performed by constructing a contingency table through use of thresholds. Three thresholds were selected for comparison namely:

1. A 1 mm threshold,
2. A 5 mm threshold and,
3. A 10 mm threshold.

By evaluating yes, both radar and gauge received precipitation above the threshold; or no both are below the threshold, etc. The frequency of yes/no occurrences are constructed into a contingency like table format as displayed below in Figure 4-13.

		Observed	
		YES	NO
Estimates	YES	HITS	FALSE ALARMS
	NO	MISSES	CORRECT NEGATIVES

Figure 4-13: The format of a contingency table constructed by the use of thresholds.

A large variety of categorical statistics can be calculated from the elements in the contingency table to describe particular aspects of the different precipitation algorithms performance. One of the most common statistics to calculate is the accuracy (Equation 4-7).

$$Accuracy = \frac{hits + correct\ negatives}{total} \quad (4-7)$$

$$total = hits + false\ alarms + misses + correct\ negatives \quad (4-8)$$

The accuracy shows the overall percentage of estimates that were corresponding with the rain gauges. A perfect score will be 1, for 100% of cases. However, the score can be very misleading because it heavily influenced by correct negatives. Because the estimates and rain gauges are physical measurement of the atmosphere it is very easy for both measurements to return 0 mm of rainfall. For the majority of the study period there will be no rain over the gauges resulting in a high frequency of correct negatives. Thus, it will be expected that the accuracy scores will be high even if algorithms perform poorly.

The frequency BIAS (Equation 4-9) is another useful score to use. It measures how the frequency of the estimated "yes" events compare to the frequency of observed "yes" events, i.e. the score indicates whether the estimates has a tendency to under-forecast or over-forecast observed events. A perfect score is 1, while 0 and  $\infty$  show no skill. However, it does not measure how well the estimates correspond to the observations.

$$BIAS = \frac{hits + false\ alarms}{hits + misses} \quad (4-9)$$

The Probability of Detection (POD) and False Alarm Ratio (FAR) should be used in conjunction with one another, because both are very sensitive to the climatological frequency of their respective event. The POD indicates what percentage of the observed "yes" events were correctly estimated and the FAR indicates what percentage of estimated "yes" events actually did occur; i.e. using a 1 mm threshold the POD will give you the percentage of radar estimates that are more than 1 mm when the gauge measured more than 1 mm. The opposite is true for the FAR. For the POD in Equation 4-10 a perfect score is 1, while the FAR in Equation 4-11 a score of 0 is preferable.

$$POD = \frac{hits}{hits + misses} \quad (4-10)$$

$$FAR = \frac{\text{false alarms}}{\text{hits} + \text{false alarms}} \quad (4-11)$$

The Critical Success Index (CSI) illustrates how well the estimated “yes” event corresponded to the observed “yes” events. This is a particularly good score to use for precipitation because it ignores correct negatives. The CSI is only concerned with estimates that occurred and can thus be viewed as the accuracy of the estimates. It is heavily dependent on the climatological frequency of the hits and hits can occur purely due to random chance. By using the Equitable Thread Score (ETS) one can account and adjust for the hits that occur due to random chance. It is a good score to use when comparing different algorithms because it allows for the scores to be compared more fairly across different regimes. Both scores work on perfect score of 1.

$$CSI = \frac{\text{hits}}{\text{hits} + \text{misses} + \text{false alarms}} \quad (4-12)$$

$$ETS = \frac{\text{hits} - \text{hits}_{\text{random}}}{\text{hits} + \text{misses} + \text{false alarms} - \text{hits}_{\text{random}}} \quad (4-13)$$

$$\text{hits}_{\text{random}} = \frac{(\text{hits} + \text{misses})(\text{hits} + \text{false alarms})}{\text{total}} \quad (4-14)$$

The Heidke Skill Score (HSS) will illustrate the accuracy of the estimates relative to that of random chance. In meteorology it is better to measure the skill against climatology or persistence. Thus, the HSS measures the percentage of estimates that are correct after eliminating the estimates that would be correct due to climatology or persistence. The perfect score is 1 while 0 and below indicates no skill at all.

$$HSS = \frac{(\text{hits} + \text{correct negatives}) - (\text{expected correct})_{\text{random}}}{\text{total} - (\text{expected correct})_{\text{random}}} \quad (4-15)$$

$$\begin{aligned} & (\text{expected correct})_{\text{random}} = \\ & \frac{1}{\text{total}} \left[ (\text{hits} + \text{misses})(\text{hits} + \text{false alarms}) + \right. \\ & \left. (\text{correct negative} + \text{misses})(\text{correct negatives} + \text{false alarms}) \right] \quad (4-16) \end{aligned}$$

The results of the evaluation score will be presented in chapter 5

## 4.6 Summary

The rain gauges underneath the Irene radar domain have been extensively quality controlled. However, there may still be some problematic measurement as it is difficult to account for all the associated errors with the dataset. The S-band radar at Irene produces high quality reflectivity data that is free from RLAN interference and less effected by attenuation, particularly over short ranges from the radar. This is favourable for precipitation estimates. Ground clutter from the reflectivity data has been removed as well as possible by the Doppler filter. The reflectivity data was then converted into 3 precipitation algorithms:

1. The TITAN algorithm uses a single Z-R relationship and is calculated as described in section 4.4.3. This is the current operational algorithm at the national forecasting centre and will be used as the benchmark to compare improvements from the other algorithms.
2. The CRR, uses a dual Z-R relationship (section 4.4.2)
3. The OFRR, uses the dual Z-R relationship and motion vector morphing (section 4.4.2)

These algorithms are evaluated by comparing the estimated values to gauge measurements using a point verification technique. Continuous variable and dichotomous verifications scores provide sufficient framework to analyse the algorithms. The results will be presented in the next chapter. Section 5.2 will report the result from the classification algorithm, Section 5.3 will report the performance of the different algorithm and section 5.4 will report on the algorithm performance with range from the radar.

---

## CHAPTER 5

### ALGORITHM EVALUATION RESULTS

---

#### 5.1 Introduction

In this chapter the results of the verification scores introduced in Chapter 4 will be discussed. The classification scheme is to compare 5 minute rain rate values and Vertical Profiles of Reflectivity (VPR) to determine whether the classification scheme can accurately distinguish convective from stratiform precipitation. The TITAN algorithm is then evaluated using continuous variable and contingency table statistics as discussed in the previous chapter. The Classified Rain Rate (CRR) and Optical Flow Rain Rate (OFRR) on all CAPPI levels are then compared to the TITAN algorithm to determine if there is any improvement. Lastly the algorithms are evaluated in terms of range from the radar to estimate the overall performance of the algorithms.

#### 5.2 Results from Classification Scheme

The classification scheme was analysed using a selected event over the Gauteng area during the study period. The 15<sup>th</sup> and 16<sup>th</sup> of December 2010 were selected. The precipitation event cause localized flooding in parts of Gauteng and provided long durations of both convective and stratiform precipitation. A number of 5 minute rainfall station data were analysed within a 75 km radius of the radar to determine whether convective and stratiform rainfall occurred over the stations and whether the classification scheme can accurately distinguish between the two precipitation types. Figure 5-1 illustrates the 5 minute rain rate recorded by 2 of these rainfall stations namely Wonderboom Airport and Springs Automatic Rainfall Stations (ARS's). The graphs in Figure 5-1 show the recorded rain rate from 2010-12-15 00h00 to 2010-12-16 23h55 (SAST). The plotted line is a blue colour when the radar CAPPI classification scheme did not classify any rainfall, red when stratiform was classified and green when the classification scheme determined convective rainfall. Stratiform rain rate is associated with low rain rates for extended durations whereas convective rain rate tends to be at a much higher rain rate with shorter durations. At the Wonderboom Airport ARS a period of heavy convective precipitation is observed with frequent spikes in the rain rate which reach well over 40 mm/h. The classification scheme produced favourable results with the convective classified precipitation plotted as a green line. During the same time, the Springs ARS also recorded a spike in the rain rate reaching close to 40 mm/h, which is associated with the convection classified in the radar



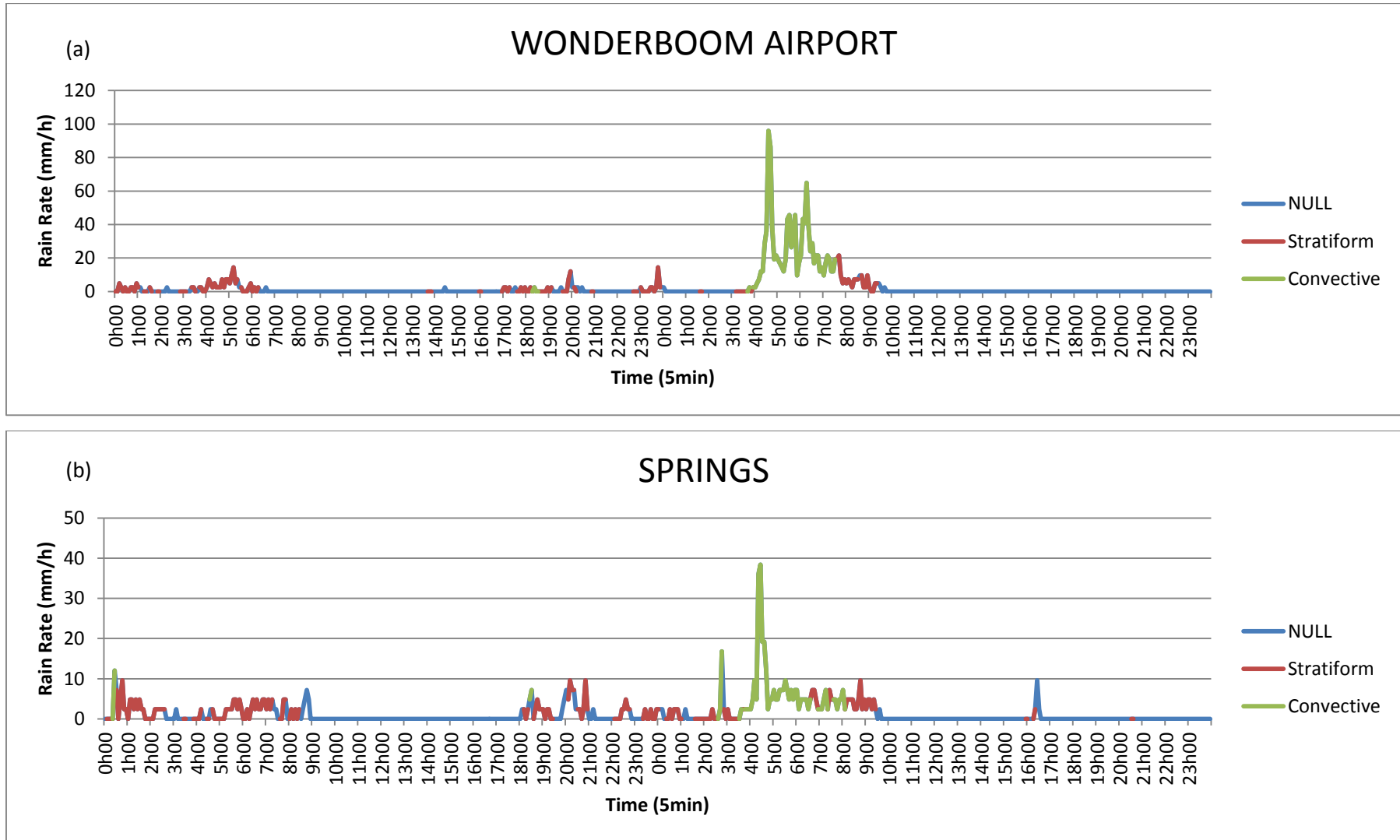


Figure 5-1: The 5 minute rain rate data recorded at the automatic rainfall stations of Wonderboom Airport (a) and Springs (b). The graphs show the recorded rain rate from the gauge for the period 2010-12-15 00h00 to 2010-12-16 23h55 (UTC). The traces are blue when the classification of the radar is null, red when classified as stratiform and green when the classification algorithm chose convective rainfall.

images. It is then followed by a steady rain rate of no more than 10 mm/h for a few hours, which is associated with stratiform precipitation. The convection is well identified by the classification scheme, evident from the green segments of the plotted line. However, the periods other than the convective segments comprise a mixture of null, convective and stratiform precipitation. Some further investigation is needed to determine if it is indeed stratiform or convective precipitation that occurred.

In order to accurately determine whether the radar is measuring convective or stratiform precipitation the radar Vertical Profile of Reflectivity (VPR) was extracted from the CAPPIS directly over the different rainfall stations. As discussed in Chapter 2, the bright band can easily be identified from the radar images of stratiform precipitation. Typically, an area of increased reflectivity would be observed on the VPR just below the freezing level. This feature is normally not present with convective precipitation due to the strong mixing of hydrometeors within the storm. Figure 5-2 illustrates the VPR calculated at the Wonderboom Airport ARS. Due to the fact that ARS data is in 5 minute intervals and the Radar scan strategy is running at 6 minute intervals the VPR needed to be averaged over an hourly period to match the gauge data. Thus, the corresponding pixel over the station was considered classified as convective when every vertical scan within the represented hour was classified as convective. The same is true for stratiform classified pixels. The VPR for each scan over the corresponding gauge was then extracted and averaged over the hour to be plotted as in Figure 5-2. The freezing level height was obtained from that closest matching time when radiosonde data was collected at the Irene WO. The freezing level height is also plotted (red line) on the graphs in Figure 5-2 for ease of comparison. The three graphs in Figure 5-2 were all classified as convective profiles because of the vertical structure of the reflectivity below the freezing level and because the reflectivity of the corresponding plotted VPR is near 40 dBZ. The time of the plots: 2010-12-16 0500, 2010-12-16 0600 and 2010-12-16 0700 correspond to the convective precipitation observed in Figure 5-1. Analysing the VPR for this time period in more detail, a typical convective profile was observed. High reflectivities below the freezing level were dominant and there is a steady drop with increasing height above the freezing level. This is due to more snow and ice hydrometeors being present within the atmosphere and the dielectric constant of ice results in lower reflectivities being observed. The analysis of the Wonderboom Airport VPRs show how well the classification scheme behaves.

Figure 5-3 is similar to Figure 5-2, except that these VPR's are located at the Springs ARS a day earlier than the plot in Figure 5-2 and they were classified as stratiform pixels. The corresponding time of 2010-12-15 0200, 2010-12-15 0600 and 2010-12-15 0700 were also defined as stratiform precipitation in Figure 5-1 which is early in the time series indicated by the

red line segment in the plot. Analysis of the VPR's shows a strong presence of the bright band. The sharp increase of reflectivity just below the freezing level, followed immediately below the peak by a sharp drop in reflectivity, is clear evidence of the bright band's presence.

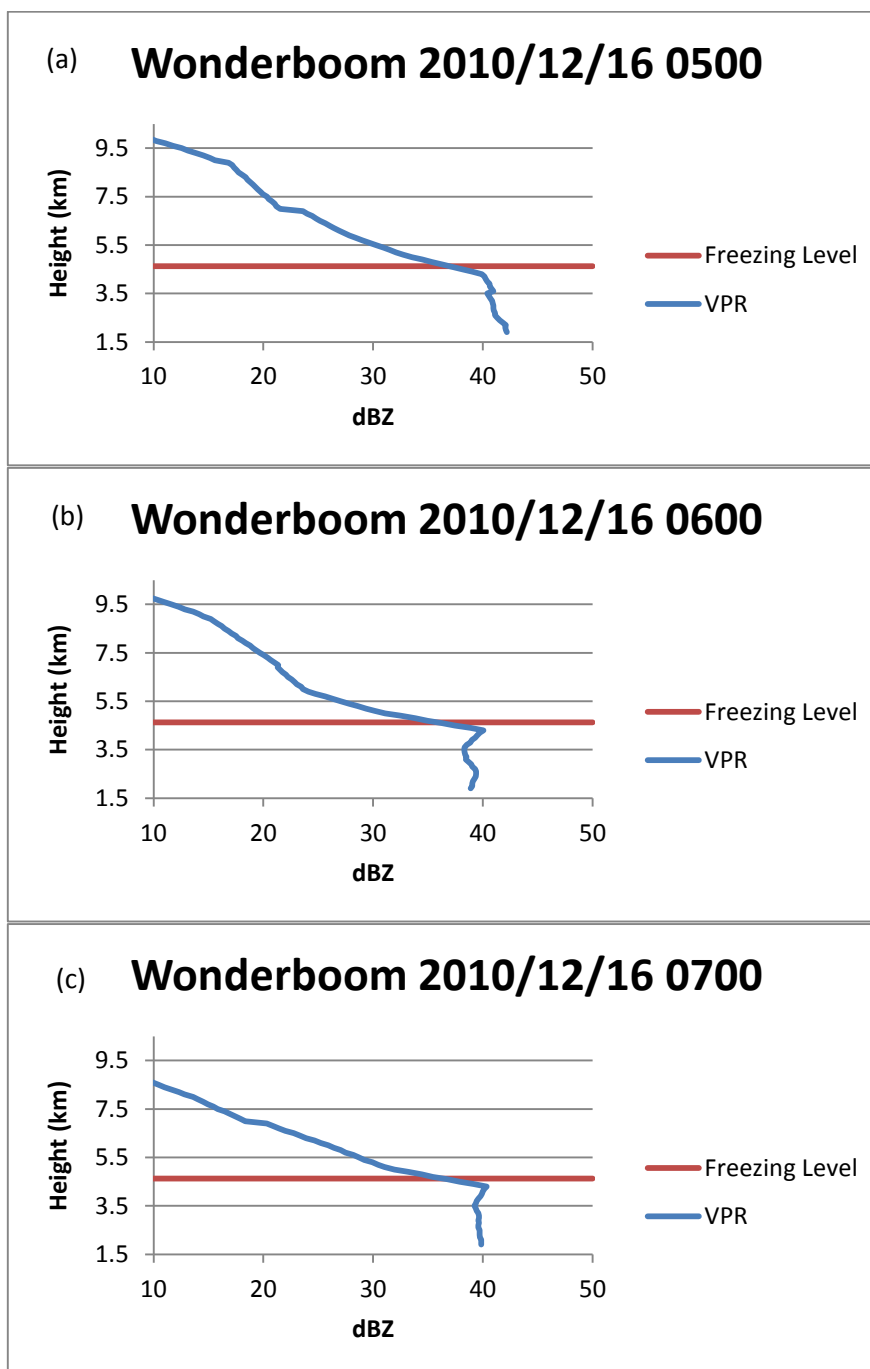


Figure 5-2: The average VPR for Wonderboom Airport. An hourly average of the VPR was calculated and plotted for each hour in which every radar scan above the pixel located at the station was classified as convective. The freezing level identified by the radiosonde launched from the Irene WO is also plotted (red line). The graphs are all classified as convective because of the vertical structure of the reflectivity below the freezing level where the reflectivity is near 40 dBZ. In the graphs (a), (b) and (c) the dates correspond to the title.

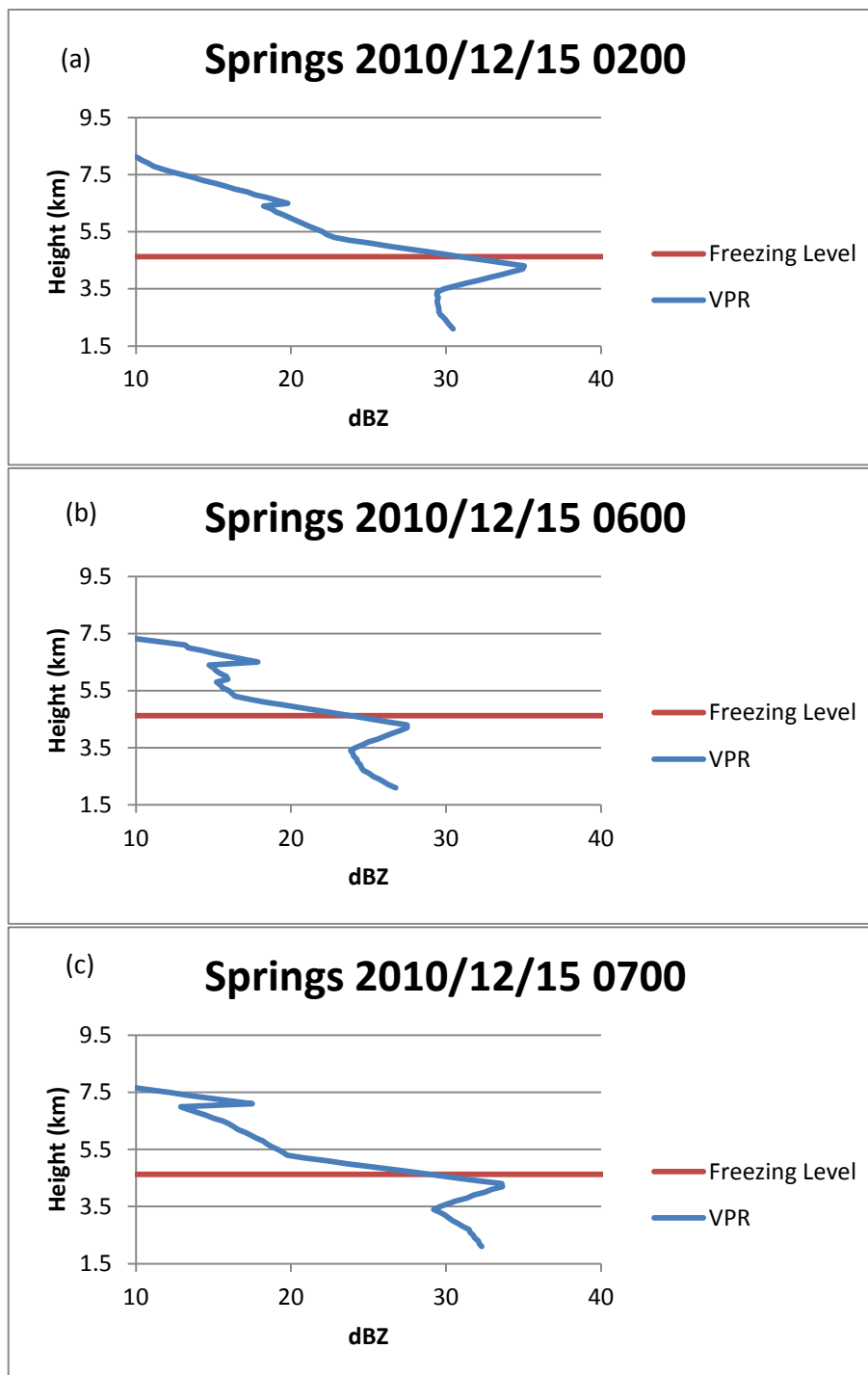


Figure 5-3: The average VPR for Springs ARS. An hourly average of the VPR was calculated and plotted for each hour where every radar scan within the hour, the corresponding pixel located at the station, was classified as stratiform. The freezing level from the radiosonde balloon ascent data launched from Irene WO is also plotted (red line). The graphs are all classified as stratiform. In the graphs (a), (b) and (c) the dates correspond to the title.

This confirms the classification of the column of stratiform precipitation above the Springs station. Thus, the classification scheme successfully classified the stratiform precipitation as shown in Figure 5-1.

Figure 5-4 illustrates the VPR's for the Springs ARS that represents the area of convective classified precipitation first identified analysing Figure 5-1. Both the graphs were classified as convective. Analysing the first panel of Figure 5-4 which is the average profile during the hour 2010-12-16 0500, a typical convective profile is observed. There is no sharp increase in reflectivity below the freezing level, so there seems to be no evidence of a bright-band occurring;

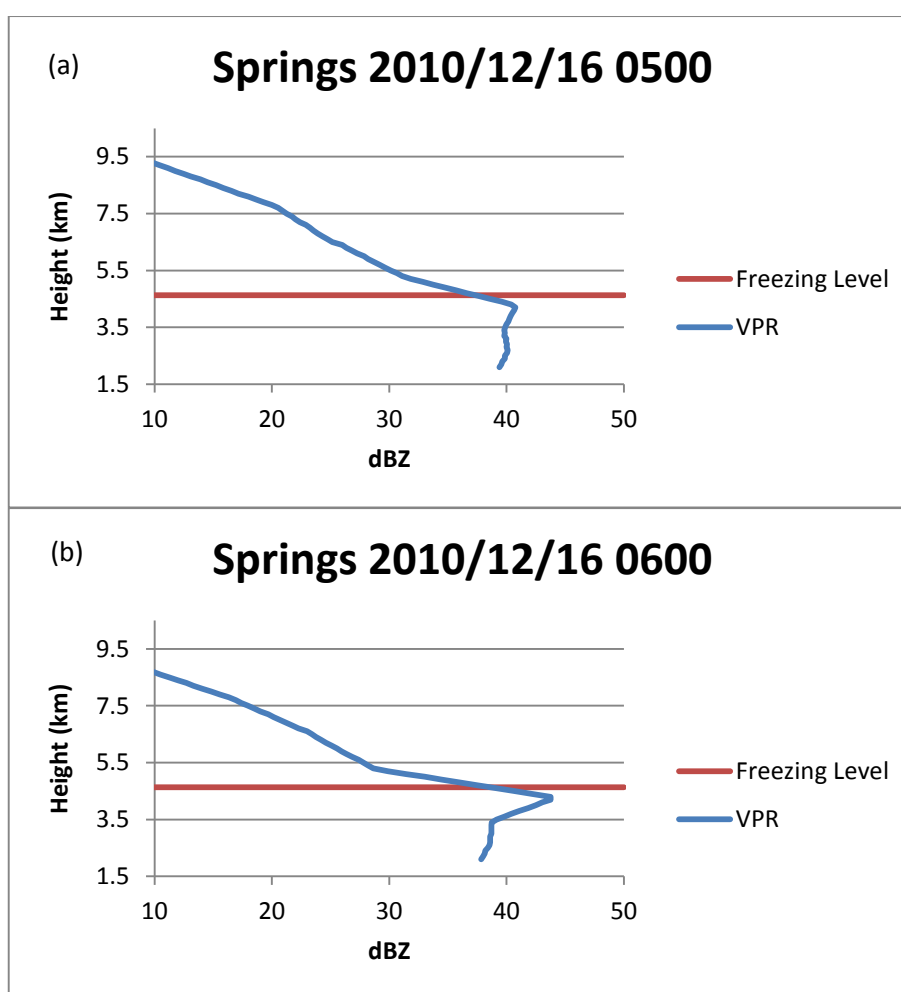


Figure 5-4: The average VPR for Springs ARS. An hourly average of the VPR was calculated and plotted for each hour where every radar scan within the hour, the corresponding pixel located at the station, was classified as convective. The freezing level from the balloon ascent data done at Irene WO is also plotted (red line). The graphs are both classified as convective. In the graphs (a) and (b) the dates correspond to the title.

in addition the reflectivity is about 40 dBZ. It is safe to classify this profile as convective precipitation. This corresponds well with Figure 5-1 where a sharp spike in rain rate is observed at the same time.

The lower panel in Figure 5-4 was also classified as convective. However, after analysis a local peak of reflectivity was observed below the freezing level, below which the reflectivity drops to about 38 dBZ. Thus, the presence of the well-definite bright band signifies stratiform rainfall. This conclusion is supported by the lower rain rates in Figure 5-1 at the corresponding time. Thus, the classification scheme did not accurately classify the stratiform precipitation in this case, probably because the reflectivity of the bright band peaks as 45 dBZ.

This conclusion was confirmed when analysing other rainfall stations with their corresponding VPR's over the same period. It would seem that the classification scheme works well in identifying stratiform and convective regions. However, it seems to struggle in distinguishing between the two classifications when a region of stratiform precipitation follows a convective front. The classification scheme then tends to over-compensate by choosing convective pixels.

### **5.3 Algorithm Comparison**

The following subsections will discuss the results from the verification scores calculated from gauges within the 17 – 73 km cylinder as defined in Chapter 4. The scores will be compared to determine whether the CRR and OFRR algorithm outperforms the TITAN algorithm.

#### **5.3.1 TITAN as a Benchmark**

The TITAN algorithm was chosen to be the benchmark against which to measure any improvements coming from the CRR and OFRR algorithms. Figures 5-5 (a) and 5-5 (b) illustrate the scatterplots for the hourly and daily measurements respectively as measured by the TITAN algorithm. The blue dashed line represents the linear fit, while the black line represents a perfect fit of Radar to Gauge rainfall. The hourly trend-line through the data in Figure 5-5 (a) has a gradient of 0.97 which is very close to the ideal gradient of 1. This indicates that the radar estimates have a slight tendency to under-estimate the precipitation as the magnitude of the measurements increases. The trend-line has an intercept of 0.21 mm, which illustrates that the radar estimates are more likely to indicate rainfall whenever a gauge measures zero. The correlation of 0.792 is respectable, even though there is a fair amount of scatter. A similar pattern is observed with the daily measurements. The values for the linear fit are worse than the hourly, possibly due to the longer accumulation period. A gradient of 0.78 shows a greater

tendency to underestimate larger measurements, while the intercept of 5.65 mm illustrates that the radar estimates are very likely to measure precipitation when the gauges are recording zero rainfall. This can be due to error from rain gauge measurements as a result of mechanical malfunction or human error when the measurements are recorded, as well as radar estimates that measures precipitation as a result from non-precipitating reflectivities such as anomalous propagation, clutter, etc. The correlation value of 0.682 indicates mediocre linkage between the sets of data. Although every attempt has been made to remove the errors from the dataset, it is difficult to remove every contaminated measurement.

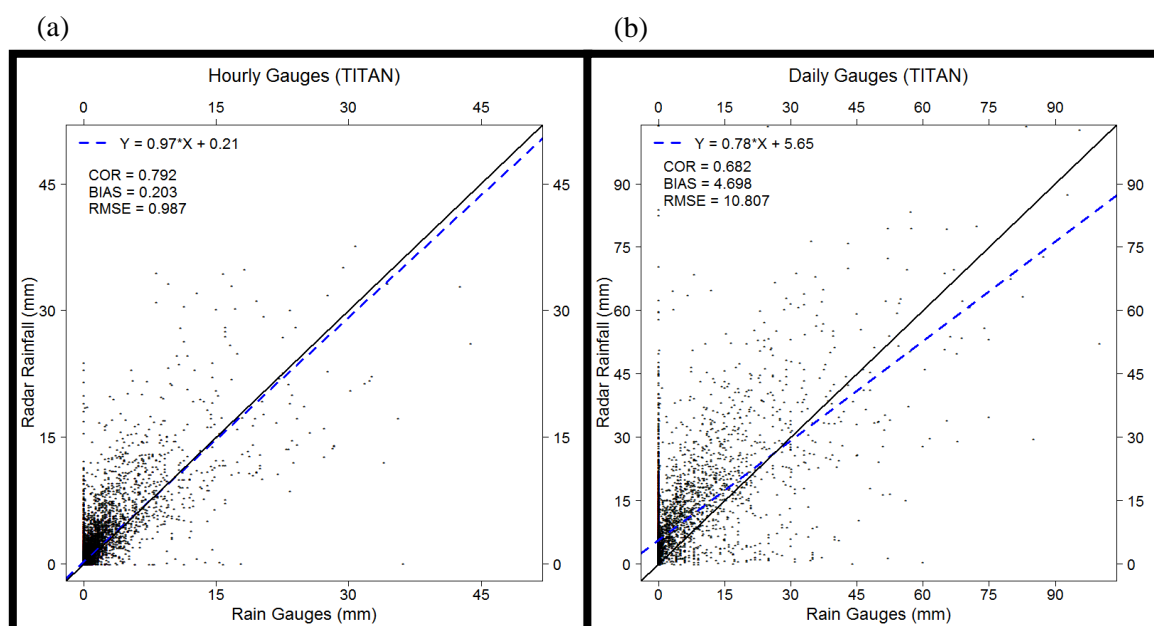


Figure 5-5: Scatterplot for the hourly (a) and daily (b) radar and contemporaneous gauge measurements for the whole study period October 2010 to March 2011. The blue dashed line represents the linear fit, while the black line represents a perfect fit of  $y=x$ . The associated correlation, bias and RMSE for the entire study period are also shown.

The correlation coefficients for hourly and daily accumulations are illustrated in Figure 5-6 (a) from October 2010 to March 2011. The radar precipitation estimates correlate reasonably well with the gauge measurements. With the hourly measurements, most of the individual months have a correlation value of around  $\pm 0.8$ , with January the only month that deviates and drops down to 0.72. This reduces the correlation coefficient for the study period to below 0.8, as shown in Figure 5-5 (a). The daily measurements show a high correlation of 0.78 during October and drops down to 0.59 for November. The remainder of the period then illustrates a correlation coefficient of close to 0.68, which is the correlation coefficient for the whole 6 month period, as shown in Figure 5.5.

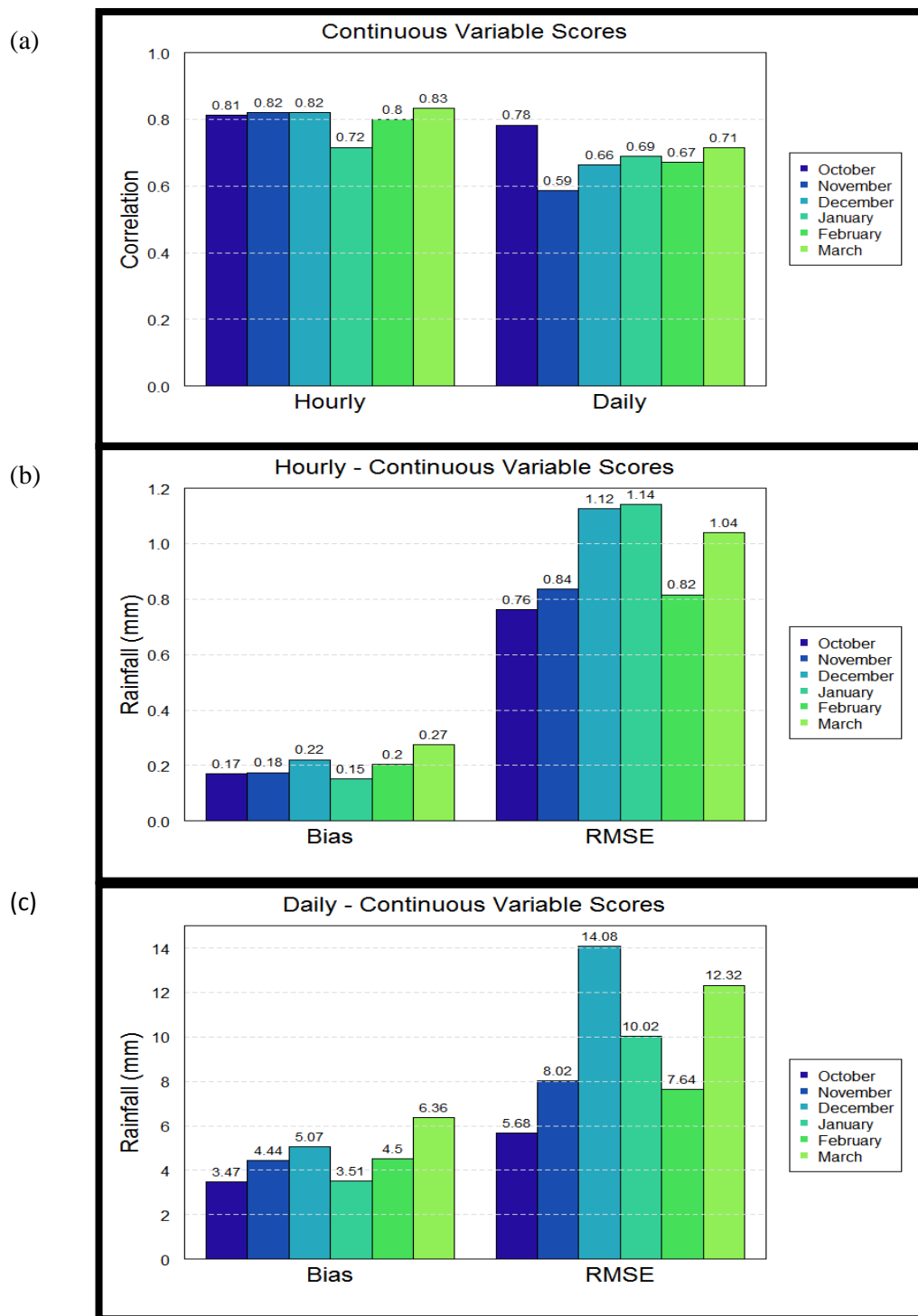


Figure 5-6: Continuous variable scores on a monthly basis for the October 2010 – March 2011 study period are illustrated. The correlation coefficient (a) for hourly and daily measurements is shown. The BIAS and Root Mean Square Error (RMSE) for one hour accumulations (b) as well as daily accumulations (c) are shown. The blue to green bars represents the changes through each month.



The BIAS scores are similarly illustrated in Figure 5-6 (b) and 5-6 (c) for both hourly and daily accumulation periods respectively. Positive values are observed for every individual month, which indicates an over-estimation by the TITAN algorithm for both accumulation periods. A similar pattern is observed for both hourly and daily measurements. October and January illustrates the best scores, followed by November and February. December and March thus shows the highest BIAS scores for the period. The month of January does illustrate the best BIAS score, contradiction the lower correlation value. However, good BIAS scores can be obtained through compensating errors.

The RMSE is also illustrated in Figure 5-6 (b) and (c), which are the hourly and daily measurements respectively. The hourly measurements have an error of 0.76 – 1.14 mm, with December, January and March having an error of about 1 mm and October, November and February illustrating errors of around 0.8 mm. This pattern is also observed with the daily measurements. December, January and March have errors from 10.02 -14.08 mm while October, November and February have errors 5.68 – 8.02 mm. December, January and March are also the months that illustrated above normal rainfall (Figure 4-2, in chapter 4), while October, November and February received below normal rainfall. Thus, the decrease in errors can be related to the amount of precipitation received during the particular observation period. This is due to the higher probability that both instruments will record zero rainfall whenever there is no rainfall present.

Table 5-1 illustrates contingency table and dichotomous (yes/no) evaluated scores using thresholds of 1 mm, 5 mm and 10 mm for the hourly measurements. Table 5-1 (a) illustrates the number of events where the gauge and radar measured both score more than 1 mm (hits) , both less than 1 mm (correct negatives), the radar more than 1mm while the gauge less than 1 mm (false alarms) and the gauge more than 1 mm and the radar less (missed events). Tables 5-1 (b) and (c) are similar tables, but are using 5 mm and 10 mm respectively as the measurement thresholds. Table 5-1 (d) lists the scores calculated from Tables 5-1 (a), (b) and (c). The accuracy scores illustrate near perfect scores of 1, with the 10 mm threshold performing the best with a score of 0.995, followed by the 5mm threshold with 0.990 and then the 1 mm threshold with 0.973. This score is somewhat misleading due to the fact that it only takes hits and correct negative events into consideration. During the rainfall period it is far more likely that the gauge and radar will measure precipitation below the specified threshold, as shown by the contingency tables in Table 5-1 (a), (b) and (c). Thus, to get a true sense of the performance of the algorithm, one must refer to the Critical Success Index (CSI). The CSI score includes the false alarms and missed events while ignoring the correct negatives. It is clear that the 1 mm threshold performs

the best with 0.539, followed by the 5 mm threshold with 0.453 and then the 10mm threshold with 0.357.

Table 5- 1: Contingency tables for hourly measurements are illustrated using 1 mm (a), 5 mm (b) and 10 mm (c) as thresholds. Scores calculated from the resulting tables are illustrated in (d).

(a)			(b)			(c)		
ESTIMATE	OBSERVED		ESTIMATE	OBSERVED		ESTIMATE	OBSERVED	
	$\geq 1$	$< 1$		$\geq 5$	$< 5$		$\geq 10$	$< 10$
$\geq 1$	1579	1196	$\geq 5$	414	425	$\geq 10$	134	191
$< 1$	155	47885	$< 5$	74	49902	$< 10$	50	50440

	Scores (1mm)	Scores (5mm)	Scores (10mm)
<b>Accuracy</b>	0.973	0.99	0.995
<b>Bias</b>	1.6	1.719	1.766
<b>Probability of Detection</b>	0.911	0.848	0.728
<b>False Alarm Ratio</b>	0.431	0.507	0.588
<b>Critical Success Index</b>	0.539	0.453	0.357
<b>Equitable Thread Score</b>	0.524	0.449	0.355
<b>Heidke Skill Score</b>	0.687	0.619	0.524

The Equitable Thread Score (ETS) is similar to the CSI but it compensates for the possibility of scoring hits in the contingency table due to random chance. The ETS illustrate scores slightly less than the CSI (decrease by less than 1%), but indicates similar results overall. The frequency bias scores show values higher than 1. This indicates an over-estimation, meaning that the radar is far more likely to estimate amounts above the threshold than what the gauge is measuring. The smallest bias is observed at the 1 mm threshold and then increases with an increase in threshold. The Probability of Detection (POD) and False Alarm Ratio (FAR) need to be compared alongside one another. With the high over-estimation, high POD and FAR scores are observed. A decreasing POD and increasing FAR is observed with an increase in threshold. The Heidke Skill Score (HSS) also indicates a decrease in value with an increase in threshold.

Table 5-2 follows the same layout as Table 5-1. It illustrates the contingency tables for the daily gauge and radar estimates also with thresholds of 1 mm, 5 mm and 10 mm. For the 1

mm threshold the accuracy is below 50% with 0.439. The scores increase with increasing threshold with the 5 mm threshold and 10 mm threshold scoring 0.743 and 0.821 respectively.

Table 5-2: Contingency tables for daily measurements are illustrated using 1 mm (a), 5 mm (b) and 10 mm (c) as thresholds. Scores calculated from the resulting tables are illustrated in (d).

(a)			(b)			(c)		
ESTIMATE	OBSERVED		ESTIMATE	OBSERVED		ESTIMATE	OBSERVED	
	$\geq 1$	$< 1$		$\geq 5$	$< 5$		$\geq 10$	$< 10$
$\geq 1$	1547	2813	$\geq 5$	982	1179	$\geq 10$	609	799
$< 1$	34	681	$< 5$	123	2791	$< 10$	108	3559

(d)			
	Scores (1mm)	Scores (5mm)	Scores (10mm)
<b>Accuracy</b>	0.439	0.743	0.821
<b>Bias</b>	2.758	1.956	1.964
<b>Probability of Detection</b>	0.978	0.889	0.849
<b>False Alarm Ratio</b>	0.645	0.546	0.567
<b>Critical Success Index</b>	0.352	0.43	0.402
<b>Equitable Threat Score</b>	0.062	0.282	0.311
<b>Heidke Skill Score</b>	0.117	0.44	0.475

This is due to the likelihood of scoring correct negatives with increasing threshold values. Taking the CSI into consideration, very low scores are evident. The highest being the 5 mm threshold at 0.43. With the ETS taking persistence into account, it reveals very low scores and an increase in accuracy with increase in threshold. The bias scores indicate heavy over-estimation with the 1 mm threshold, with the 5 mm scoring slightly less than the 10 mm threshold. The 1 mm threshold has a very high POD of 0.978. However, the FAR is also high at 0.645 supporting the heavy over-estimation illustrated by the bias. When considering both POD and FAR the 5 mm threshold scores the best. The HSS indicates an increase in skill with increase in threshold the 1 mm threshold has almost no skill at 0.117 for daily measurements.

Figure 5-7 compares cumulative plots and frequency distributions of the hourly and daily radar and gauge data during the study period. In the individual images, the blue and red line represents the gauges and radar estimates respectively. Figure 5-7 (a) illustrates the hourly measurements while Figure 5-7 (b) the daily measurements. The top graph in each panel

illustrates the average cumulative sum of the radar estimates and gauge measurements. The bottom graph illustrates the Cumulative Distribution Function (CDF) for the study period considering only non-zero precipitation events. Thus, the CDFs reflect the probability of a specific value occurring whenever precipitation occurs. With both the hourly and daily measurements (Figure 5-7 (a) and (b)) the radar estimates illustrate a much more rapid growth than the gauge measurements and continue to deviate from each other as time progress. The hourly gauges recorded an average total of 673 mm during the study period and the radar estimated an average of 1255 mm, almost twice the amount of the gauges. Similarly, the daily gauges measured a total of 665 mm with the radar coming in at 1414 mm, more than twice the amount of the gauges. This confirms the over-estimation bias score and clearly shows that the greater the accumulation the larger the error will be. The region used for verification contains 16 hourly gauges while the daily gauges have a total of 42. The hourly measurements CDF graph in Figure 5-7 (a) illustrate that the probability of a specific precipitation value of occurring is always greater for the radar estimates than the gauge measurements. The daily measurements CDF graph in Figure 5-7 (b) show that the gauge estimates have a higher probability of occurring than the radar estimates. Only for the smaller precipitation measurements past the 2.0 mm measurement the probability of the radar estimate drastically increase.

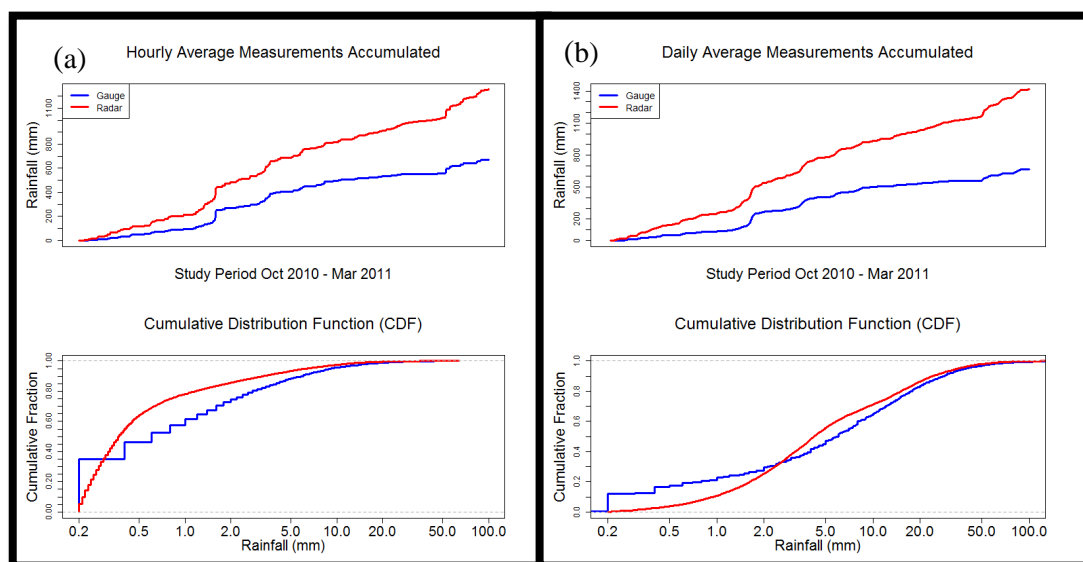


Figure 5-7: Gauge (blue) and radar (red) hourly accumulation (a) and daily accumulation (b) for the study period of October 2010 – March 2011. The associated Cumulative Distribution Function (CDF) considering only measurement that are not zero, are also illustrated in the lower panels, in which the cumulative fraction ranges from 0 to 1 and the horizontal axes are logarithmic scales.

### 5.3.2 Visual Comparison of Algorithms

Figure 5-8 illustrates 4 examples where the 3 algorithms (TITAN, CRR and OFRR) hourly accumulations are compared. The rows within the figure represent each algorithm with the TITAN algorithm at the top, CRR in the centre and OFRR at the bottom. Each column is an event and time stamps are valid for the end of the accumulated period. The dates and time for the events are (from left to right) 2010-10-24 15h00, 2010-10-28 00h00, 2010-12-03 02h00 and 2010-12-15 23h00 respectively. The 3.0 km CAPPI was selected to represent the CRR and OFRR algorithms.

The first case relating to 2010-10-24 15h00 the CRR algorithm captures the convective core on the border of the precipitation field at the north east and south East corners. A higher rain rate is illustrated with the CRR algorithm than the TITAN algorithm. The convective storms to the North and East of Pretoria (indicated by PTA in the images within Figure 5-8) also indicate higher rain rates. This is due to the deep convective Z-R relationship ( $300R^{1.4}$ ) used by the CRR algorithm. The TITAN and CRR algorithms show a speckled pattern clearly visible within the storm paths mentioned above. The OFRR algorithm smooth's the pattern considerably, but the storms just south and north of Pretoria still has a speckled pattern with the higher rain rates.

The lower rain rates values appear to have a much better response to the smoothing technique. However, this is not the case everywhere within the precipitation field, as the storm to the east of Pretoria shows some favourable results with the smoothing technique within the OFRR algorithm. The next accumulation which ends at 2010-10-28 00h00 the CRR show a slight increase in rain rate with the convective storm north of Pretoria. A speckled pattern is visible with the storm to the North of Pretoria within both the TITAN and CRR algorithms. The OFRR algorithm smoothed this pattern considerably to represent a much more realistic pattern for the precipitation. The accumulation of 2010-12-03 02h00 the CRR algorithm show a slight decrease in rain rate for the immediate area around the radar. This is as a result of using a single CAPPI, as both algorithms use Marshall-Palmer for stratiform rain rate.

Accumulated storms to the north of Pretoria and east of Johannesburg show a speckled pattern as a result of the radar temporal resolution. The OFRR algorithm does well to smooth out this pattern to give a more realistic result. The final accumulation in the figure, 2010-12-15 23h00 is a large event that moved very slowly and caused significant flooding over parts of Gauteng. By comparing TITAN and CRR a significant difference in the precipitation patterns are observed. Bright-band interference is mostly eliminated by the use of the CAPPI. Thus, the ring like features around the radar in the TITAN field is reduced. Small variations in the precipitation field, predominately where there is convection, are observed.

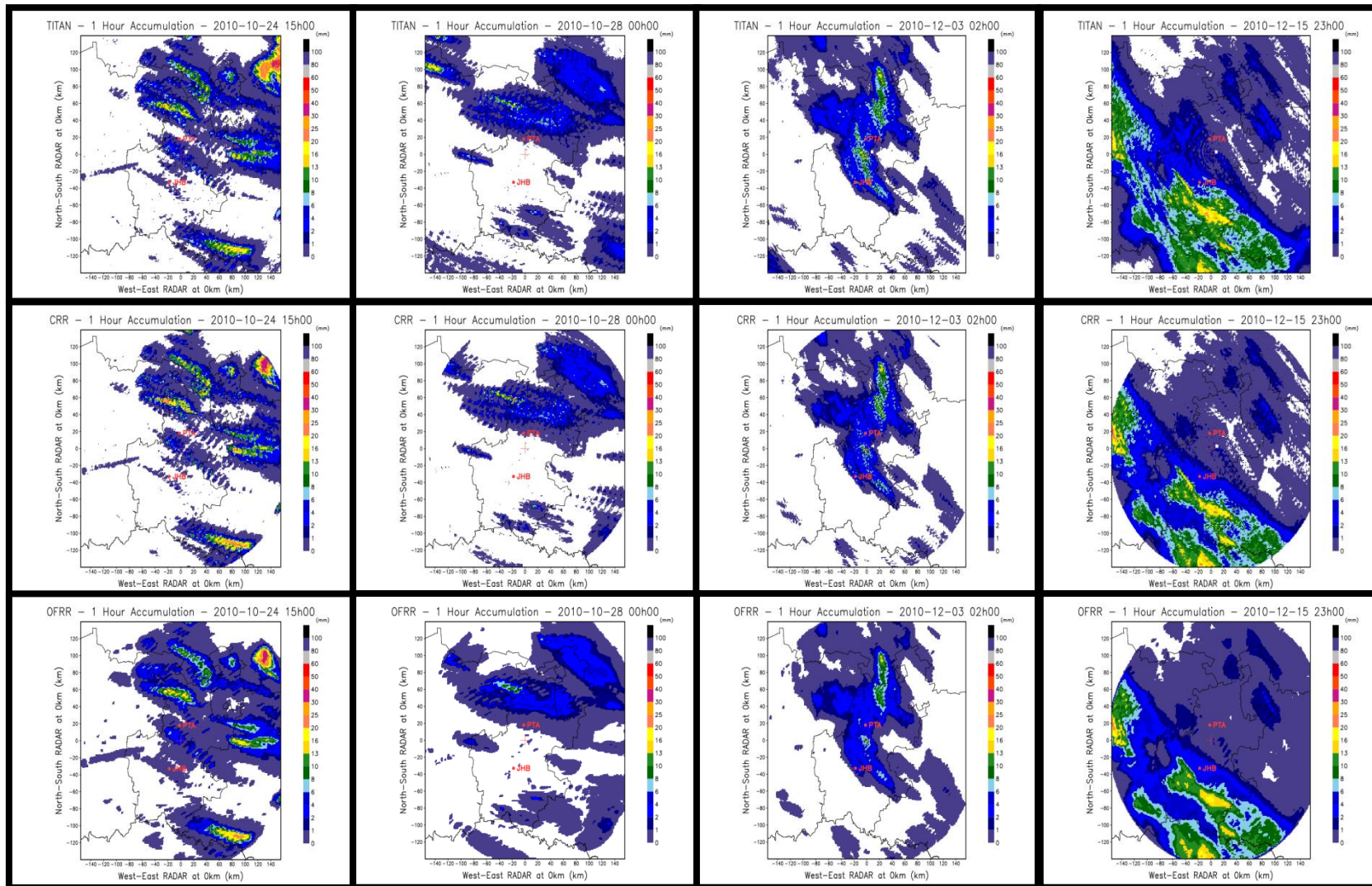


Figure 5-8: Examples of the 3 algorithms (TITAN, CRR and OFRR) hourly accumulations. The rows represent each algorithm with the TITAN algorithm at the top, CRR in the centre and OFRR at the bottom. Each column is an event and time stamps are valid for the end of the accumulated period. The 3.0km CAPPI was selected to represent the CRR and OFRR algorithms.



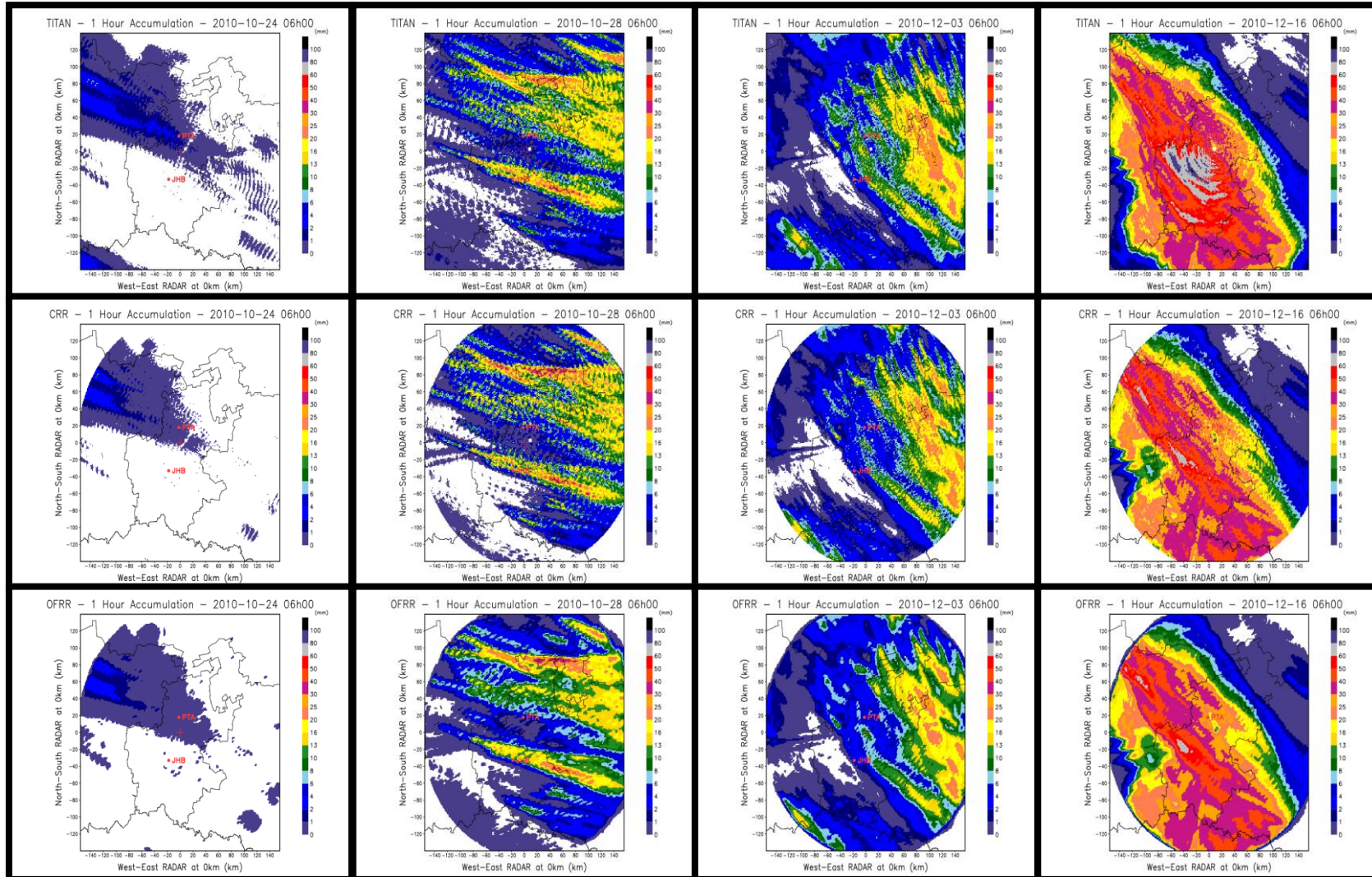


Figure 5- 9: Examples of the 3 algorithms (TITAN, CRR and OFRR) daily accumulations. The rows represent each algorithm with the TITAN algorithm at the top, CRR in the centre and OFRR at the bottom. Each column is an event and time stamps are valid for the end of the accumulated period. The 3.0km CAPPI was selected to represent the CRR and OFRR algorithms

The regions of higher precipitation to the west and south of the radar right at the edge of the coverage area showing a slight increase in precipitation due to the deep convective ZR relationship. The OFRR algorithm illustrates a much smoother precipitation field with a lot of the speckle removed, especially at the edges of the precipitation field.

Figure 5-9 illustrates 4 examples where 24 hour accumulations for 3 algorithms (TITAN, CRR and OFRR) are compared. The layout is similar to Figure 5-8. Each column is an event and time stamps are valid for the end of the accumulated period. Thus, accumulations are for 2010-10-23, 2010-10-27, 2010-12-02 and 2010-12-15 respectively. The 3.0 km CAPPI was selected to represent the CRR and OFRR algorithms. For the daily accumulation on 2010-10-23 the TITAN algorithm exhibited much higher precipitation values than the CRR or OFRR algorithm.

The use of a CAPPI level seems to have excluded the additional precipitation. The OFRR illustrates a precipitation field, which nicely smoothed the CRR field especially around the edges of the accumulated field. The accumulation on 2010-10-27 illustrates fast moving thunderstorms. Thus, speckled lines of precipitation are visible on both the TITAN and CRR algorithms. Slightly higher precipitation rate is captured by the CRR algorithm due to the deep convective Z-R relationship. The OFRR algorithm manages to smooth out most of the noise caused by the temporal resolution of the scan strategy. However, it is not completely removed. The CRR for the 2010-12-02 accumulation illustrated a reduced precipitation amount compared to the TITAN algorithm. Again, this is the result from using the single CAPPI level for precipitation calculations.

The noise from the CRR field shows a very speckled pattern. This pattern is then nicely smoothed within the OFRR precipitation field. Similar results are observed for the 2010-12-15 case where the field has been smoothed, removing a lot of the speckled pattern observed in the CRR and TITAN algorithms. Once again, the use of a single CAPPI has resulted in significant reduction in the amount of precipitation captured by the TITAN algorithm. The TITAN algorithm captures the effect of bright-band interference. The CAPPI level at 3km is still well below the freezing level and thus show minimal effects related to the interference.

### **5.3.3 Results of Verification Scores**

The correlation coefficients between the 2 precipitation algorithms and rain gauges for each CAPPI level are listed in Table 5-3 and Table 5-4 for the hourly and daily accumulations respectively. Both tables follow similar layouts with the TITAN scores discussed in section 5.3.1 also added for comparison.



Table 5-3: Correlation coefficient scores for hourly measurements of the CRR and OFRR algorithms at the respective CAPPI levels. The TITAN algorithm is include for reference and the CAPPI level SURFACE represents the vertical column of reflectivities being projected to the surface for calculations.

	Algorithm	CAPPI	PERIOD	OCT	NOV	DEC	JAN	FEB	MAR
1	TITAN	SURFACE	0.792	0.813	0.821	0.821	0.716	0.800	0.834
2	CRR	2.5	0.752	0.807	0.828	0.776	0.720	0.752	0.770
3	OFRR	2.5	0.743	0.815	0.804	0.771	0.702	0.763	0.747
4	CRR	3.0	0.751	0.779	0.829	0.780	0.708	0.752	0.774
5	OFRR	3.0	0.744	0.793	0.812	0.776	0.696	0.761	0.750
6	CRR	3.5	0.747	0.771	0.806	0.778	0.678	0.736	0.790
7	OFRR	3.5	0.740	0.791	0.795	0.775	0.668	0.745	0.768
8	CRR	4.5	0.726	0.736	0.818	0.764	0.600	0.681	0.791
9	OFRR	4.5	0.723	0.748	0.812	0.775	0.594	0.694	0.769
10	CRR	5.5	0.616	0.665	0.706	0.585	0.533	0.620	0.720
11	OFRR	5.5	0.611	0.692	0.687	0.590	0.510	0.634	0.705
12	CRR	7.0	0.482	0.574	0.533	0.471	0.399	0.553	0.585
13	OFRR	7.0	0.475	0.623	0.504	0.462	0.363	0.560	0.581
14	CRR	8.5	0.369	0.465	0.369	0.397	0.307	0.434	0.478
15	OFRR	8.5	0.355	0.499	0.329	0.361	0.260	0.464	0.493
16	CRR	10.0	0.304	0.515	0.294	0.302	0.226	0.322	0.481
17	OFRR	10.0	0.284	0.438	0.278	0.284	0.203	0.359	0.469

Table 5-4: Correlation coefficient scores for daily measurements of the CRR and OFRR algorithms at the respective CAPPI levels. The TITAN algorithm is include for reference and the CAPPI level SURFACE represents the vertical column of reflectivities being projected to the surface for calculations.

	Algorithm	CAPPI	PERIOD	OCT	NOV	DEC	JAN	FEB	MAR
1	TITAN	SURFACE	0.682	0.783	0.586	0.664	0.689	0.671	0.714
2	CRR	2.5	0.678	0.791	0.635	0.662	0.726	0.666	0.680
3	OFRR	2.5	0.678	0.760	0.633	0.669	0.726	0.664	0.669
4	CRR	3.0	0.666	0.779	0.630	0.637	0.713	0.667	0.682
5	OFRR	3.0	0.669	0.750	0.628	0.651	0.715	0.666	0.674
6	CRR	3.5	0.653	0.774	0.625	0.613	0.686	0.648	0.695
7	OFRR	3.5	0.657	0.737	0.618	0.629	0.689	0.647	0.687
8	CRR	4.5	0.649	0.760	0.587	0.649	0.623	0.637	0.669
9	OFRR	4.5	0.660	0.722	0.611	0.666	0.640	0.634	0.668
10	CRR	5.5	0.508	0.742	0.481	0.413	0.583	0.591	0.588
11	OFRR	5.5	0.518	0.695	0.507	0.428	0.584	0.584	0.597
12	CRR	7.0	0.397	0.656	0.370	0.306	0.451	0.515	0.555
13	OFRR	7.0	0.402	0.613	0.400	0.308	0.441	0.506	0.562
14	CRR	8.5	0.305	0.512	0.302	0.231	0.370	0.437	0.503
15	OFRR	8.5	0.308	0.480	0.310	0.228	0.351	0.430	0.515
16	CRR	10.0	0.211	0.368	0.262	0.146	0.303	0.358	0.430
17	OFRR	10.0	0.217	0.356	0.264	0.145	0.289	0.347	0.438

The table cells are coloured according to their corresponding values. The first column that represents correlation scores is labelled PERIOD and corresponds to the entire 6 month study period. The rest of the columns are a breakdown of the of the study period in months ranging from October 2010 to March 2011.

Considering Table 5-3 and the whole study period, the TITAN algorithm has the highest correlation of 0.792 with the gauge measurements. The CRR and OFRR algorithms best correlation scores are at the lower CAPPI levels as expect and the correlation scores decreases as the CAPPI height increase, as expected. However, the CRR scores better than the OFRR algorithm on all levels. This is not the case when considering the correlation scores on a monthly basis. Comparing the two algorithms over all CAPPI levels for each month and the OFRR algorithm out performs the CRR algorithm 37.5% of all the cases. The OFRR having the highest correlation score for the month of October at the 2.5 km CAPPI. The CRR algorithm has the highest scores for November and January at the 3.0 km and 2.5 km CAPPI's respectively. The TITAN algorithm outperforms both CRR and OFRR algorithms in terms of correlation during December, February and March. Thus, considering hourly accumulations TITAN is the algorithm that is best correlated followed by the CRR and the OFRR algorithms. When considering the correlation with daily accumulation in Table 5-4 we see for the study period the TITAN algorithm is once again the best correlated with a correlation of 0.682. However, if we investigate month by month we see that the TITAN algorithm only has the best correlation for February and March. For October and November the CRR algorithm at a 2.5 km CAPPI has the best correlation, December the OFRR algorithm at 2.5 km is on top and for January there is a tie between the CRR and OFRR algorithms. The CRR algorithm is the best correlated 58% of the time when considering all months and CAPPI levels. However, when considering the entire study period the OFRR algorithm outperforms the CRR algorithm on every CAPPI level.

The next 2 tables, Table 5-5 and Table 5-6, has then same layout as the previous 2 tables the only difference being that the bias scores are depicted in the table. Again, Table 5-5 and Table 5-6 represent hourly and daily accumulation respectively. In Table 5-5 it is clear that the TITAN algorithm is extremely bias indicated by the red colour of the cells. The use of CAPPI levels has significantly lowered the bias scores. The best bias score of 0.012 mm comes from the CRR algorithm at the 2.5 km CAPPI followed closely by the OFRR algorithm at the same level with a score of 0.013 mm. The bias scores for both the CRR and OFRR algorithms does not differ significantly with the largest difference no more than 0.003 mm between them. The lower CAPPI levels have a tendency to over-estimate and the general trend to under-estimation starts at the 5.5 km CAPPI.

Table 5-5: Bias scores for hourly measurements of the CRR and OFRR algorithms at the respective CAPPI levels. The TITAN algorithm is include for reference and the CAPPI level SURFACE represents the vertical column of reflectivities being projected to the surface for calculations.

	Algorithm	CAPPI	PERIOD	OCT	NOV	DEC	JAN	FEB	MAR
1	TITAN	SURFACE	0.203	0.171	0.175	0.221	0.152	0.203	0.274
2	CRR	2.5	0.012	0.059	0.012	-0.002	-0.060	0.042	0.050
3	OFRR	2.5	0.013	0.055	0.014	0.000	-0.060	0.040	0.051
4	CRR	3.0	0.021	0.065	0.028	0.027	-0.045	0.039	0.041
5	OFRR	3.0	0.022	0.060	0.030	0.029	-0.043	0.039	0.042
6	CRR	3.5	0.034	0.063	0.047	0.050	-0.031	0.043	0.051
7	OFRR	3.5	0.035	0.061	0.049	0.053	-0.030	0.043	0.052
8	CRR	4.5	0.017	0.029	0.004	0.007	0.000	0.027	0.041
9	OFRR	4.5	0.016	0.028	0.005	0.008	-0.003	0.026	0.039
10	CRR	5.5	-0.074	0.020	-0.041	-0.127	-0.153	-0.018	-0.070
11	OFRR	5.5	-0.074	0.018	-0.041	-0.126	-0.151	-0.019	-0.071
12	CRR	7.0	-0.120	0.000	-0.074	-0.191	-0.211	-0.049	-0.122
13	OFRR	7.0	-0.120	0.000	-0.075	-0.190	-0.208	-0.050	-0.122
14	CRR	8.5	-0.148	-0.022	-0.098	-0.240	-0.232	-0.070	-0.148
15	OFRR	8.5	-0.148	-0.023	-0.098	-0.238	-0.231	-0.071	-0.149
16	CRR	10.0	-0.164	-0.042	-0.109	-0.268	-0.244	-0.083	-0.162
17	OFRR	10.0	-0.164	-0.041	-0.110	-0.267	-0.244	-0.082	-0.162

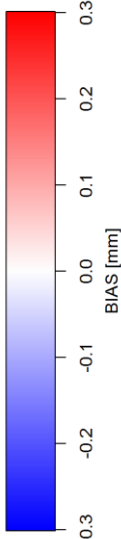
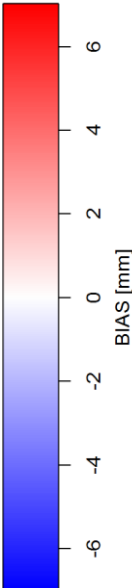


Table 5-6: Bias scores for daily measurements of the CRR and OFRR algorithms at the respective CAPPI levels. The TITAN algorithm is include for reference and the CAPPI level SURFACE represents the vertical column of reflectivities being projected to the surface for calculations.

	Algorithm	CAPPI	PERIOD	OCT	NOV	DEC	JAN	FEB	MAR
1	TITAN	SURFACE	4.698	3.473	4.444	5.065	3.511	4.505	6.357
2	CRR	2.5	0.187	1.038	0.710	-0.228	-1.341	0.787	1.305
3	OFRR	2.5	0.202	1.034	0.738	-0.229	-1.344	0.787	1.376
4	CRR	3.0	0.298	1.109	0.906	0.184	-1.077	0.675	1.083
5	OFRR	3.0	0.307	1.117	0.920	0.162	-1.067	0.677	1.128
6	CRR	3.5	0.683	1.041	1.358	0.780	-0.621	0.853	1.479
7	OFRR	3.5	0.686	1.104	1.356	0.755	-0.632	0.846	1.519
8	CRR	4.5	0.339	0.358	0.517	-0.093	-0.222	0.408	1.333
9	OFRR	4.5	0.332	0.375	0.462	-0.054	-0.295	0.412	1.351
10	CRR	5.5	-2.097	0.144	-0.444	-3.437	-3.943	-0.553	-1.480
11	OFRR	5.5	-2.098	0.158	-0.463	-3.434	-3.938	-0.549	-1.491
12	CRR	7.0	-3.220	-0.303	-1.161	-4.989	-5.333	-1.177	-2.713
13	OFRR	7.0	-3.207	-0.267	-1.187	-4.966	-5.307	-1.177	-2.703
14	CRR	8.5	-3.838	-0.788	-1.632	-6.045	-5.818	-1.556	-3.322
15	OFRR	8.5	-3.831	-0.758	-1.653	-6.027	-5.806	-1.556	-3.326
16	CRR	10.0	-4.196	-1.168	-1.891	-6.666	-6.084	-1.817	-3.615
17	OFRR	10.0	-4.193	-1.144	-1.910	-6.659	-6.079	-1.811	-3.617



When analysing the individual months an over-estimation of precipitation dominates at the lower levels except for the month of January when an under-estimation was observed. Considering all the months and CAPPI levels the OFRR algorithm had the best score for 42% of the 48 cases. The CRR algorithm was better for 39% while 19% of the case there were no difference in bias scores at all. An over-estimation in precipitation is illustrated by Table 5- 6 for the daily accumulation by the TITAN algorithm. The best bias score is the CRR algorithm with 0.187 mm again followed closely by the OFRR algorithm with 0.202 mm, both at the 2.5 km CAPPI level. This is a large improvement from the 4.698 mm over-estimation by the TITAN algorithm. Considering all the months and CAPPI levels in Table 5-6 the CRR algorithm had the best score for 48% of the 48 cases. The OFRR algorithm outscored the CRR algorithm with 46% of cases, while for 6% there was no difference in the bias score at all. However, there is a trend where the CRR algorithm outperformed the OFRR algorithm at the lower CAPPI level and the OFRR algorithm outperformed the CRR algorithm at the higher levels. At the higher CAPPI levels there was much smaller under-estimations observed in the drier months of October, November and February compared to the other wetter months.

The next two tables, Table 5-7 and Table 5-8, have the same layout as the previous four tables the only difference being that the RMSE scores are depicted in the table. Table 5-7 and Table 5-8 represent hourly and daily accumulation respectively. Considering the hourly accumulation error scores in Table 5-7 the lowest error score of 0.899 mm for the entire study period comes from the CRR algorithm at the 2.5 km CAPPI level. However, the OFRR algorithm is only a little larger at with an error score of 0.907 mm at the 2.5 km CAPPI level. The OFRR algorithm then goes on to outperform the CRR algorithm at the 3.0, 3.5, and 5.5 km CAPPI levels. The OFRR and CRR algorithms are only out scored by the TITAN algorithm at the 5.5 km CAPPI level and up. Considering all the months and CAPPI levels in Table 5-7 the CRR algorithm had the best score for 52% of the 48 cases. The OFRR algorithm however scored better at most of the months within the study period at the lower CAPPI level, except for the 2.5 km CAPPI level where the CRR algorithm outperformed the OFRR algorithm. Considering the daily accumulations of Table 5-8, the CRR algorithm again has the best error score of 8.385 mm at the 2.5 km CAPPI. Outperforming the OFRR algorithm by 0.002 mm. However, the CRR algorithm only outperforms the OFRR algorithm during October and March for the study period at the 2.5 km CAPPI. . Considering all the months and CAPPI levels in Table 5-8 the OFRR algorithm had the best score for 61% of the 48 cases. Outperforming the CRR algorithm at all CAPPI levels, except the 2.5 km level.

Table 5-7: RMSE scores for hourly measurements of the CRR and OFRR algorithms at the respective CAPPI levels. The TITAN algorithm is include for reference and the CAPPI level SURFACE represents the vertical column of reflectivities being projected to the surface for calculations.

	Algorithm	CAPPI	PERIOD	OCT	NOV	DEC	JAN	FEB	MAR
1	TITAN	SURFACE	0.987	0.761	0.837	1.125	1.141	0.816	1.039
2	CRR	2.5	0.899	0.676	0.591	1.086	1.037	0.773	0.974
3	OFRR	2.5	0.907	0.579	0.617	1.089	1.062	0.739	1.017
4	CRR	3.0	0.941	0.767	0.652	1.122	1.055	0.833	1.014
5	OFRR	3.0	0.940	0.652	0.651	1.111	1.074	0.804	1.055
6	CRR	3.5	0.972	0.730	0.753	1.148	1.108	0.851	1.013
7	OFRR	3.5	0.969	0.624	0.726	1.138	1.124	0.830	1.054
8	CRR	4.5	0.941	0.481	0.569	1.099	1.253	0.811	0.944
9	OFRR	4.5	0.935	0.430	0.564	1.068	1.254	0.791	0.973
10	CRR	5.5	1.024	0.474	0.676	1.363	1.281	0.782	0.991
11	OFRR	5.5	1.029	0.426	0.696	1.358	1.295	0.766	1.015
12	CRR	7.0	1.150	0.491	0.812	1.493	1.408	0.825	1.208
13	OFRR	7.0	1.154	0.443	0.829	1.500	1.413	0.823	1.214
14	CRR	8.5	1.227	0.495	0.893	1.580	1.460	0.911	1.321
15	OFRR	8.5	1.231	0.461	0.907	1.588	1.464	0.906	1.325
16	CRR	10.0	1.270	0.418	0.927	1.650	1.486	0.952	1.376
17	OFRR	10.0	1.271	0.442	0.931	1.649	1.487	0.949	1.380

Table 5-8: RMSE scores for daily measurements of the CRR and OFRR algorithms at the respective CAPPI levels. The TITAN algorithm is include for reference and the CAPPI level SURFACE represents the vertical column of reflectivities being projected to the surface for calculations.

	Algorithm	CAPPI	PERIOD	OCT	NOV	DEC	JAN	FEB	MAR
1	TITAN	SURFACE	10.807	5.678	8.020	14.083	10.024	7.639	12.325
2	CRR	2.5	8.385	3.756	4.498	11.833	8.193	5.060	8.953
3	OFRR	2.5	8.387	3.856	4.456	11.718	8.186	5.036	9.148
4	CRR	3.0	8.652	4.025	4.849	12.304	8.273	5.221	9.210
5	OFRR	3.0	8.600	4.152	4.787	12.071	8.252	5.210	9.335
6	CRR	3.5	9.050	3.772	5.502	12.872	8.570	5.593	9.606
7	OFRR	3.5	8.980	4.064	5.432	12.588	8.541	5.569	9.718
8	CRR	4.5	8.947	2.763	4.817	12.035	9.570	5.153	9.800
9	OFRR	4.5	8.782	2.993	4.469	11.787	9.323	5.162	9.705
10	CRR	5.5	9.930	2.728	4.787	14.732	10.640	4.959	9.186
11	OFRR	5.5	9.882	2.982	4.522	14.641	10.626	4.990	9.124
12	CRR	7.0	10.898	3.036	5.094	15.798	12.163	5.400	10.147
13	OFRR	7.0	10.883	3.231	4.850	15.783	12.142	5.425	10.140
14	CRR	8.5	11.485	3.485	5.228	16.503	12.724	5.825	11.008
15	OFRR	8.5	11.482	3.586	5.117	16.500	12.717	5.837	11.012
16	CRR	10.0	11.845	3.842	5.264	16.969	13.036	6.117	11.496
17	OFRR	10.0	11.843	3.857	5.229	16.966	13.031	6.121	11.501

The OFRR and CRR algorithm outperform the TITAN algorithm up to the 5.5 km CAPPI level. It is also evident from both Table 5-7 and 5-8, that smaller error scores are associated for the drier than normal months of October, November and February, compared to the wetter than normal months of December, January and March.

Table 5-9 and 5-10 represent contingency table scores for 1, 5 and 10 mm thresholds. They also correspond to hourly and daily accumulation values respectively. The first column holds the algorithm name, the second the threshold in millimetres used to construct the contingency table and the third the CAPPI level in kilometres AMSL. The variable surface is used within the table together with the TITAN algorithm. This implies that a vertical column of reflectivities is used to calculate the surface precipitation. The rest of the column in the table lists the following score from left to right; the Equitable Thread Score (ETS), Critical Success Index (CSI), Probability of Detection (POD), False Alarm Ratio (FAR), Heidke Skill Score (HSS), Accuracy (ACC) and bias (BIAS). Considering the scores of the hourly values in Table 5-9 the best ETS and CSI score at the 1 mm threshold comes from the CRR algorithm at the 3.0 km CAPPI, it is closely followed by the OFRR algorithm. Both the OFRR and CRR algorithm outperform the TITAN algorithm up to the 4.5 km CAPPI level. The CRR algorithm performs the best on most CAPPI levels compared to the OFRR algorithm at the 1 mm threshold. With the 5 mm threshold the TITAN algorithm scores the best but is closely followed by the scores of the CRR and OFRR algorithms at the 3.0 km CAPPI.

The CRR performs best on most CAPPI levels. With the 10 mm threshold the CRR algorithm at the 3.0 km CAPPI again has the highest ETS, followed by TITAN algorithm and then the OFRR algorithm. Considering the different thresholds the CRR algorithm is superior over the different CAPPI levels. The 3.0 km CAPPI has the best result and the algorithms are much more accurate with the smaller thresholds. Considering the POD and FAR it is clear that the TITAN algorithm has the highest scores. However, it also has the highest FAR scores as well. The biggest FAR comes from the higher CAPPI levels but the FAR for the TITAN algorithm by far exceeds the FAR of the OFRR and CRR algorithms at the lower CAPPI levels. Taking both POD and FAR into account the CRR algorithm at the 2.5 km CAPPI performs the best at a 1 mm threshold. For the 5 and 10 mm threshold the TITAN algorithm performs better detecting the larger accumulation values. The HSS show that the CRR algorithm at a 2.5 km CAPPI level, the TITAN algorithm and the CRR algorithm at the 3.0 km CAPPI level has the best skill at 1, 5 and 10 mm thresholds respectively. The CRR algorithm also shows greater skill at most CAPPI levels.

Table 5-9: Contingency table scores using thresholds of 1, 5 and 10 mm are listed in the table below. The scores are listed with the corresponding algorithm, threshold and CAPPI level. The scores are based on hourly accumulated values. The best scores in each category are highlighted in red.

	ALGO	THRESHOLD	Level	ETS	CSI	POD	FAR	HSS	ACC	BIAS
1	TITAN	1	SURFACE	0.524	0.539	0.911	0.431	0.687	0.973	1.600
2	CRR	1	2.5	0.618	0.629	0.781	0.237	0.764	0.984	1.023
3	OFC	1	2.5	0.596	0.607	0.772	0.261	0.747	0.983	1.044
4	CRR	1	3.0	0.613	0.624	0.807	0.267	0.760	0.983	1.101
5	OFC	1	3.0	0.604	0.616	0.813	0.283	0.753	0.983	1.133
6	CRR	1	3.5	0.583	0.595	0.819	0.315	0.736	0.981	1.195
7	OFC	1	3.5	0.574	0.587	0.821	0.327	0.730	0.980	1.220
8	CRR	1	4.5	0.551	0.565	0.792	0.338	0.711	0.979	1.196
9	OFC	1	4.5	0.550	0.563	0.795	0.342	0.709	0.979	1.207
10	CRR	1	5.5	0.432	0.444	0.529	0.266	0.604	0.977	0.721
11	OFC	1	5.5	0.428	0.440	0.528	0.274	0.600	0.977	0.727
12	CRR	1	7.0	0.210	0.219	0.242	0.306	0.348	0.971	0.349
13	OFC	1	7.0	0.211	0.219	0.244	0.314	0.348	0.970	0.356
14	CRR	1	8.5	0.093	0.097	0.101	0.293	0.170	0.968	0.144
15	OFC	1	8.5	0.097	0.101	0.106	0.291	0.176	0.968	0.149
16	CRR	1	10.0	0.047	0.049	0.050	0.181	0.090	0.967	0.061
17	OFC	1	10.0	0.046	0.048	0.048	0.184	0.088	0.967	0.059
18	TITAN	5	SURFACE	0.449	0.453	0.848	0.507	0.619	0.990	1.719
19	CRR	5	2.5	0.423	0.427	0.572	0.373	0.594	0.993	0.912
20	OFC	5	2.5	0.403	0.406	0.551	0.393	0.574	0.992	0.908
21	CRR	5	3.0	0.441	0.445	0.627	0.394	0.613	0.993	1.035
22	OFC	5	3.0	0.440	0.444	0.629	0.398	0.611	0.992	1.045
23	CRR	5	3.5	0.439	0.444	0.668	0.431	0.610	0.992	1.174
24	OFC	5	3.5	0.438	0.443	0.664	0.430	0.610	0.992	1.164
25	CRR	5	4.5	0.391	0.395	0.576	0.444	0.562	0.992	1.035
26	OFC	5	4.5	0.401	0.405	0.582	0.429	0.573	0.992	1.018
27	CRR	5	5.5	0.201	0.204	0.234	0.387	0.335	0.991	0.381
28	OFC	5	5.5	0.194	0.197	0.221	0.361	0.325	0.991	0.346
29	CRR	5	7.0	0.117	0.119	0.127	0.347	0.210	0.991	0.195
30	OFC	5	7.0	0.116	0.118	0.125	0.337	0.208	0.991	0.189
31	CRR	5	8.5	0.037	0.038	0.039	0.406	0.072	0.991	0.066
32	OFC	5	8.5	0.044	0.044	0.045	0.312	0.084	0.991	0.066
33	CRR	5	10.0	0.014	0.014	0.014	0.500	0.027	0.990	0.029
34	OFC	5	10.0	0.010	0.010	0.010	0.545	0.020	0.990	0.023
35	TITAN	10	SURFACE	0.355	0.357	0.728	0.588	0.524	0.995	1.766
36	CRR	10	2.5	0.346	0.347	0.495	0.462	0.514	0.997	0.918
37	OFC	10	2.5	0.308	0.309	0.446	0.497	0.471	0.996	0.886
38	CRR	10	3.0	0.371	0.372	0.554	0.469	0.541	0.997	1.043
39	OFC	10	3.0	0.352	0.354	0.533	0.487	0.521	0.996	1.038
40	CRR	10	3.5	0.358	0.359	0.576	0.512	0.527	0.996	1.179
41	OFC	10	3.5	0.339	0.341	0.549	0.526	0.507	0.996	1.158
42	CRR	10	4.5	0.276	0.277	0.413	0.542	0.432	0.996	0.902
43	OFC	10	4.5	0.256	0.258	0.391	0.569	0.408	0.996	0.908
44	CRR	10	5.5	0.188	0.189	0.223	0.446	0.316	0.997	0.402
45	OFC	10	5.5	0.163	0.164	0.196	0.500	0.280	0.996	0.391
46	CRR	10	7.0	0.079	0.080	0.087	0.500	0.147	0.996	0.174
47	OFC	10	7.0	0.073	0.074	0.082	0.559	0.137	0.996	0.185
48	CRR	10	8.5	0.031	0.031	0.033	0.538	0.060	0.996	0.071
49	OFC	10	8.5	0.026	0.026	0.027	0.667	0.050	0.996	0.082
50	CRR	10	10.0	0.000	0.000	0.000	1.000	0.000	0.996	0.005
51	OFC	10	10.0	0.005	0.005	0.005	0.667	0.011	0.996	0.016



Table 5-10: Contingency table scores using thresholds of 1, 5 and 10 mm are listed in the table below. The scores are listed with the corresponding algorithm, threshold and CAPPI level. The scores are based on daily accumulated values. The best scores in each category are highlighted in red.

	ALGO	THRESHOLD	Level	ETS	CSI	POD	FAR	HSS	ACC	BIAS
1	TITAN	1	SURFACE	0.062	0.352	0.978	0.645	0.117	0.439	2.758
2	CRR	1	2.5	0.372	0.556	0.892	0.404	0.542	0.776	1.497
3	OFC	1	2.5	0.371	0.556	0.897	0.406	0.542	0.775	1.512
4	CRR	1	3.0	0.473	0.625	0.892	0.323	0.642	0.833	1.318
5	OFC	1	3.0	0.469	0.624	0.898	0.329	0.639	0.830	1.338
6	CRR	1	3.5	0.471	0.624	0.896	0.327	0.640	0.831	1.330
7	OFC	1	3.5	0.466	0.621	0.898	0.332	0.635	0.828	1.344
8	CRR	1	4.5	0.455	0.612	0.880	0.333	0.625	0.825	1.320
9	OFC	1	4.5	0.451	0.609	0.879	0.336	0.622	0.823	1.323
10	CRR	1	5.5	0.453	0.600	0.811	0.302	0.623	0.831	1.161
11	OFC	1	5.5	0.452	0.600	0.810	0.302	0.622	0.830	1.161
12	CRR	1	7.0	0.343	0.482	0.597	0.285	0.511	0.799	0.835
13	OFC	1	7.0	0.351	0.490	0.608	0.283	0.520	0.802	0.847
14	CRR	1	8.5	0.187	0.291	0.330	0.288	0.315	0.748	0.464
15	OFC	1	8.5	0.184	0.290	0.330	0.298	0.311	0.746	0.471
16	CRR	1	10.0	0.076	0.127	0.134	0.282	0.141	0.712	0.186
17	OFC	1	10.0	0.076	0.129	0.136	0.290	0.142	0.712	0.192
18	TITAN	5	SURFACE	0.282	0.430	0.889	0.546	0.440	0.743	1.956
19	CRR	5	2.5	0.457	0.555	0.760	0.327	0.627	0.866	1.129
20	OFC	5	2.5	0.458	0.557	0.768	0.330	0.629	0.866	1.148
21	CRR	5	3.0	0.469	0.567	0.784	0.327	0.639	0.869	1.165
22	OFC	5	3.0	0.459	0.558	0.776	0.335	0.629	0.865	1.167
23	CRR	5	3.5	0.444	0.548	0.795	0.361	0.615	0.857	1.243
24	OFC	5	3.5	0.447	0.552	0.798	0.359	0.618	0.858	1.245
25	CRR	5	4.5	0.432	0.535	0.757	0.354	0.603	0.856	1.171
26	OFC	5	4.5	0.433	0.537	0.763	0.356	0.605	0.856	1.184
27	CRR	5	5.5	0.305	0.389	0.467	0.299	0.467	0.839	0.666
28	OFC	5	5.5	0.304	0.389	0.466	0.298	0.467	0.839	0.664
29	CRR	5	7.0	0.138	0.187	0.203	0.287	0.242	0.807	0.284
30	OFC	5	7.0	0.141	0.192	0.208	0.290	0.247	0.808	0.293
31	CRR	5	8.5	0.054	0.076	0.078	0.265	0.103	0.792	0.106
32	OFC	5	8.5	0.055	0.077	0.079	0.256	0.105	0.792	0.106
33	CRR	5	10.0	0.022	0.030	0.031	0.244	0.043	0.785	0.041
34	OFC	5	10.0	0.019	0.027	0.027	0.250	0.038	0.785	0.036
35	TITAN	10	SURFACE	0.311	0.402	0.849	0.567	0.475	0.821	1.964
36	CRR	10	2.5	0.398	0.463	0.653	0.386	0.570	0.892	1.063
37	OFC	10	2.5	0.402	0.466	0.654	0.382	0.573	0.893	1.059
38	CRR	10	3.0	0.414	0.480	0.695	0.392	0.586	0.893	1.142
39	OFC	10	3.0	0.413	0.479	0.695	0.393	0.585	0.893	1.144
40	CRR	10	3.5	0.408	0.476	0.721	0.416	0.579	0.887	1.234
41	OFC	10	3.5	0.407	0.475	0.713	0.413	0.578	0.888	1.213
42	CRR	10	4.5	0.407	0.472	0.668	0.384	0.579	0.894	1.084
43	OFC	10	4.5	0.401	0.466	0.665	0.391	0.573	0.892	1.092
44	CRR	10	5.5	0.205	0.247	0.280	0.328	0.340	0.878	0.417
45	OFC	10	5.5	0.205	0.245	0.276	0.312	0.340	0.879	0.402
46	CRR	10	7.0	0.087	0.107	0.113	0.319	0.160	0.866	0.166
47	OFC	10	7.0	0.091	0.111	0.116	0.284	0.166	0.868	0.162
48	CRR	10	8.5	0.037	0.045	0.046	0.283	0.071	0.862	0.064
49	OFC	10	8.5	0.038	0.048	0.049	0.300	0.074	0.862	0.070
50	CRR	10	10.0	0.008	0.010	0.010	0.300	0.015	0.859	0.014
51	OFC	10	10.0	0.008	0.010	0.010	0.222	0.016	0.859	0.013



The bias again show large over-estimation from the TITAN algorithm compared to the other algorithms. At the 1 mm threshold the CRR algorithm at the 2.5 km CAPPI level illustrates the best result. An over-estimation is observed up to the 4.5 km CAPPI where under-estimation is then dominant as the CAPPI level increase in height. With the 5 mm threshold the CRR algorithm at a 3.0 km CAPPI has the smallest bias. The CRR algorithm also outperforms the OFRR algorithm at most CAPPI levels. The 2.5 km CAPPI illustrates under-estimation, but the 3.0 – 4.5 km CAPPI over- estimation is observed. With the 10 mm threshold the OFRR algorithm has the smallest bias score at the 3.0 km CAPPI level. The OFRR algorithm outperforms the CRR algorithm at most of the CAPPI levels at the 10 mm threshold. The 2.5 km CAPPI level under-estimates, with over-estimation only at the 3.0 and 3.5 km CAPPI levels. The accuracy score in this regard does not add any value because of the high frequency of both instruments measuring 0 mm of precipitation.

Table 5-10 is similar to Table 5-9 except that is illustrated the contingency table scores using daily accumulations. The CRR algorithm at the 3.0 km CAPPI level show the best ETS and CSI scores at all threshold of 1, 5 and 10 mm. The TITAN algorithm does not perform very well at the smaller thresholds but it does improve with an increase in threshold. The CRR algorithm outperforms the OFRR algorithm at most CAPPI levels except at the 5 mm threshold. Although the CRR algorithm has the highest score it is very closely followed by the OFRR algorithm. For the POD and FAR the TITAN algorithm scores the highest at all thresholds. Considering both the POD and FAR scores the OFRR and CRR algorithm at the 3.0 km CAPPI scores the best.

The CRR algorithm at 3.0 km and 3.5 km CAPPI levels scores the best at 5 and 10 mm thresholds respectively. The CRR algorithm at the 3.0 km CAPPI level again has the highest skill with the best HSS scores at all thresholds. The bias again indicates large over-estimations by the TITAN algorithm. With the smallest bias at the 5.5 km CAPPI level for the 1 mm threshold and 2.5 km CAPPI level for the 5 and 10 mm thresholds. An over-estimation is observed at the lower CAPPI levels and the higher CAPPI levels under-estimation is observed. Form Table 5-9 and Table 5-10 it is clear that the lower CAPPI levels perform well as expected. Although there is not much of a difference between the CRR and OFRR algorithms the CRR algorithm seems to be edging in front of the OFRR algorithm on a regular basis.

Figure 5-10 is similar to Figure 5-7 however it includes the CRR algorithm calculated on the different CAPPI levels. Figure 5-10 (a) illustrates the hourly measurements while Figure 5-10 (b) the daily measurements. The top graph illustrates the average cumulative sum of the radar estimates and gauge measurements. The bottom graph illustrates the Cumulative

Distribution Function (CDF) for the study period considering only non zero precipitation events.

Thus, the CDFs reflect the probability of a specific value occurring whenever precipitation occurs. With both the hourly and daily measurements (Figure 5-10 (a) and (b)) the TITAN algorithm estimates illustrates a much more rapid growth than the gauge measurements as well as the CRR algorithm on any of the CAPPI levels and it continues to deviate away as time progress. The hourly gauges recorded 673 mm during the study period and the TITAN algorithm 1255 mm as mentioned in Figure 5-7. Similarly, the daily gauges measured a total of 665 mm with the TITAN algorithm over-estimating at 1414 mm. For both the hourly and daily measurements the CRR at the 2.5 km CAPPI level was the closest accumulation to the gauges. The CRR algorithm measured 682 mm and 703 mm for the hourly and daily measurements respectively. However, it was followed very closely by the OFRR algorithm, measuring 684 mm and 706 mm respectively at the 2.5 km CAPPI level. A slightly higher accumulation is observed when the CAPPI level increases until the 5.5 km CAPPI level where a sharp drop in the total accumulation is shown. The CDF graph in Figure 5-10 (a) and (b) both illustrate that the lower CAPPI levels closely follow the CDF curve that represents the gauges, with the 2.5 km CAPPI being the most accurate. The higher CAPPI levels and TITAN algorithm deviates quite significantly.

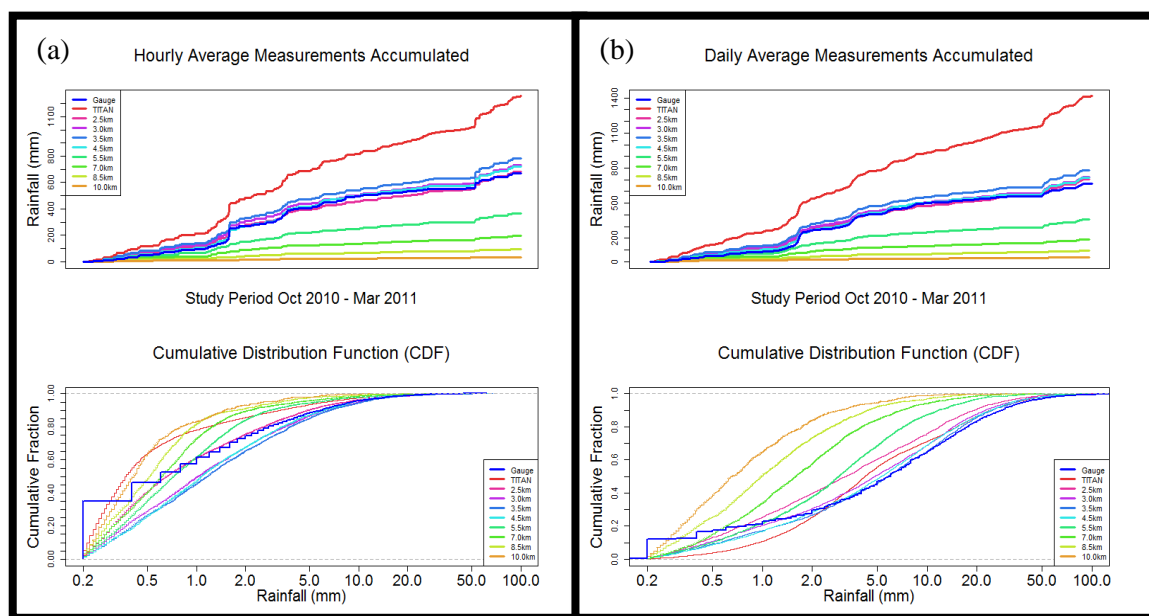


Figure 5-10: Gauge, TITAN algorithm and CRR algorithm at all CAPPI levels for hourly accumulation (a) and daily accumulation (b) for the study period of October 2010 – March 2011. The associated Cumulative Distribution Function (CDF) considering only measurement that are not zero, are also illustrated in the lower panels, in which the cumulative fraction ranges from 0 to 1 and the horizontal axes are logarithmic scales.

## 5.4. Precipitation Performance with Range

The TITAN and CRR algorithms were also evaluated in terms of range from the radar. The CRR algorithm was selected for the comparison with TITAN, because the CRR algorithm had mostly favourable results compared to the OFRR algorithm. Nevertheless, the differences were small and the results did not differ much compared to the CRR, so either algorithm would produce similar results for the range comparison.

Figure 5-11 illustrates the correlation coefficient for hourly (a) and daily (b) measurements in terms of the range interval separated by 30 km. The Blue line is the TITAN algorithm while the rest represents the CRR algorithm at the different CAPPI levels. The bars at the bottom of the graph indicate the number of gauges available within the indicated radius. The range intervals are labelled with the start range of the interval. It is clear from the graph that the lower CAPPI levels in both Figure 5-11 (a) and Figure 5-11 (b) are performing the best together with the TITAN algorithm. These include the 2.5, 3.0 and 3.5 km CAPPI levels. However, all these CAPPI levels including the TITAN algorithm drop significantly to much lower correlations once the range of 150 km is exceeded. The lower the CAPPI level the shorter the range at which it can effectively measure the precipitation estimates.

Figures 5-12 illustrates the bias for hourly (a) and daily (b) measurements in terms of the range intervals. A similar pattern is observed with both Figures 5-12 (a) and (b). The TITAN algorithm illustrates an extreme bias near the radar and it decrease linearly as the range from the radar increases. The lower CAPPI levels from the CRR algorithm show a slight over-estimation near the radar but they soon start to under-estimate as the range from the radar increases.

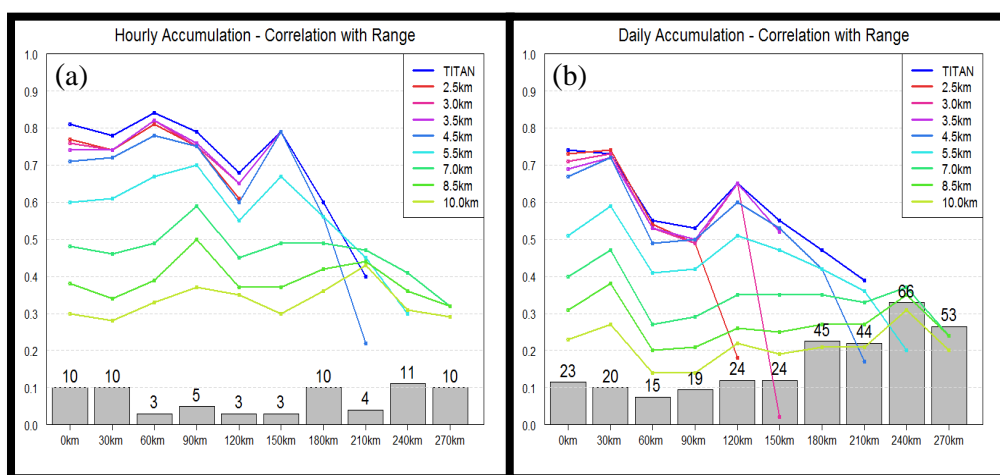


Figure 5-11: The correlation coefficient at range intervals for the TITAN algorithm and CRR algorithm at all CAPPI levels for hourly accumulation (a) and daily accumulation (b) for the study period of October 2010 – March 2011. The grey bars indicate the number of gauges within each range ring.

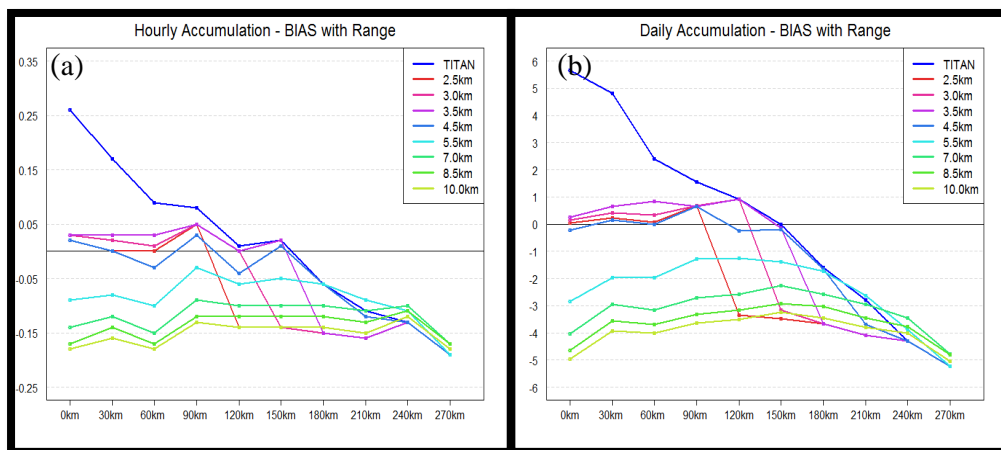


Figure 5-12: The bias at range intervals for the TITAN algorithm and CRR algorithm at all CAPPI levels for hourly accumulation (a) and daily accumulation (b) for the study period of October 2010 – March 2011.

The 2.5 km CAPPI start the under-estimation at 90-120 km, the 3.0 km CAPPI at 120-150 km and from 150 km all, including the TITAN algorithm, start to under-estimate.

Figure 5-13 illustrates the RMSE for hourly (a) and daily (b) measurements in terms of the range intervals. The same pattern is observed as in Figures 5-11 and 5-12. The lower CAPPI levels perform the best, but start to increase in error as the range from the radar increases. Again all errors increase past the 150 km mark. Thus, it is safe to say that no matter what type of algorithm is used, past the 150 km mark precipitation estimates dramatically decline in reliability.

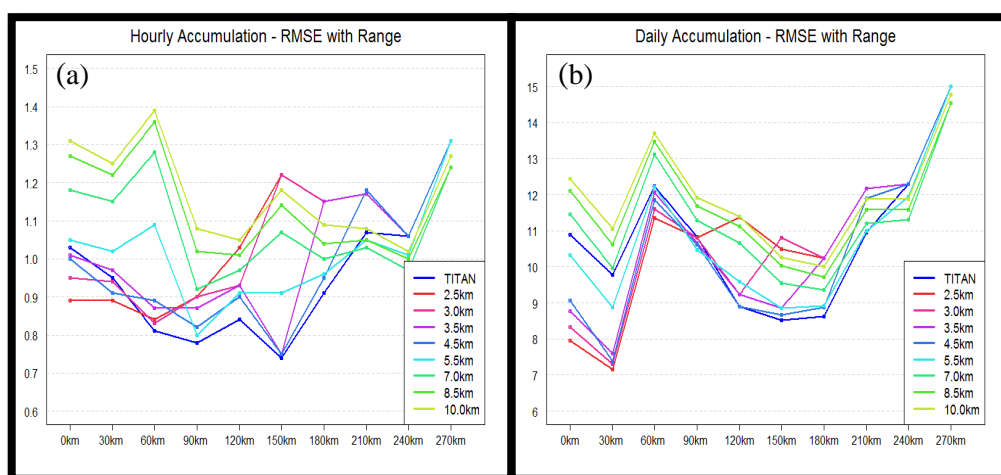


Figure 5-13: The RMSE at range intervals for the TITAN algorithm and CRR algorithm at all CAPPI levels for hourly accumulation (a) and daily accumulation (b) for the study period of October 2010 – March 2011.

## **5.5. Summary**

In this chapter the information regarding the performance of the classification scheme and precipitation algorithms was presented and discussed. The classification scheme illustrated a tendency to over-estimate the frequency of convective rainfall. The CRR and OFRR algorithms performed better than the TITAN algorithm. However, there were very small differences between the CRR and OFRR algorithm. It became clear that the lower the CAPPI level is to the ground, the better it will perform compared to the gauge measurements, which one would hope to be the case. It was also determined that precipitation estimates have little quantitative value beyond 150 km from the radar. These findings and more will be discussed further in the next chapter.

---

## CHAPTER 6

### SUMMARY AND CONCLUSIONS

---

#### 6.1 Introduction

Although there is a summary at the end of each chapter it is fitting to review the critical points set out there. Chapter 1 introduced the aims and objectives of the study. The objectives were to introduce instantaneous precipitation classification so that a dual Z-R relationship technique can be applied to convective and stratiform classified rainfall, and to account for storm movement between successive scans by integrating precipitation over a computed vector path that is based on optical flow techniques. Chapter 2 discussed the history of radar in South Africa followed by an in depth look at all aspects involved with radar precipitation, such as the theories behind error correction and techniques for rain rate estimation from reflectivities. Chapter 3 discussed the computer algorithms that were written to address the study objectives. The algorithms incorporate a 2 dimensional classification scheme (Chumchean et al., 2008), and optical flow techniques to calculate motion vectors between successive scans (Bowler et al., 2004), applies a dual Z-R relationship to convert reflectivity to rain rate (Chumchean et al., 2008), then accumulation through the integration of precipitation with motion vectors (Hannesen, 2002). By applying these algorithms to extracted CAPPI data, the aim was to improve the radars' precipitation estimates. Chapter 4 then discussed the evaluation method over a number of different CAPPI level heights and the use of rain gauge data as the basis for verification. The advantages and limitation of both rain gauge and radar datasets were also discussed. Chapter 5 then evaluated the results of the evaluation methods. All this was done with one question in mind: can these techniques improve on the current operational QPE algorithm available at the SAWS? To answer the question, the following sections in this chapter will address the conclusions drawn about whether the classification scheme can accurately classify the radar reflectivities and whether the use of optical flow vectors have any benefit as well.

#### 6.2 Classifying Precipitation

How well can the classification scheme distinguish between convective and stratiform precipitation? To answer this question 5 minute rain rate from various gauges as well as the Vertical Profile of Reflectivity (VPR) were analysed. The overall analysis showed that the

classification scheme can distinguish between convective and stratiform precipitation reasonably well. The analysis of the Wonderboom Airport VPR showed very favourable results for the classification scheme, successfully classifying convective precipitation observed from the 5 minute rain rate and VPR as convective precipitation. When stratiform precipitation is observed the classification scheme also does a reasonably good job in classifying the precipitation correctly. However, the classification scheme seems to struggle to distinguish between the two classifications whenever a region of stratiform precipitation follows a convective line or when stratiform precipitation has a high rain rate. Thus, the classification scheme tends to over-estimate the frequency of convective precipitation.

### **6.3 Algorithm Comparison**

The next step was to determine whether the use of a dual Z-R relationship can improve on the existing TITAN precipitation algorithm. The Classified Rain Rate (CRR) algorithm was created and precipitation was generated on multiple CAPPI levels. The CRR estimates were then compared to the TITAN precipitation algorithm. After this comparative analysis, the tendency for the TITAN algorithm to under-estimate extreme precipitation events was identified, in addition, both the hourly and daily measurements are in general over-estimated by TITAN. The CRR algorithm computed an increase in rainfall within the convective region due to the strong convective Z-R relationship. Using this particular dual Z-R relationship has shown a small improvement over using a single relationship such as the Marshall-Palmer relationship (Poolman et al., 2014). However, using a single CAPPI level to estimate the rainfall proves to be the most significant improvement within the algorithm. The lower the CAPPI level the more accurate the estimation, but with larger precipitation thresholds slightly higher CAPPI levels such as the 3.0 and 3.5 km CAPPI perform better. By using several CAPPI levels to estimate the precipitation, the capability to detect larger precipitation thresholds can decrease significantly. From the 5.5 km CAPPI level and upwards there is no skill in the precipitation estimates. The CRR algorithm thus outperforms the TITAN algorithm.

The Optical Flow Rain Rate (OFRR) algorithm was created to determine if the smoothing of precipitation accumulations using optical flow techniques further improve the precipitation algorithm. This method accounts for errors that might occur due to the temporal resolution of the radar scan strategy. There were very small differences between the CRR and OFRR algorithms. The CRR algorithm showed the best scores at the 2.5 km CAPPI level with a very close results between them at the 3.0 and 3.5 km CAPPI levels. Both the evaluation method and temporal resolution of 6 minutes can affect these results. The 6 minute temporal resolution may be short enough to not cause any significant differences between the two algorithms.

Alternatively, stratiform precipitation may have smoothed the effect of fast moving storms due to the use of seasonal periods and monthly time scales by the evaluation method. In either case, further evaluation will be needed to determine exactly how the temporal resolution affects the precipitation algorithm at a larger time scale.

The results showed that the lower the CAPPI level the better the precipitation estimates. However, the disadvantage of this is that the operating range of the radar at the 2.5 km level has a maximum range of 70 km. Using higher CAPPI levels the radar can potentially operate with satisfactory results with a range of up to 150 km. However, due to the radar beam increasing in height with range, 150 km is the outer limit at which a radar can successfully estimate precipitation at the ground. This observation was also confirmed when it was shown that CAPPI levels of 5.5 km and higher have no skill in estimating precipitation at the ground.

## 6.4 Summary

The following recommendations and future work can be concluded from the study. The evaluations detailed above have shown that the chosen classification scheme illustrates favourable results with a slight over-estimation in convective precipitation. This can be improved by additional filters, such as a bright-band filter or by using an alternative classification technique incorporating information from the Vertical Integrated Liquid (VIL) column such as was used in the classification technique of Zhang and Qi (2010).

The CRR and OFRR algorithms both showed an improvement over the TITAN algorithm. The CRR algorithm made a relatively small improvement when comparing the dual Z-R relationship against the simple Marshall-Palmer relation. The OFRR algorithm in some cases performed better than the CRR and in other cases not. Further evaluation is needed to determine the value of adding the technique.

The main result that comes out of this study is that the greatest improvement was from the use of CAPPI levels instead of a vertical column of reflectivity to estimate the rainfall. Thus, future work can possibly focus on the development of a “smart” CAPPI level that incorporates topography and sophisticated interpolation techniques that can skilfully extract the appropriate reflectivity for precipitation estimation. This might add greater value to the precipitation estimates than any other technique such as the dual Z-R relationship or optical flow technique for example.



## REFERENCES

- Andrieu H., Creutin J.D., 1995: Identification of vertical profiles of radar reflectivities for hydrological applications using an inverse method. Part I: Formulation. *J. Appl. Meteor.*, 34, 225-239.
- Atlas, D., Ulbrich, C.W., Mark Jr., F.D., Amitai, E., Williams, C.R., 1999. Systematic variation of drop size and radar-rainfall relation. *J. Geophys. Res.* 104, 155–169.
- Austin A., 1992: Radar in World War II: The South African contribution, *Eng. Sci. And Edu. J.*, Vol. 3, No. 3, p121-130
- Austin, P.M., Houze Jr., R.A., 1972. Analysis of the structure of precipitation patterns in New England. *J. Appl. Meteorol.* 11, 926–935.
- Bab-Hadiashar, A., and D. Suter, 1998: Robust optic flow computation. *International Journal of Computer Vision*, 29, 59–77.
- Battan, L. J., 1973: *Radar Observations of the Atmosphere*. University of Chicago Press., 324 pp.
- Bech J., Codina B., Lorente J., Bebbington D., 2002: The Sensitivity of Single Polarization Weather Radar Beam Blockage Correction to Variability in the Vertical Refractivity Gradient, *J. Atmos. And Oceanic Tech.*, 20, 845-855
- Bowler, N. E. H., C. E. Pierce, and A. Seed, 2004: Development of a precipitation nowcasting algorithm based upon optical flow techniques. *Journal of Hydrology*, 288, 74–91.
- Brandes, E.A., 1975: Optimizing rainfall estimates with the aid of radar. *J. Appl. Meteorol.*, 14, 1339-1345.
- Calheiros RV, Zawadzki I (1987) Reflectivity- Rain Rate Relationships for Radar Hydrology, in Brazil. *Journal of Climate and Applied Meteorology* 26, 118-132.
- Carte A.E. and Held G., 1978: Variability of hailstorms on the South African plateau. *J. Appl. Met.*, 17, 365-373
- Cheng M., Collier C.G., 1993: An objective method for recognizing and partially correcting bright band error in radar images. *J. Appl. Meteor.*, 32, 1142-1149
- Churchill, D.D., Houze Jr. R.A., 1984: Development and structure of winter monsoon cloud clusters on 10 December 1978. *J. Atmos. Sci.*, 41, 933-960.

## REFERENCES

- Chumchean, S., A. Seed, and A. Sharma, 2004: Application of Scaling in Radar Reflectivity for Correcting Range-Dependant Bias in Climatological Radar Rainfall Estimates, *J. Atmos. Oceanic Technol.*, 21, 1545-1556.
- Chumchean S., Sharma A., Seed A., 2006: An Integrated Approach to Error Correction for Real-Time Radar-Rainfall Estimation, *J. Atmos. And Oceanic Tech.*, 23, 67-79
- Chumchean, S., A. Seed, and A. Sharma, 2008: An operational approach for classifying storms in real-time radar rainfall estimation. *Journal of Hydrology*, 363, 1–17
- Collier, C.G., 1986a. Accuracy of rainfall estimates by radar. Part I. Calibration by telemetering raingauges. *J. Hydrol.* 83 (4), 207– 223.
- Collier, C.G., 1986b. Accuracy of rainfall estimates by radar. Part II. Comparison with raingauge network. *J. Hydrol.* 83 (4), 225–235.
- Collier, C.G., Knowles, J.M., 1986c. Accuracy of rainfall estimates by radar. Part III. Application for short-term flood forecasting. *J. Hydrol.* 83 (4), 237–249.
- Collier C.G., 1996: *Applications of Weather Radar Systems*, Wiley, 390pp.
- CSIR, 1948: Artificial stimulation of precipitation : interim progress report on experiments carried out by the C.S.I.R., the Division of Meteorology and the South African Air Force, December 1947 to April 1948.
- de Coning, E., Poolman, E., 2011: South African Weather Service operational Satellite based precipitation estimation technique: application and Improvements, *Hydrol. Earth Syst. Sci.*, 15, 1131–1145
- de Coning, E., Terblanche, D. E., and George, G.: Short range forecasting and nowcasting at the South African Weather Service using the newly acquired S-band radar systems, *Meteorological Technology, International*, UK, 120–123, 2010.
- De Waal K, Terblanche D, Dixon M., 2008: Irene radar and Radio LAN interference filtering. South African Weather Service, Pretoria (Unpublished Report).
- Deyzel I.T.H., Pegram G.G.S., Visser P.J.M, Dicks D., 2004: Spatial Interpolation and Mapping of Rainfall (SIMAR), Volume 2: Radar and Satellite Products. WRC Report No 1152/1/04, Pretoria.

## REFERENCES

- Dicks D., Hodson M.C., Held G., and Neishlos H., 1987: Initial result from the newly-developed CSIR Doppler pulse-pair processor. Abstract of the 4th Annual Conference of the South African Society for Atmospheric Sciences, Pretoria, 27.
- Dixon, M.J., 1977: Proposed Mathematical Model for the Estimation of the Areal Properties of High Intensity Short Duration Storms, MScEng thesis, University of Natal, Durban
- Doneaud, A.A., Ionescu-Niscov, S., Preignitz, D.L., Smith, P.L., 1984: The area-time integral as an indicator for convective rain volumes. *L. Climate Appl. Meteorol.* 23(4), 555-561.
- Doviak, R., and D. Zrnić, 1993: *Doppler Radar and Weather Observations*, Academic Press, 458 pp.
- Franco, M., R. Sánchez-Diezma, and D. Senpere-Torres, 2006: Correction of the error related to the vertical profile of reflectivity: previous partitioning of precipitation types. Fourth European Conference on Radar Meteorology and Hydrology, Barcelona, 125-128.
- Fletcher S.L.M., 1980: Radar observation in the BEMEX area. *BEWMEX Progress Report* 21, 47.
- Fulton, R., J. Breidenbach, D.-J. Seo, D. Miller, and T. O'Bannon, 1998: The WSR-88D rainfall algorithm. *Wea. Forecasting*, 13, 377-395
- Gagin A., Rosenfeld D. and Nozice H., 1986: Report on the analysis of convective rain cells, in the region of Bethlehem, R.S.A. as a basis for rainfall enhancement experiment. Report to the Water Research Commission, Pretoria, South Africa.
- Gourley J.J., Calvert C.M., 2003: Automated Detection of the Bright Band using WSR-88D Data, *Weather and Forecasting*, 18, 585-599.
- Gunn K.L.S., East T.W.R., 1954: The microwave properties of precipitation. *Quart. J. Roy. Meteor. Soc.*, 80, 522-545.
- Gupta, V. K., and E. C. Waymire, 1990: Multiscaling properties of spatial rainfall and river flow distribution. *J. Geophys. Res.*, 95, 1999–2009.
- Habib, E. and Krawjewski, W.F. (2002). Uncertainty Analysis of the TRMM Ground Validation Radar-Rainfall Products: Application to the TEFLUN-B Field Campaign. *Journal of Applied Meteorology*, 41,558-572.
- Hannesen, R. (2002). An enhanced surface rainfall algorithm for Radar Data. Technical Report Progress report for MUSIC, contract No. EVK1-CT-2000-00058, European Commission.

## REFERENCES

- Harold T., English E., Nicholass C., 1974: The accuracy of radar-derived rainfall measurements in hilly terrain. *Quart. J. Roy. Meteor. Soc.*, 100, 201-208.
- Harrison M.S.J., 1974: An Introduction to the Bethlehem Weather Modification Experiment. Part 1. Technical Paper No 1, Weather Bureau, Pretoria.
- Held G. and Gomes A.M., 1992: The first case study of a thunderstorm in South Africa based on dual-Doppler radar observations. *S. Afr. J. Sci.* 88, 516-524.
- Held G. and Carte A.E., 1973: Thunderstorms in 1971/72. CSIR Research Report 322, 1-77.
- Held G., 1978: The probability of hail in relation to radar echo heights on the South African Highveld. *J. Appl. Met.*, 17, 755-762.
- Held G., 1982: Comparison of radar observations of a devastating hailstorm and a cloud burst at Jan Smuts Airport. *Cloud Dynamics* eds. E.M. Agee and T. Asai, D Reidel Publ. Co., Dordrecht.
- Hewitt F.J., 1975: South Africa's role in the development and use of radar in World War II, *Military History Journal (South Africa)*.
- Hitschfeld W., Bordan J., 1954: Errors inherent in the radar measurement of rainfall at attenuating wavelengths. *J. Meteor.*, 11, 58-67.
- Hodson M.C., 1993: An Analysis of the meteorological and volume sampling effects on comparison of radar and raingauge measurement of rainfall. PhD thesis. University of Witwatersrand, Johannesburg.
- Horn, B.K.P., Schunck, B.G., 1981. Determining optical flow. *Artificial Intelligence* 17, 185–203.
- Houze Jr., R.A., 1973. A climatological study of vertical transports by cumulus-scale convection. *J. Atmos. Sci.* 30, 1112–1123.
- Houze Jr., R.A., 1993. *Cloud Dynamics*. Academic Press, 573pp.
- Houze Jr., R.A., 1997. Stratiform precipitation in regions of convection: a meteorology paradox? *Bull. Am. Meteorol. Soc.* 78, 2179–2195.
- IPCC: Report on global warming – Localizing a global story, <http://www.ipccinfo.com/extreme.php> April6, 2007.

## REFERENCES

- Joe P., May, P.T., 2003: Correction of Dual PRF Velocity Errors for Operational Doppler Weather Radars. *J. Atmos. Oceanic Technol.*, 20, 429–442.
- Joss J., Lee R., 1995: The application of radar-gauge comparisons to operational precipitation profile corrections. *J. Appl. Meteor.*, 34, 3612-2630
- Kitchen M., Brown R., Davies A.G., 1994: Real-Time correction of weather radar data for effects of bright band, range and orographic growth in widespread precipitation. *Quart. J. Roy. Meteor. Soc.*, 120, 1231-1254.
- Krauss T.W., Bruintjies R.T. and Verlinde J., 1987: Microphysical and radar observations of seeded and non-seeded continental cumulus clouds. *J. Climate Appl. Meteor.*, 26, 585-606
- Kroese N.J., 2004: Spatial Interpolation and Mapping of Rainfall (SIMAR), Volume 1: Maintenance and Upgrading of Radar Rain Gauge Infrastructure. WRC Report No 1151/1/04, Pretoria.
- Kroese N.J., 2006: Daily Rainfall mapping Over South Africa (DARAM): Infrastructure and Capacity Building. WRC Report No 1426/1/06, Pretoria.
- Kruger, A. C., 2007: Climate of South Africa, Precipitation, Report No. WS47, South African Weather Service, Pretoria, South Africa, 41 pp.
- Kuligowski R.J., Scofield R.A., 2003: Status and Outlook of Operational Satellite Precipitation Algorithms for Extreme-precipitation Events. *Weather and Forecasting*.18, 1037-1051
- Landman, S., Engelbrecht, F.E., Dyson, L.L., Engelbrecht, C.J., Landman, W.A., 2012: A multi-model ensemble system for short-range weather prediction in South Africa, *WaterSA*, 38, 5, 765-774
- Lee G, Zawadzki I (2005) Variability of drop size distributions: Time-scale dependence of the variability and its effects on rain estimation. *Journal of Applied Meteorology*, 44, 241-255.
- Li, L., Schmid, W., Joss, J., 1995. Nowcasting of motion and growth of precipitation with radar over a complex orography. *Journal of Applied Meteorology* 34, 1286–1300.
- Marshall, J.S., and W.M.K. Palmer, 1948: Distribution of Raindrops with Size, *J. Meteorology*, 5,165-166

## REFERENCES

- Mather G.K. and Terblanche D.E., 1993: The National Precipitation Research Programme: Final Report 1990-1992. WRC Report, Pretoria.
- Mather G.K., Dixon M. And de Jager J.M., 1996: Assessing the potential for rain augmentation – The Nelspruit randomized convective cloud seeding experiment. *J. Appl. Meteor.*
- Mather G.K. and Terblanche D.E., 1996: The National Precipitation Research Programme: Final Report 1993-1996. WRC Report, Pretoria.
- Mittermaier M.P., 1999: Characteristics of the radar vertical reflectivity profile. MSc dissertation. University of Natal, Durban.
- Mittermaier M.P., Terblanche D.E., 1997: Converting weather radar data to Cartesian space: A new approach using DISPLACE averaging. *Water SA*, 23(1), 45-50.
- Mandelbrot, B. B., 1982: *The Fractal Geometry of Nature*. W. H. Freeman, 460 pp.
- Mueller E.A., Jones D.M.A., 1960: Drop size distributions in Florida. *Proc. Eighth Wea. Radar Conf.*, pp. 299-305
- Mylne, M.F., Hems B.D., 1991: Examination of the impact of range on the quality of daily catchment rainfall totals derived from the Ingham radar. In: Cluckie I.D., Collier C.D. (Eds.) *Hydrological Application of Weather Radar*, pp 258-266.
- Pegram G.G.S., 2004: *Spatial Interpolation and Mapping of Rainfall (SIMAR), Volume 3: Data Merging for Rainfall Map Production*. WRC Report No 1153/1/04, Pretoria.
- Pegram G.G.S, Sinclair S., Wesson S., 2006: *Daily Rainfall mapping Over South Africa: Modelling*, WRC Report No. 1425/1/06
- Poolman, E, 2009: *Developments in Flash Flood Forecasting: The SAFFG system*, Internal Presentation, available at South African Weather Service, Pretoria, South Africa, 2009.
- Poolman, E., de Coning, E., Becker, E., Pegram, G., Sinclair, S., Kroese N., 2014: *Improvement of Early Preparedness and Early Warning Systems for Extreme Climatic Events – Flood Warnings*, WRC Report No K5/2068/1 (Final Draft), Pretoria.
- Press W.H., S.A. Teukolsky, W.T. Vetterling, and B.P. Flannery. 1992. *Numerical Recipes in FORTRAN*. 2nd ed. Cambridge: University Press.
- Reyniers M., 2008: *Quantitative Precipitation Forecasting based on radar observations: principles, algorithms and operational systems*, Royal Meteorological Institute of Belgium.

## REFERENCES

- Rinehart R.E., 2004: Radar for meteorologists, Rinehart Publications, Missouri.
- Rinehart R.E., Garvey E.T., 1978: Three-dimensional storm motion detection by conventional weather radar. *Nature*, 273, 287-289.
- Rosenfeld D., Mintz Y., 1988: Evaporation of rain falling from convective clouds as derived from radar measurements. *J. Applied Meteor.*, 27, 209-215.
- Rosenfeld D. and Gagin A., 1989: Factors governing the total rainfall yield from continental convective clouds. *J. Appl. Meteor.*, 28, 1015-1030.
- Rosenfeld D., Wolff D.B., Atlas D., 1993: General probability-matched relations between radar reflectivity and rain rate. *J. Appl. Meteorol.*, 32, 50-72
- Rosenfeld D., Wolff D.B., Amitai E., 1994: The window probability matching method for rainfall measurements with radar. *J. Appl. Meteorol.*, 33, 683-693
- Sanchez-Diezma R., Zawadzki I., Sempere-Torres D., 2000: Identification of the bright band through the analysis of volumetric radar data. *J. Geophys. Res.*, 105, 2225-2236.
- Sempere Torres, D., Sanchez-Diezma, R., Zawadzki, I., Creutin, J.D., 2000. Identification of stratiform and convective areas using radar data with application to the improvement of DSD analysis and Z-R relations. *J. Phys. Chem. Earth (B)* 25, 985– 990
- Sinclair, S. and Pegram, G., 2005: Combining radar and rain gauge estimates using conditional merging. *Atmospheric Science Letters*, 6:19–22.
- Sinclair, S., 2007: Spatio-temporal Rainfall Estimation and Nowcasting for Flash Flood Forecasting, Phd Thesis, School of Civil Engineering, Surveying and Construction Management, University of KwaZulu-Natal
- Smith C.J., 1986: The reduction of errors caused by bright bands in quantitative rainfall measurements made by radar. *J. Atmos. Oceanic Technol.*, 3, 129-141.
- Stanski, H.R., L.J. Wilson, and W.R. Burrows, 1989: Survey of common verification methods in meteorology. World Weather Watch Tech. Rept. No.8, WMO/TD No.358, WMO, Geneva, 114 pp.
- Steiner, M., R. A. Houze Jr, and S. E. Yuter, 1995: Climatological characterization of three-dimensional storm structure from operational radar and rain gauge data. *Journal of Applied Meteorology*, 34, 1978–2007

## REFERENCES

- Steyn P.C.L. and Bruintjies R.T., 1990: Convective cloud characteristics for the Bethlehem area. *Water SA*, 16-2, 115-118.
- Tao, W.-K., Simpson, J., Sui, C.-H., Ferrier, B., Lang, S., Scala, J., Chou, M.-D., Pickering, K., 1993. Heating, moisture, and water budgets of tropical and mid latitude squall lines: comparisons and sensitivity to long wave radiation. *J. Atmos. Sci.* 50, 673– 690.
- Terblanche D.E., 1996: Digital Signal Processing of Data from Conventional Weather Radar: The DISPLACE method. PhD thesis. University of Pretoria, Pretoria.
- Terblanche D.E., Visser P.J.M., Mittermaier M.P., Kroese N.J., 2001: VIPOS: Vaal Dam Catchment integrated Precipitation Observation System WRC Report No 954/1/01, Pretoria.
- Terblanche D.E., Pegram G.G.S., Mittermaier M.P., 2001: The development of weather radar as a research and operational tool for hydrology in South Africa, *Journal of Hydrology*, 241, 3-25.
- Tokay, A., Short, D.A., 1996. Evidence from tropical raindrop spectra of the origin of rain from stratiform versus convective clouds. *J. Appl. Meteorol.* 35, 355–371.
- Van Heerden J. and Steyn P.C.L., 1999: Weather Radar Measurement of Rainfall for Hydrological and other Purposes, WRC Report No 693/1/99, Pretoria.
- Visser P.M.J. 1999: The use of Volumetric Scanned Weather Radar Reflectivities for the identification of Convective Storm Characteristics. MSc dissertation.
- Wexler R., Atlas D. 1963: Radar reflectivity and attenuation of rain. *J. Appl. Meteor.*, 2, 276-280.
- Wiener G., Dixon M., 1993: TITAN Thunderstorm Identification, Tracking, Analysis, and Nowcasting - A Radar-based Methodology, *J. Atmos. Oceanic Technol.*, 10, 785–797.
- Wilks, D.S., 2005: *Statistical Methods in the Atmospheric Sciences*. 2nd Edition. Elsevier, 627 pp.
- Wilson J.W., 1966: Storm-to-storm variability in the radar reflectivity rainfall rate relationship. *Proc. Twelfth Conf. Radar Meteor.*, pp. 229-233.
- Wilson J.W., 1975: Radar-gage precipitation measurements during IFYGL. CEM Rept. 4177-4546, The Center for the Environment and Man, Hartford, Conn., 121 pp.



## REFERENCES

- Wilson J.W., Brandes E.A., 1979: Radar measurement of rainfall – a summary. *Bull. Amer. Meteor. Soc.*, 60, 1048-1058.
- Yuter, S.E., Houze Jr., R.A., 1997. Measurements of raindrop size distributions over the pacific warm pool and implications for Z– R relations. *J. Appl. Meteorol.* 36, 847–867.
- Zawadzki, I., 2006. Sense and Nonsense in radar QPE. In: *Proceedings of 4th European Conference on Radar in Meteorology and Hydrology, Barcelona, Spain*, pp. 126–129.
- Zhang, J., Howard, K., Langston, C., Vasiloff, S., Kaney, B., Arthur, A., van Cooten, S., Kelleher, K., Kitzmiller, D., Ding, F., Seo, D.J., Wells, E., Dempsey, C., 2011: National Mosaic and Multi-Sensor QPE (NMQ) Systems: Description, Results, and Future Plans, *Bull. Amer. Meteor. Soc.*, 92 (10), 1321-1338
- Zhang J., Qi Y., 2010: A Real-Time Algorithm for the Correction of Brightband Effects in Radar-Derived QPE, *J. Hyd. Meteor.*, 11, 1157-1171.
- Zrnica, D., and A. Ryhkov, 1996: Advantages of rain measurements using specific differential phase. *J. Atmos. Oceanic Technol.*, 13, 454–464.